Linear and Non-linear Interactions in a Rough-Wall Turbulent Boundary Layer

Thesis by

Jonathan P. Morgan

In Partial Fulfillment of the Requirements for the
Degree of
Doctorate Of Philosophy in Aeronautics

CALIFORNIA INSTITUTE OF TECHNOLOGY
Pasadena, California

2019
Defended February 21, 2019

Jonathan P. Morgan
ORCID: 0000-0003-2898-4868

ACKNOWLEDGEMENTS

Many, many people have helped and encouraged me on this very long journey towards completing my PhD, none more so than my advisor, Beverley McKeon. She has my eternal gratitude for the guidance and support she provided me through the years, which have been invaluable to my development as a researcher. I would also like to thank Dale Pullin, Tim Colonius, and Dan Meiron for agreeing to serve on my committee.

My research group at Caltech has been the best working environment of my life, thanks to the many wonderful people who have shared it with me. Reeve Dunne, Subrahmanyam Duvvuri, Esteban Hufstedler, Kevin Rosenberg, Tess Saxton-Fox, David Huynh, Sean Symon, Simon Toedtli, Ryan McMullen, Maysam Shamai, Morgan Hooper, Ben Barthel, Mitul Luhar, Rashad Moarref, Scott Dawson, Angeliki Laskari, Arslan Ahmed, and Jane Bae have all helped me with research, helped me laugh, and helped me stay sane, and I am so thankful to each of them. The group's administrative assistants, Jamie Meighen-Sei and Denise Ruiz, have also been a tremendous resource in supporting both my research and good spirits. I could not have completed this thesis without all of these group members.

I would also like to thank Petros Arakelian, who performed the 3D printing of the roughness surfaces shown in this thesis. His advice and support was essential for designing my experiments.

My first year at Caltech was supported by the Ikawa Fellowship in Aeronautics, generously funded by GALCIT alumnus Hideo Ikawa, to whom I am eternally grateful.

Lastly, I would like to thank my family: my father Chip, my mother Marge, and my sister Heather. They have encouraged my academic pursuits at every turn, even when it has meant living 3000 miles away. Without their love and support, I could not have done any of this.

ABSTRACT

This thesis explores the linear and non-linear interactions which take place in a rough-wall turbulent boundary through experiments and modeling. In order to derive physics-based models for the relation between roughness geometry and flow physics, two very simple periodic roughnesses were 3D printed and placed in a boundary layer wind tunnel for separate experiments. Hot-wire measurements were taken at a grid of points within a single period of the roughness in order to map the spatial variation of important flow statistics in way that allows correlation back to the roughness geometry. Time averaged streamwise velocity and the power spectrum of instantaneous streamwise velocity were both found to vary coherently with the roughness. The spatial variation of the time averaged velocity was identified as the linear result of the roughness, as it has identical wavenumber and frequency to the static roughness geometry. Modeling the time-averaged velocity field as a response mode of the linear resolvent operator was found to be reasonable for certain wavenumbers. The spatial distribution of the power spectrum was shown to be a non-linear effect of the roughness; the power spectrum only measures the energy of convecting modes, which necessarily have non-zero frequency and cannot correlate linearly to the static roughness. The spatial modulation of the power spectrum was found to be indicative of non-linear triadic interactions between the static velocity Fourier modes and pairs of convecting modes, as allowed by the Navier-Stokes equations. A low-order model for these interactions, and their effect on the power spectrum, was constructed using resolvent response modes to represent all velocity Fourier modes. The model was found to qualitatively predict the modulation of the power spectrum for several sets of wavenumbers. The success of such a simple model suggests that it presents a useful low-order understanding of non-linear forcing between scales in rough-wall boundary layers.

PUBLISHED CONTENT AND CONTRIBUTIONS

J Morgan and B McKeon. Relation between a singly-periodic roughness geometry and spatio-temporal turbulence characteristics. *Int. J. of Heat and Fluid Flow*, 71:322-333, 2018. DOI: 10.1016/j.ijheatfluidflow.2018.04.005.

Jonathan Morgan designed and performed the experiment, analyzed the data, created the figures, and was the primary author.

TABLE OF CONTENTS

LIST OF ILLUSTRATIONS

LIST OF TABLES

Chapter 1

INTRODUCTION

Turbulent boundary layers are a pervasive phenomenon in the fields of climate, industry, and aviation. In many cases of practical interest, the surfaces over which the boundary layers develop are not smooth, and this roughness can alter the important characteristics of the boundary layer, including drag. The study of rough-wall-bounded turbulence must encompass not only the enormous phase space brought on by the expanse of scales in turbulence, but also an incredibly broad parameter space, which includes any surface formed by nature or devised by the human brain. Due to the infinite possible geometric variety of rough surfaces, it is impossible for simulations and experiments to fully explore and document the entire phase space of roughness. This poses a problem for design engineers and analysts who would like to know the effects of a particular arbitrary roughness without performing a potentially costly experiment or simulation, but it also presents an opportunity for scientists. A rough wall can be a slight perturbation to an otherwise-canonical flow. Subjecting the "black box" of canonical wall-bounded turbulence to a slight change and observing the outcome can help expose its inner workings. As outlined in the final section of this chapter, this thesis will connect the study of rough- and smooth-wall flows by creating a simple roughness, documenting its direct linear and indirect non-linear effects on a boundary layer, and creating a simple, cheap, low-order model to explain the observed results.

1.1 The Turbulent Boundary Layer

The Navier-Stokes equations which govern the motion of incompressible viscous fluids were first derived by Navier [50], and are reproduced in Equations 1.1 and 1.2. Vector velocity $\boldsymbol{u}$ and thermodynamic pressure p are the fields which vary in space (vector coordinate $\boldsymbol{x} = (x, y, z)$) and evolve in time t. Density ρ and kinematic viscosity ν may in general vary, but are considered in this thesis to be constant and homogeneous. These equations apply the second law of motion and the linear relationship between stress and strain in a fluid, first noted by Newton [51], to the case of a general three-dimensional flow.

$$\frac{\partial \boldsymbol{u}}{\partial t} + \boldsymbol{u} \cdot \nabla \boldsymbol{u} = -\frac{1}{\rho}\nabla p + \nu \nabla^2 \boldsymbol{u}, \tag{1.1}$$

$$\nabla \cdot \boldsymbol{u} = 0. \tag{1.2}$$

The number of free parameters in Equation 1.1 may be reduced by non-dimensionalizing the terms using characteristic scales in length (L), velocity (W), and pressure (Q), and time may be non-dimensionalized by a composite time scale L/W to yield Equations 1.3 and 1.4. For conciseness, we also introduce the Reynolds number $Re = \frac{WL}{\nu}$ as a non-dimensional parameter.

$$\frac{\partial \grave{\boldsymbol{u}}}{\partial \grave{t}} + \grave{\boldsymbol{u}} \cdot \nabla \grave{\boldsymbol{u}} = -\frac{P}{\rho W^2}\nabla \grave{p} + \frac{1}{Re}\nabla^2 \grave{\boldsymbol{u}}, \tag{1.3}$$

$$\nabla \cdot \grave{\boldsymbol{u}} = 0. \tag{1.4}$$

The formulation of the Navier-Stokes equations in Equations 1.3 and 1.4 describes the evolution of the non-dimensional velocity ($\grave{\boldsymbol{u}} = \boldsymbol{u}/W$) and pressure ($\grave{p} = p/P$) fields in non-dimensional space ($\grave{x} = x/L$) and time ($\grave{t} = TW/L$). The coefficient $\frac{P}{\rho W^2}$ is of no dynamical significance, as the absolute level of pressure in an incompressible flow does not enter into the equations of motion. This leaves only the Reynolds number Re, representing a ratio of inertial to viscous forces, as a free parameter in the equations of motion. Boundary conditions are typically taken to be identically zero relative velocity at solid surfaces and arbitrary prescribed velocities at other boundaries. Two flows with initial and boundary conditions which are identical under non-dimensionalization will evolve identically if they have the same Reynolds number.

One such flow is the canonical zero-pressure-gradient smooth-wall boundary layer (ZPGBL): velocity is identically zero along a half-plane surface at $Y = 0, X > 0$, and tends to a single freestream velocity U_∞ infinitely far from the surface. The time-averaged pressure field is homogeneous. The length scale L can be taken to be the distance X along the plate, while U_∞ is the velocity scale. When the Reynolds number is large, the last term in Equation 1.3 would seem to vanish as its coefficient tends to zero. This presents the mathematical problem of reducing the order of the equation, preventing the solution from satisfying all boundary conditions. Prandtl [58] was the first to reconcile this apparent paradox, noting that, in a thin layer adjacent to the surface, strong gradients in velocity maintain the viscous term as a

part of the dominant balance in the equation. Prandtl's theory divides the flow into two regions: a freestream away from the wall without significant viscous stresses, and a "boundary layer" just above the wall, where viscosity cannot be ignored.

For sufficiently low Reynolds number, a canonical ZPGBL will be steady and laminar [9]. For this case, Blasius [8] found a self-similar solution of the Navier-Stokes equations, in which the velocity field is a function only of the freestream velocity and the similarity coordinate $\chi = y\sqrt{U_\infty/\nu x}$. A laminar ZPGBL which is impulsively perturbed will eventually return to a Blasius profile, with a spatial evolution that has been shifted in x. For this reason, from here, we will take the length scale of a boundary layer to be the 99% boundary layer thickness δ, the distance from the wall at which the mean velocity recovers to 99% of its freestream value. We will also use a different velocity scale in the friction velocity $u_\tau = \sqrt{\tau_w/\rho}$, derived from the shear stress at the wall τ_w, for ease of comparison to rough wall flows. The resulting Reynolds number $Re_\tau = u_\tau\delta/\nu$ is called the Karman number or friction Reynolds number. For the ZPGBL, it is bijective and monotonic with other definitions of the Reynolds number, uniquely identifying a flow condition. Quantities normalized by u_τ are denoted with a superscript plus.

1.2 Similarity and Modeling of Rough-Wall Turbulent Boundary Layers

In addition to the Reynolds number, the characteristics of a rough-wall boundary layer depend on the infinite number of geometrical parameters which describe the surface roughness. Although each individual pattern of roughness presents a unique physical and mathematical case, some patterns emerge across a wide variety of geometries. As in the smooth-wall case, many rough-wall flow quantities scale with the friction velocity u_τ and kinematic viscosity ν, and quantities which are non-dimensionalized by these inner variables are denoted with a superscript plus. Flows without sufficient scale separation between the roughness height k and the boundary layer thickness δ are characterized as "obstacle flows" and have significant qualitative differences in measured flow quantities throughout the boundary layer when compared to smooth wall flows, including the elimination of the logarithmic layer [32]. Jimenez gives a criterion of δ/k <40 to separate obstacle flows from rough-wall flows, which do exhibit some similarity to canonical smooth-wall flows.

Nikuradse [52] performed the first systematic study of rough wall flows, using sifted sand and lacquer to create geometrically similar roughnesses of varying height. He found that, as in the smooth case, there exists a region of the flow in which the

inner-normalized streamwise mean velocity $\overline{u}^+$ scales logarithmically with wall-normal distance y^+. Compared to smooth walls, however, the virtual origin of the velocity profile is displaced from the wall and the velocity profile in the logarithmic region is shifted toward slower velocities. The magnitude of this shift is named the "Hama roughness function" and is labeled ΔU^+. Subsequent research [48], including by Colebrook [14] with industrial roughness, found that the mean profile of a wide variety of roughnesses can be parameterized in the "fully rough" regime ($k^+ \to \infty$) with an "equivalent sand roughness" $k_{s\infty}$. The equivalent sand roughness of a rough wall is the magnitude of the roughness in Nikuradse's experiments which would match the ΔU^+ of that rough wall at high k^+. Therefore, the behavior of a rough wall in the fully rough regime is described by a single parameter, though at present no work has provided a general relation between an arbitrary roughness geometry and its equivalent sand roughness [32]. Outside the fully rough regime, with intermediate $k^+_{s\infty}$, both $k_{s\infty}$ and the roughness geometry figure into the observed variables, even at very high Reynolds numbers [1]. Between the surface and the logarithmic layer is a roughness sublayer which is believed to extend to several times the sand grain roughness [60].

Wall flows with three-dimensional roughness and sufficient scale separation δ/k exhibit similarity with smooth-wall flows beyond just the logarithmic mean profile. Townsend's hypothesis [69] posits that the boundary layer physics outside of the roughness sublayer are affected by the roughness only through the length and velocity boundary conditions which the sublayer imposes on the rest of the flow. In this description, the roughness elements serve only to perturb the turbulent cascade in the roughness sublayer, altering the velocity profile near the wall and therefore the wall shear stress. The resulting values of u_τ and δ then provide the scales for the flow statistics in the outer layer, so that rough-wall quantities of the form $Q^+(y/\delta)$ are identical to smooth-wall quantities at the same Reynolds number. Schultz and Flack [65] find such a similarity for the velocity defect $U^+_\infty - U^+$ and for single-point velocity correlations up to third order. Flores et al. [21] provides evidence for this view, observing roughness-like similarity in simulated flows with prescribed velocities and Reynolds stresses at the wall.

In contrast, a parametric study of of herringbone-pattern riblet roughness by Nugroho et al. [53] found that for such a periodic roughness, large spatial variations in mean flow quantities can persist throughout the boundary layer, with boundary layer thickness varying by a factor of two within a single spanwise period of rough-

ness. Using experimental data up to high Reynolds number ($Re_\tau \approx 2800 - 17400$), Morrill-Winter et al., [49] find a dependence of normalized wall-normal velocity variance on roughness conditions in the wake region of a sandpaper-roughness boundary layer, well outside the roughness layer. Mejia-Alvarez and Christensen [45] discovered large, δ-scale variations in ensemble-averaged flow velocity within the roughness sublayer even in a disordered, real world roughness derived from a damaged turbine blade. Further studies by Barros and Christensen [6] and Anderson et al. [3] correlated areas of recessed roughness to low-momentum pathways (LMP) and elevated roughness to high-momentum pathways (HMP). They further found associated secondary flows which persisted well into the outer layer of the boundary layer. Similar to Hinze's [25] work on flows in the corners of rectangular ducts, these flows were found to be Prandtl's secondary flow of the second kind, generated by spanwise gradients in Reynolds stress. Studies of streamwise-aligned heterogeneous roughness by Vanderwel and Ganapathisubramani [71] and Willingham et al. [74] found that these secondary flows can extend through the boundary layer with a scale on the order of δ when the spanwise spacing is appropriately large. Spanwise-aligned roughnesses, including both two-dimensional bars and staggered cubes, were found by Volino et al. [72] to effect the flow well into the outer region via blockage effects. As Pedras et al. note, any spatial variation in mean velocity creates a dispersive stress which appears in the equation for the spatio-temporally averaged velocity [55]. These studies on heterogeneous roughness indicate a number of circumstances under which a roughness will not obey Townsend's hypothesis, particularly when the roughness is coherent in the streamwise and spanwise directions with large length scales.

Flows with small amounts of transpiration have also been shown to obey Townsend's hypothesis, similarly to low-amplitude roughness. Gomez et al. [24] used a time- and azimuthal-averaged streamwise momentum equation to isolate the effect of periodic transpiration on the mean profile of pipe flow. At large amplitudes, such transpiration is capable of increasing or decreasing flow rates, depending on the transpiration wavenumber. The change in mean flow due to transpiration can be broken down into three component mechanisms: a change in the Reynolds stress throughout the pipe radius, an interaction between the transpiration and the downstream flow, and a component associated with streamwise inhomogeneity. All three terms are significant to the observed change in mean velocity profile.

Despite qualitative support for the importance of the near-wall activity to rough-

wall-bounded flow physics, there is a relative paucity of quantitative predictive spectral models. Chakraborty and Gioia [23] provide a quantitative description of the mechanism by which roughness elements affect u_τ by taking the elements to physically limit the size of a quasi-streamwise vortex of the near-wall cycle, truncating the cascade at roughness scales. Their model accurately reproduces the qualitative behavior of the skin friction coefficient with varying Reynolds number, but falls short of quantitatively predicting skin friction for arbitrary roughnesses.

1.3 Measurement Challenges in Rough-Wall Flows

Ideally, efforts to connect roughness geometry to flow physics would start with full-field measurements of rough-wall flows. Unfortunately, several features of experimental rough-wall turbulence make measurements difficult. While the boundedness of channel and pipe flows allow simple measurement of wall shear stress from pressure drop, rough-wall boundary layers have no such relation. Wall drag force on the flow includes both viscous stress and form drag from local acceleration of the flow, and separation may occur over individual roughness elements. Skin friction and a virtual origin for rough-wall boundary layers is therefore usually estimated from the logarithmic region of the mean velocity profile, using a modified Clauser fit [56] [37]. An uneven wall can also block optical access and prevent the close approach of physical probes of finite size. Optical access through a rough wall requires refractive index-matching, as in Hong et al. [26], who used PIV to measure fields of velocity and Reynolds stress in the roughness sublayer and between close-packed pyramidal roughness elements. The present work circumvents some of these issues with a long-wavelength roughness that creates a disturbance throughout the boundary-layer, even away from the wall.

1.4 Experiments and Simulations on Idealized Roughnesses

Recently, there has been intense study to determine the relation between a roughness geometry and its effect on the boundary layer. MacDonald et al. [41] have demonstrated an efficient method of simulating mean quantities of interest such as ΔU^+ for sine-wave roughness by performing direct numerical simulation in a rough channel with very limited spanwise domain of a few roughness wavelengths. Although these simulations do not by themselves accurately predict the flow within the entire channel, using these simulations to provide a boundary condition to full-domain, lower resolution DNS accurately reproduces the exact flow. This indicates that the eddies which provide the physical link between roughness geometry and

the physics of the roughness sublayer have a size on the order of the roughness wavelength. Flack and Schultz [20] have found correlations between the roughness function and the statistical moments of the roughness topology. Jelly and Busse found that a roughness with only pits resulted in a much weaker roughness function than one with only peaks. They attribute this to a dependence of the relative behavior of Reynolds and dispersive stress on the skewness of the surface [31]. Mejia-Alvarez and Christensen [44] explored the effects of individual roughness scales by using proper orthogonal decomposition to extract a low-order representation of a real-world roughness. A 3D-printed low-order roughness constructed from the fifteen most amplified proper orthogonal decomposition (POD) modes was found to accurately reproduce the drag characteristics of the full roughness in channel flow, indicating that a key subset of geometric scales are responsible for the flow physics of real-world rough-wall flows. The present work proceeds in the opposite direction, by creating a simple, singly-periodic roughness to observe the effect on the flow of a single large roughness scale.

1.5 Spatio-Temporal Representation of Turbulence

Heuristic understanding and simplified modeling of the dynamics of a turbulent boundary layer requires a low-order representation of the velocity phase space, for example by projecting onto a low-dimensional subspace. Unfortunately, the multi-scale and apparently chaotic nature of wall turbulence leaves its phase space without a natural basis. In addition to the representation of turbulence with primitive variables, many different transformations and projections have been used to guide intuition or to formulate models. The streamwise, spanwise, and time homogeneity of canonical shear flow statistics suggest a Fourier basis in these dimensions. When a periodic roughness is introduced in Chapter 2, statistics will be assumed to be periodic with equal wavenumber to the roughness. A spatial Fourier basis for those statistics will consist of wavenumbers which are integer multiples of the roughness wavenumber. Wavelet transforms [19] for turbulence capture the effect of position and scale of turbulent features in a sparse manner by using basis functions with local support. Data-driven approaches like proper orthogonal decomposition (POD) [7] and dynamic mode decomposition [62] both create a basis for the flow using full field time-series data from experiments or simulations to identify dynamically important modes. Spectral POD (SPOD) is the application of POD to time-Fourier-transformed stationary flow fields to create a basis which is coherent in both space and in time. Towne et al. [68] showed that under certain circumstances, SPOD

produces modes which are identical to DMD modes or resolvent modes.

Resolvent analysis [43], in contrast to data-driven approaches, requires only a Reynolds number and a mean velocity field as input. For the one-dimensional resolvent used in this thesis, only a one-dimensional mean velocity profile in the wall-normal direction is needed. The Fourier-transformed Navier-Stokes equations for a boundary layer are recast such that a Fourier mode of velocity and pressure in the flow is the result of a linear operator (the resolvent) acting on a forcing mode (the Fourier-transformed non-linear term). By retaining the non-linearity explicitly, resolvent analysis gives an exact representation of the Navier-Stokes equations that is self-consistent. For a given flow, the resolvent operator is a function of wavenumber and frequency. Performing a singular value decomposition on a resolvent operator gives orthonormal bases in the wall-normal direction for both the velocity modes and the forcing modes, ranked by the degree of amplification (or singular value) caused by the operation of the resolvent. In general, full representation of a velocity field would require the full set of velocity basis vectors for each wavenumber-frequency combination. However, when the highest singular value is much larger than the other singular values, one may expect the output of the operator (the velocity Fourier modes) to be dominated by the most amplified basis vector. This suggests that this basis vector may be an optimal representation of a velocity Fourier mode for modeling purposes. Resolvent analysis has been used to successfully model numerous aspects of turbulence including streamwise energy-density scaling [46], opposition control [39], and as a basis for assimilating experimental data in 2D flows [66].

The resolvent method for shear flows has been extended to non-spatially uniform boundary conditions, including roughness, in a number of ways. Luhar et al. [40] use asymptotic expansions similar to Gaster et al. [22] to construct a resolvent boundary condition for a compliant surface. Chavarin and Luhar [12] use a volume-penalization method similar to immersed boundary methods in CFD to impose a zero velocity field within streamwise-constant roughness. Gomez et al. [24] calculate a resolvent operator that is not Fourier-transformed in the streamwise direction in order to accommodate spatially-dependent transpiration at the wall.

1.6 Coherent Structures in Turbulent Flows

The turbulent, unsteady motions that define and sustain a wall-bounded turbulent flow are not simply stochastic noise, but are instead organized into structures that

are coherent in space and time [10]. These coherent structures may be identified in a statistical sense, from local extrema in two-point correlations or power spectra, or directly from observed velocity fields, using instantaneous snapshots, flow visualization, or conditional averaging. These methods reveal patterns in the velocity field which preferentially recur and persist in time as they convect through the flow. Two classes of coherent structures will be discussed here: the near-wall cycle and superstructures.

The near-wall cycle was first observed by Kline et al. [36] as a series of streamwise-aligned regions of alternating high and low velocity ("streaks"), with a spanwise wavelength of roughly $100\nu/u_\tau$. These streaks were observed to slowly move away from the wall before becoming unstable and breaking up. Work by Jimenez and Pinelli [33] and Schoppa and Hussain [64] explained the cycle as the result of linear amplification of the streaks and interaction with quasi-streamwise vortices. Hutchins and Marusic [28] associate the near-wall cycle with a local maximum of the premultiplied power spectrum of the streamwise velocity. This local maximum was found at a height of $15\nu/u_\tau$ and a streamwise wavelength of $1000\nu/u_\tau$ for values of Re_τ from 1010 to 7300.

Superstructures were first observed by Hutchins and Marusic [28] using both spectral data and instantaneous velocity fields. They are long, meandering regions of high or low velocity in the log region of boundary layers. Superstructures scale in outer units, with a local maximum in the premultiplied power spectrum occurring at a wall-normal height of 0.06δ and a streamwise wavelength of 6δ for turbulent boundary layers, but instantaneous velocity fields show that the structures extend down to the wall. Monty et al. [47] found that superstructures are qualitatively similar but distinct from the very large scale motions (VLSM) first observed in channel and pipe flows by Kim and Adrian [35].

1.7 Amplitude Modulation of Small-Scale Turbulence by Large-Scale Structures

Large scale velocity disturbances are known to influence small-scale flow physics in canonical smooth-wall flows. A deterministic coupling between between large- and small-scale structures in shear flows was first observed by Rao et al. [59] and Bandyopadhyay et al. [5]. Hutchins and Marusic [29] connected the large-scale and small-scale structures to superstructures and the near-wall cycle, respectively. Mathis et al.[42] went on to quantify the correlation with the amplitude modulation

correlation coefficient R. Under this approach, the large scale velocity fluctuations u_L and small scale fluctuations u_S are separated from the full velocity time series by a filter and considered as independent signals. The envelope of the small scale fluctuations E is calculated as a function of time using the Hilbert transform. The envelope is then filtered to isolate large-scale modulation of the envelope, resulting in the time series E_L. This quantity is compared to the large scale fluctuations using the temporal correlation coefficient to yield the amplitude-modulation correlation coefficient, R in Equation 1.5, with an bar indicating a time average.

$$R = \overline{u_L E_L} / \left(\sqrt{\overline{u_L^2}} \sqrt{\overline{E_L^2}} \right). \tag{1.5}$$

In smooth-wall flows, R attains a maximum in the viscous region, approaches and then passes through zero in the log region, and attains a minimum in the wake region before increasing in the intermittent turbulent/non-turbulent region at the edge of the boundary layer.

Jacobi and McKeon [30] demonstrated that R is dominated by the signature of one scale, associated with the very large-scale motions in the flow. For periodic signals, such a correlation coefficient can be cleanly interpreted as the relative phase between signals via the dot product [13]. Duvvuri and McKeon [18] showed R to be a measure of average phase for pairs of turbulent scales which are triadically consistent with the large scales. As an example, a singly-periodic large scale signal u_L,

$$u_L = a_L \cos(k_L x - \omega_L t + \theta_L), \tag{1.6}$$

with amplitude a_L, wavenumber k_L, frequency ω_L, and phase θ_L, combined with a small scale signal u_S,

$$u_S = a_S \cos(k_p x - \omega_p t + \theta_p) + a_S \cos(k_q x - \omega_q t + \theta_q), \tag{1.7}$$

with amplitudes a_p and a_q, wavenumbers k_p and k_q, frequencies ω_p and ω_q, and phases θ_p and θ_q, will exhibit amplitude modulation when the three sinusoids are triadically consistent, i.e.,

$$k_L = k_q - k_p, \tag{1.8}$$

$$\omega_L = \omega_q - \omega_p. \tag{1.9}$$

This occurs because the small scale signal can be rewritten as

$$u_S = 2a_S \cos\left(\frac{k_q - k_p}{2} - \frac{\omega_q - \omega_p}{2} + \frac{\theta_q - \theta_p}{2}\right) \cdot \cos\left(\frac{k_q + k_p}{2} - \frac{\omega_q + \omega_p}{2} + \frac{\theta_q + \theta_p}{2}\right). \tag{1.10}$$

When the condition of triadic consistency is satisfied, the first sinusoid, the envelope of the signal, has a consistent temporal phase difference,

$$\Delta\theta = (\theta_q - \theta_p - \theta_L)/\omega_L, \tag{1.11}$$

with the large scale signal, resulting in a correlation coefficient R_{pq} of

$$R_{pq} = \cos(\Delta\theta). \tag{1.12}$$

Furthermore, Duvvuri and McKeon authors probed the phase organization between scales by perturbing a boundary layer with an oscillating transverse rib, introducing a strong synthetic large-scale mode into the flow. A new correlation coefficient, analogous to R above but associated with just the synthetic component of the large-scale signal, was defined as in Equation 1.13. Here tildes refer to a phase average with a period equal to the oscillation period of the rib.

$$\Psi = \overline{\tilde{u}\tilde{u}_S^2} \Big/ \left(\sqrt{\overline{\tilde{u}^2}} \sqrt{\overline{\tilde{u}_S^2}^2} \right). \tag{1.13}$$

For the two-dimensional, spanwise constant disturbance, the quantity Ψ was found to be near one close to the wall, indicating perfect correlation. Around the critical layer of the flow (the wall-normal location at which the mean velocity is equal to the convection speed of the synthetic mode), Ψ changed abruptly to nearly -1 for nearly a decade of height, indicating perfect anti-correlation. Ψ then increased toward 1 at the edge of the boundary layer. In this way, it was shown that a synthetic

mode organizes the phases of triadically-consistent scales in a quasi-deterministic manner.

Experiments and simulations of rough wall flows have found amplitude modulation of turbulence in the roughness sublayer by superstructures that is qualitatively similar to amplitude modulation in canonical flows. Anderson [2] found that LES of a boundary layer over staggered cubes produced amplitude modulation profiles that are comparable to smooth walls, albeit with large spatial variation below the roughness element height. Pathikonda and Christensen [54] and Awasthi and Anderson [4] both studied amplitude modulation in flow over roughnesses with prominent spanwise heterogeneity which produce low- and high-momentum pathways. Pathikonda and Christensen found a greater amplitude modulation in the rough wall flow compared to a smooth wall, with the strongest correlation occurring within an LMP. Awasthi and Anderson found amplitude modulation within a LMP to be similar to a rough wall without spanwise heterogeneity, while amplitude modulation within an HMP was strongly affected by a change in the local spectral density.

1.8 Approach

The approach taken in the present work will tie together two areas of turbulent shear flow with the goal of shedding light on the challenges of each field by exploiting the strengths of the other. A boundary layer with a simply periodic rough wall presents a perturbation of a canonical flow which is uniquely amenable to experiment. A probe placed at a single point within the boundary layer simultaneously records the signature of the perturbation (as the mean velocity) as well as its organizing effect on the turbulent motions which convect past (as revealed in the instantaneous velocity and its spectrum). Tools primarily used in the study of canonical flows such as amplitude modulation and resolvent analysis can be applied to the "barely rough" wall, even contributing to a computationally cheap low-order model that qualitatively predicts the qualitative features results of non-linear interactions.

Chapter 2 of this thesis will describe the novel design of the rough-wall boundary layer experiments, as well as flow conditions and measurement parameters. In addition, the chapter will introduce notation and methods for decomposing the flow field into Fourier series in the streamwise and spanwise directions and in time. The resolvent operator, its significance, and its numerical calculation are detailed as well.

Chapter 3 will present the measured flow characteristics of the simply-periodic

rough wall boundary layer. Spatially-averaged profiles of time-averaged velocity and velocity statistics reveal the bulk effect of roughness on the boundary layer. The spatially-varying parts of these fields are correlated to the periodic roughness, revealing the direct effect of the roughness on boundary layer physics. In a novel contribution to the field, the spatial variation of the streamwise power spectrum is also correlated to the roughness, showing the modulation of individual scales in the flow by the roughness.

Chapter 4 will relate the spatially-varying mean velocity field of Chapter 3 to the velocity response modes of the resolvent operator with zero frequency. Furthermore, the chapter will contribute a novel exploration of the scaling characteristics of low-order representations of the resolvent operator at zero frequency. Parameters such as the leading singular value of that operator are related to the Navier-Stokes equations to predict asymptotic behavior at extreme wavenumbers and Reynolds numbers.

Chapter 5 will introduce a novel, efficient, low-order model to qualitatively predict the power spectrum modulation measured in Chapter 3. The model limits computational cost by considering only a single pair of convecting wavenumbers and their interactions with a static velocity Fourier mode which has zero frequency and is identical in wavenumber to the roughness. The three wavenumbers are triadically compatible, and each Fourier mode is represented by the most-amplified response mode of the corresponding resolvent operator.

Chapter 6 will summarize the results and conclusions of this thesis, and discuss avenues for future work.

Chapter 2

METHODS

2.1 Notation and Equations of Motion

Equations of Motion

The experimental flow considered in this work is turbulent, incompressible, and uniform in both density and viscosity, so that the evolution of its inner-normalized vector velocity field $\boldsymbol{u}^+ = [u^+, v^+, w^+]^T$ is given by the Navier Stokes equations:

$$\frac{\partial \boldsymbol{u}^+}{\partial t^+} + \boldsymbol{u}^+ \cdot \nabla \boldsymbol{u}^+ = -\nabla p^+ + \frac{1}{Re_\tau}\nabla^2 \boldsymbol{u}^+, \tag{2.1}$$

$$\nabla \cdot \boldsymbol{u}^+ = 0. \tag{2.2}$$

Here p is the thermodynamic pressure divided by density, and u^+,v^+,w^+ represent the velocity components in the streamwise (x), wall-normal (y), and spanwise (z) directions, respectively, all normalized by inner units and the boundary layer thickness δ.

Double Decomposition of Field Variables

The full time series of streamwise velocity at a given spatial location and time, $u(x, y, z, t)$, can be decomposed via the usual Reynolds decomposition into a temporally-averaged mean component denoted by an overbar, $\bar{u}(x, y, z)$, and a zero-mean fluctuating component relative to that mean, $u'(x, y, z, t)$, i.e.,

$$u(x, y, z, t) = \bar{u}(x, y, z) + u'(x, y, z, t), \tag{2.3}$$

with

$$\bar{u}(x, y, z) = \frac{1}{\tau}\int_0^\tau u \, \mathrm{d}t, \tag{2.4}$$

and

$$u'(x, y, z, t) = u(x, y, z, t) - \bar{u}(x, y, z). \tag{2.5}$$

Alternatively, data taken in a spatially-periodic flow at the same y-location but at different (x, z) coordinates can be decomposed into a spatial average over a full wavelength of the flow (denoted by angle brackets), $\langle u \rangle(y, t)$, as in Equation 2.6, (with λ_x and λ_z representing the streamwise and spanwise wavelengths of the flow, respectively) and a spatial fluctuation, $\tilde{u}(x, y, z, t)$ defined in Equation 2.7.

$$\langle u \rangle(y, t) = \frac{1}{\lambda_x \lambda_z}\int_0^{\lambda_x}\int_0^{\lambda_z} u(x, y, z, t) \, \mathrm{d}z \, \mathrm{d}x. \tag{2.6}$$

$$\tilde{u}(x,y,z,t) = u(x,y,z,t) - \langle u \rangle (y,t). \tag{2.7}$$

The two decompositions can be combined to give a description of the full streamwise velocity field in terms of a spatio-temporal average, $\langle \bar{u} \rangle (y)$, the time-independent spatial variation from that average, $\tilde{\bar{u}}(x,y,z)$, a fluctuation that is a function of distance from the wall and time, but common to the whole roughness unit, $\langle u' \rangle (y,t)$, and a spatially and temporally varying fluctuation, $\tilde{u}'(x,y,z,t)$, i.e., Equation 2.8.

$$u(x,y,z,t) = \langle \bar{u} \rangle (y) + \tilde{\bar{u}}(x,y,z) + \langle u' \rangle (y,t) + \tilde{u}'(x,y,z,t). \tag{2.8}$$

The full time- and spatial-decomposition of Equation 2.8 was introduced by Pedras et al. [55] for use in porous flow and is also commonly used in studies of spatially heterogeneous flows such as riverbed roughness [57]. It differs from the phase-average decomposition of Hussain and Reynolds [27] in that the spatial fluctuation terms with a tilde are defined and calculated as the difference between the spatial average and the whole field over a single period. Assuming a non-developing flow (no streamwise change in spanwise- and temporally-averaged flow quantities) and a sufficient number of observed periods, this term should be identical to a spatial phase average. Because measurements were taken with only a single hot-wire, i.e., with separate spatial and temporal resolution, the two time-varying terms $\langle u' \rangle$ and $\tilde{u}'$ cannot be distinguished and are gathered together as u' in Equation 2.9, consistent with the definition in Equation 2.5.

$$u(x,y,z,t) = \langle \bar{u} \rangle (y) + \tilde{\bar{u}}(x,y,z) + u'(x,y,z,t). \tag{2.9}$$

Expanding the momentum equation (Equation 2.1) for a zero pressure gradient flow using the triple decomposition of Equation 2.9 and performing spatial (streamwise and spanwise) and temporal averaging gives the expression for the spatio-temporal average velocity, $\langle \overline{\mathbf{u}} \rangle$, Equation 2.10.

$$< \overline{\boldsymbol{u}}^+ > \cdot \nabla < \overline{\boldsymbol{u}}^+ > + < \tilde{\overline{\boldsymbol{u}}}^+ \cdot \nabla \tilde{\overline{\boldsymbol{u}}}^+ > + < \overline{\boldsymbol{u}'^+ \cdot \nabla \boldsymbol{u}'^+} > = \frac{1}{Re_\tau} \nabla^2 < \overline{\boldsymbol{u}}^+ > . \tag{2.10}$$

Subtracting this space- and time- averaged Equation 2.10 from the time-averaged equation gives the relation for the spatially-varying mean field, Equation 2.11:

$$\tilde{\overline{\boldsymbol{u}}}^+ \cdot \nabla < \overline{\boldsymbol{u}}^+ > + < \overline{\boldsymbol{u}}^+ > \cdot \nabla \tilde{\overline{\boldsymbol{u}}}^+ + \widetilde{\tilde{\overline{\boldsymbol{u}}}^+ \cdot \nabla \tilde{\overline{\boldsymbol{u}}}^+} + \widetilde{\overline{\boldsymbol{u}'^+ \cdot \nabla \boldsymbol{u}'^+}} = -\nabla \tilde{\overline{p}}^+ + \frac{1}{Re_\tau} \nabla^2 \tilde{\overline{\boldsymbol{u}}}^+ . \tag{2.11}$$

The equivalent expression for the fluctuating velocity field is obtained by subtracting the time average from the full Navier-Stokes momentum equation to give Equation 2.12:

$$\frac{\partial \boldsymbol{u}'^{+}}{\partial t^{+}} = -\nabla p'^{+} + \frac{1}{Re_\tau}\nabla^2 \boldsymbol{u}'^{+} - < \overline{\boldsymbol{u}}^{+} > \cdot \nabla \boldsymbol{u}'^{+} - \boldsymbol{u}'^{+} \cdot \nabla < \overline{\boldsymbol{u}}^{+} > \\ - \tilde{\overline{\boldsymbol{u}}}^{+} \cdot \nabla \boldsymbol{u}'^{+} - \boldsymbol{u}'^{+} \cdot \nabla \tilde{\overline{\boldsymbol{u}}}^{+} - \boldsymbol{u}'^{+} \cdot \nabla \boldsymbol{u}'^{+} + \overline{\boldsymbol{u}'^{+} \cdot \nabla \boldsymbol{u}'^{+}}. \quad (2.12)$$

The associated forms of the continuity equations are

$$\nabla \cdot \langle \overline{\mathbf{u}}^{+} \rangle = 0, \quad (2.13)$$

$$\nabla \cdot \tilde{\overline{\mathbf{u}}}^{+} = 0, \quad (2.14)$$

$$\nabla \cdot \mathbf{u}'^{+} = 0. \quad (2.15)$$

Fourier Transform

A field quantity $Q(x, y, z, t)$ can be transformed by applying a Fourier transform in x, z, and t to yield the Fourier mode $\hat{Q}(y; \boldsymbol{K})$ with the wavenumber-frequency triplet $\boldsymbol{K} = (k, m, \omega)$ containing the streamwise wavenumber k, spanwise wavenumber m, and angular frequency ω, defined in Equation 2.16:

$$Q(x, y, z, t) = \int_{-\infty}^{\infty}\int_{-\infty}^{\infty}\int_{-\infty}^{\infty} \hat{Q}(y; \boldsymbol{K} = (k, m, \omega)) e^{i(kx+mz-\omega t)} \, \mathrm{d}k \, \mathrm{d}m \, \mathrm{d}\omega. \quad (2.16)$$

Applying the Fourier transform of Equation 2.16 to Equation 2.12 yields expressions for the velocity Fourier modes, Equations 2.17 and 2.18:

$$-i\omega \hat{\boldsymbol{u}}^{+}(y; \boldsymbol{K}) = -\nabla_K \hat{p}^{+}(y; \boldsymbol{K}) + \frac{1}{Re_\tau}\nabla_K^2 \hat{\boldsymbol{u}}^{+}(y; \boldsymbol{K}) - < \overline{\boldsymbol{u}} >^{+} \cdot \nabla_K \hat{\boldsymbol{u}}^{+}(y; \boldsymbol{K}) \\ - \hat{\boldsymbol{u}}^{+}(y; \boldsymbol{K}) \cdot \nabla_K < \overline{\boldsymbol{u}}^{+} > - \int_{\boldsymbol{K_1}} \hat{\boldsymbol{u}}^{+}(y; \boldsymbol{K - K_1}) \cdot \nabla_{K_1} \hat{\boldsymbol{u}}^{+}(y; \boldsymbol{K_1}), \quad (2.17)$$

$$\nabla_K \cdot \hat{\boldsymbol{u}}^{+}(y; \boldsymbol{K}) = 0. \quad (2.18)$$

Here the operator $\nabla_K \equiv (ik, \partial_y, im)^T$ is the spatial ∇, Fourier-transformed in x and z, and we have absorbed into the final integral all terms which are nonlinear with respect to a perturbation to the spatio-temporal average, i.e. we do not explicitly separate interactions including $\tilde{\overline{\boldsymbol{u}}}$.

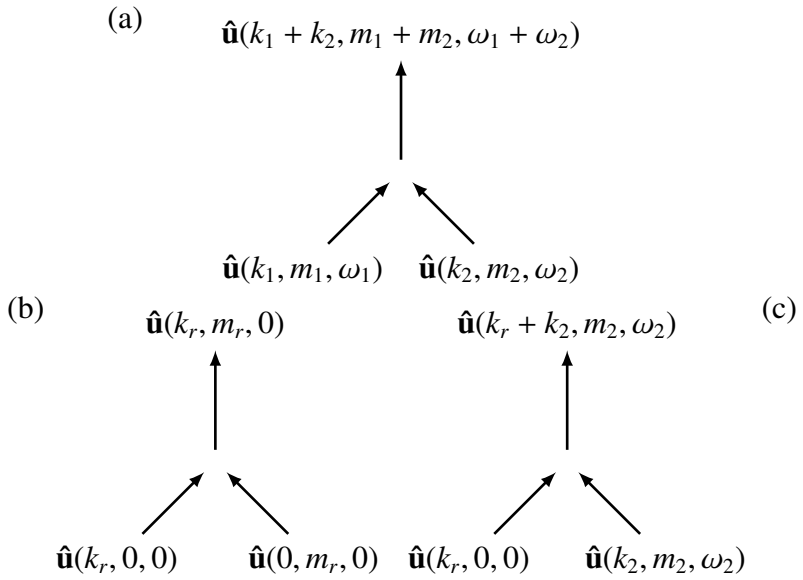

Figure 2.1: Representation of nonlinear interactions between triadically consistent velocity modes, (a) for the canonical case, where $k_1, k_2, m_1, m_2, \omega_1, \omega_2 \neq 0$, (b) for the case of periodic roughness, where direct interactions give rise to a stationary response, for example the interactions of the velocity response at roughness wavenumbers $(k_r, 0, 0)$ and $(0, m_r, 0)$ giving rise to a response at $(k_r, m_r, 0)$, and (c) again for periodic roughness, for the case of a static mode and a spatio-temporally varying one giving rise to a response at a spatio-temporally varying $\mathbf{K}$.

Triadic Interactions

The expression $\hat{\boldsymbol{u}}(y; \boldsymbol{K})$ can be interpreted as the wall-normal (complex) variation of wave-like spatio-temporally varying velocity modes with streamwise, spanwise and temporal wavenumbers given by $\boldsymbol{K}$. The last term in Equation 2.17 accounts for nonlinear interactions coupling between such modes to give a response at $\boldsymbol{K}$. These interactions can be effectively described in terms of triads; for a pair of modes with wavevectors $\boldsymbol{K_1}$ and $\boldsymbol{K_2}$ to interact with a mode with wavevector $\boldsymbol{K}$, they must be triadically-consistent, i.e. $\boldsymbol{K_1} + \boldsymbol{K_2} = \boldsymbol{K}$. This triadic relation is illustrated for the canonical case in Figure 2.1(a), where $k_1, k_2, m_1, m_2, \omega_1, \omega_2 \neq 0$, i.e. all deviations from the mean have non-zero spatial and temporal variations. The full nonlinear term at $\boldsymbol{K}$ corresponds to the integral over all triadically consistent pairs.

In the case of a periodic roughness geometry, additional nonlinear interactions must be considered. Equation 2.11 for the spatial variation, correlated to the roughness geometry, contains nonlinear interactions between static spatial variations and a static variation arising from the interactions of fluctuations, through the last two terms on the left hand side. The former corresponds to Figure 2.1(b) and the latter

corresponds to Figure 2.1(a) with $(k_1, m_1, \omega_1) + (k_2, m_2, \omega_2) = (k_r, m_r, 0)$

An additional category of nonlinear interaction between the fluctuation and the static spatial variation must also be considered. This can also be expressed in terms of triadic interactions with one interacting leg required to arise from the description of $\tilde{\tilde{\boldsymbol{u}}}$. This kind of interaction is sketched for the roughness mode $\boldsymbol{K} = (k_r, 0, 0)$, where k_r is the streamwise roughness wavenumber of this study, in Figure 2.1(c). The full contribution to the nonlinear term in the fluctuation equation associated with the stationary roughness geometry will be given by the integral over $\mathbf{K_1}$ and the static roughness modes.

2.2 Resolvent Analysis

To facilitate low-order modeling of the dynamics of a rough-wall boundary layer, the resolvent framework of McKeon and Sharma [43] is employed to identify physically-relevant velocity modes which are periodic in time and in the streamwise and spanwise directions and which have a defined amplitude and phase distribution in the wall-normal direction. To identify these modes, the linear part of the Navier-Stokes equations 2.17 is first cast in velocity-vorticity form to eliminate pressure, following Schmid and Henningson [63] and Rosenberg et al. [61]. Taking $\langle \overline{u} \rangle$ as streamwise-only, streamwise- and spanwise-constant base flow, Equations 2.17 and 2.18 may be cast in component-wise form as in Equations 2.19-2.22, where $\boldsymbol{f} = [f_x, f_y, f_z]^T$ represents the non-linear terms associated with each component of the momentum equation.

$$-i\omega\hat{u}^+ + ik\langle\overline{u}^+\rangle\hat{u}^+ + \hat{v}^+\partial_y\langle\overline{u}^+\rangle + ik\hat{p}^+ - \frac{1}{Re_\tau}\nabla^2_{\boldsymbol{K}}\hat{u}^+ = \hat{f}_x{}^+. \tag{2.19}$$

$$-i\omega\hat{v}^+ + ik\langle\overline{u}^+\rangle\hat{v}^+ + \partial_y p^+ - \frac{1}{Re_\tau}\nabla^2_{\boldsymbol{K}}\hat{v}^+ = \hat{f}_y{}^+. \tag{2.20}$$

$$-i\omega\hat{w}^+ + ik\langle\overline{u}^+\rangle\hat{w}^+ + im\hat{p}^+ - \frac{1}{Re_\tau}\nabla^2_{\boldsymbol{K}}\hat{w}^+ = \hat{f}_z{}^+. \tag{2.21}$$

$$ik\hat{u}^+ + \partial_y\hat{v}^+ + im\hat{w}^+ = 0. \tag{2.22}$$

We next define the wall-normal vorticity η as in Equation 2.23, which, in combination with continuity (Equation 2.22), allows the elimination of pressure from the momentum equation.

$$\hat{\eta} = im\hat{u}^{+} - ik\hat{w}^{+}. \tag{2.23}$$

Introducing $b^2 = k^2 + m^2$ for brevity, the velocity-vorticity form of the Navier-Stokes Equation can then be written as in Equation 2.24, with operators M, L, and B defined as in Equations 2.25-2.29.

$$-i\omega M \begin{bmatrix} \hat{v} \\ \hat{\eta} \end{bmatrix} + L \begin{bmatrix} \hat{v} \\ \hat{\eta} \end{bmatrix} = B \begin{bmatrix} \hat{f}_x^{+} \\ \hat{f}_y^{+} \\ \hat{f}_z^{+} \end{bmatrix}. \tag{2.24}$$

$$M = \begin{bmatrix} b^2 - \partial_y^2 & 0 \\ 0 & 1 \end{bmatrix}. \tag{2.25}$$

$$L = \begin{bmatrix} L_{OS} & 0 \\ im\partial_y\langle\overline{u}\rangle & L_{SQ} \end{bmatrix}. \tag{2.26}$$

$$L_{OS} = ik\langle\overline{u}\rangle(b^2 - \partial_y^2) + ik\partial_y^2\langle\overline{u}\rangle + \frac{1}{Re_\tau}(b^2 - \partial_y^2)^2. \tag{2.27}$$

$$L_{SQ} = ik\langle\overline{u}\rangle + \frac{1}{Re_\tau}(b^2 - \partial_y^2). \tag{2.28}$$

$$B = \begin{bmatrix} -ik\partial_y & -b^2 & -im\partial_y \\ im & 0 & -ik \end{bmatrix}. \tag{2.29}$$

For a discretization scheme with N points in the y direction, each submatrix of M, L, and B represented by a single entry above will be an N by N matrix. Scalars such as k or m are implicitly multiplied by an N by N identity matrix, while quantities such as $\langle\overline{u}\rangle$ which vary with y are diagonalized. Differentiation with respect to y, ∂_y, is accomplished via an N by N differentiation matrix appropriate to the discretization. The submatrices L_{OS} and L_{SQ} defined in Equations 2.27 and 2.28 are called the Orr-Sommerfeld and Squire operators, respectively.

Equation 2.24 can be rearranged into the input-output form of Equation 2.30, casting the wall-normal velocity and vorticity as the output of an operator, H, defined in Equation 2.31, which is forced by non-linear terms $M^{-1}B\boldsymbol{f}$. The explicit inclusion of the non-linear terms ensures that Equation 2.32 is exactly equivalent to the

Navier Stokes equations for incompressible zero-pressure gradient boundary layers of Equations 2.19- 2.22.

$$\begin{bmatrix} \hat{v} \\ \hat{\eta} \end{bmatrix} = (-i\omega + M^{-1}L)^{-1} M^{-1} B \begin{bmatrix} \hat{f}_x^{+} \\ \hat{f}_y^{+} \\ \hat{f}_z^{+} \end{bmatrix}. \tag{2.30}$$

$$H = (-i\omega + M^{-1}L)^{-1}. \tag{2.31}$$

$$\begin{bmatrix} \hat{v} \\ \hat{\eta} \end{bmatrix} = HM^{-1}B \begin{bmatrix} \hat{f}_x^{+} \\ \hat{f}_y^{+} \\ \hat{f}_z^{+} \end{bmatrix}. \tag{2.32}$$

Given such an input-output relationship, it is useful to perform a modal decomposition of the operator to identify which velocity modes are preferentially amplified. One choice, the singular value decomposition (SVD), requires a norm to quantify the amplification of a mode. In this work, we will use a kinetic energy norm as defined in Equation 2.33, where W is a diagonal matrix appropriate to the discretization. For use with the velocity-vorticity formulation, the associated velocity Fourier distributions $\hat{u}$, $\hat{v}$, and $\hat{w}$ must first be related to the velocity-vorticity phase vector via matrix C, defined in Equation 2.34. The appropriate weighting matrix for calculating the norm of velocity-vorticity state vectors is therefore $Q = C^* W C$, as shown in Equation 2.35.

$$\int_0^\infty |\hat{u}|^2 + |\hat{v}|^2 + |\hat{w}|^2 \, \mathrm{d}y = \begin{bmatrix} \hat{u}^* & \hat{v}^* & \hat{w}^* \end{bmatrix} W \begin{bmatrix} \hat{u} \\ \hat{v} \\ \hat{w} \end{bmatrix}. \tag{2.33}$$

$$\begin{bmatrix} \hat{u} \\ \hat{v} \\ \hat{w} \end{bmatrix} = \frac{1}{b^2} \begin{bmatrix} ik\partial_y & -im \\ b^2 & 0 \\ im\partial_y & ik \end{bmatrix} \begin{bmatrix} \hat{v} \\ \hat{\eta} \end{bmatrix} = C \begin{bmatrix} \hat{v} \\ \hat{\eta} \end{bmatrix}. \tag{2.34}$$

$$\int_0^\infty |\hat{u}|^2 + |\hat{v}|^2 + |\hat{w}|^2 \, \mathrm{d}y = \begin{bmatrix} \hat{v}^* & \hat{\eta}^* \end{bmatrix} C^* W C \begin{bmatrix} \hat{v} \\ \hat{\eta} \end{bmatrix} = \begin{bmatrix} \hat{v}^* & \hat{\eta}^* \end{bmatrix} Q \begin{bmatrix} \hat{v} \\ \hat{\eta} \end{bmatrix}. \tag{2.35}$$

A generalized singular value decomposition (GSVD) [34] is performed in order to identify modes which are highly amplified by the resolvent operator H. The goal

is to decompose the operator into the product of three matrices. The matrices will yield sets of input modes and output modes, with each set being orthonormal under the energy norm, as well as a set of singular values which quantify the amplification the operator applies when acting on a given input mode to produce its corresponding output mode. The calculation starts by performing the standard SVD (using the built-in MATLAB function svd) on a transformed resolvent $Q^{1/2}HQ^{-1/2}$, as shown in Equation 2.36, resulting in orthonormal matrices α and β and the diagonal matrix of singular values Σ.

$$\alpha\Sigma\beta^* = Q^{1/2}HQ^{-1/2}. \tag{2.36}$$

$$\beta^*\beta = \alpha^*\alpha = I. \tag{2.37}$$

The output and input matrices of the GSVD, ψ and ϕ respectively, are defined as shown in Equations 2.38 and 2.39, so that, from Equations 2.37, they are orthonormal by the energy norm. The resolvent H can then be represented in terms of ψ and ϕ as in Equation 2.41. Applying this to Equation 2.32 yields the expression in Equation 2.42. This expression may be interpreted as follows: the rightmost part, $\phi^*QB\hat{f}$, is the projection of the nonlinear forcing onto the input modes ϕ. The complex coefficients of the resulting set of input modes are then multiplied by the singular value corresponding to each mode to become the coefficients for the appropriate output modes.

$$\psi = Q^{-1/2}\alpha. \tag{2.38}$$

$$\phi = Q^{-1/2}\beta. \tag{2.39}$$

$$\psi^*Q\psi = \phi^*Q\phi = I. \tag{2.40}$$

$$H = \psi\Sigma\phi^*Q. \tag{2.41}$$

$$\begin{bmatrix}\hat{v}\\ \hat{\eta}\end{bmatrix} = \psi\Sigma\phi^*QM^{-1}B\hat{f}. \tag{2.42}$$

Quadrature points and weights are generated for a domain $\check{y} \in [-1, 1]$ using Driscoll et al.'s clencurt MATLAB function [16] for Clenshaw-Curtis quadrature. The points and weights are then transformed into the semi-infinite domain suitable to boundary layers, $y \in [0, \infty)$, using the algebraic expression of Equation 2.43

$$y = \frac{1 + \check{y}}{1 - \check{y}}. \tag{2.43}$$

Differentiation matrices in $\check{y}$ were constructed using Weideman and Reddy's chebdif and cheb4c MATLAB functions [73], which enforce the boundary conditions on v and η,

$$\hat{v}(0) = \hat{v}(\infty) = \hat{v}(0) = \hat{v}(\infty) = \hat{\eta}(0) = \hat{\eta}(\infty). \tag{2.44}$$

Differentiation matrices of order n in y, ∂^n, were constructed from differentiation matrices in $\check{y}$, $\partial^n_{\check{y}}$, by application of the chain rule, resulting in

$$\begin{aligned}
\partial^1 =& \frac{\mathrm{d}y}{\mathrm{d}\check{y}}\partial^1_{\check{y}}, \\
\partial^2 =& \left(\frac{\mathrm{d}y}{\mathrm{d}\check{y}}\right)^2 \partial^2_{\check{y}} + \frac{\mathrm{d}^2 y}{\mathrm{d}\check{y}^2}\partial^1_{\check{y}}, \\
\partial^4 =& \left(\frac{\mathrm{d}y}{\mathrm{d}\check{y}}\right)^4 \partial^4_{\check{y}} + 6\frac{\mathrm{d}^2 y}{\mathrm{d}\check{y}^2}\left(\frac{\mathrm{d}y}{\mathrm{d}\check{y}}\right)^2 \partial^3_{\check{y}} + \left(4\frac{\mathrm{d}y}{\mathrm{d}\check{y}}\frac{\mathrm{d}^3 y}{\mathrm{d}\check{y}^3} + 3\frac{\mathrm{d}^2 y}{\mathrm{d}\check{y}^2}\right)\partial^2_{\check{y}} + \frac{\mathrm{d}^4 y}{\mathrm{d}\check{y}^4}\partial^1_{\check{y}}.
\end{aligned} \tag{2.45}$$

The number of quadrature points N was chosen to be 400 for calculations in Chapter 5, as this was found to result in sufficient convergence. $N = 800$ points were used in Chapter 4 in order to provide more precision in locating peaks in y.

Incorporation of Rough-Wall Boundary Conditions into the Resolvent Operator

There are multiple non-mutually exclusive methods for incorporating non-smooth-wall boundary conditions into the resolvent operator, at a cost of increased modelling complexity and, potentially, computational expense.

Linearized Boundary Condition

Following Gaster et al. [22], the wall boundary conditions of the Navier-Stokes Equations can be represented for the case of a small-amplitude roughness via asymp-

totic expansion. For a general single-Fourier-mode static roughness with small amplitude a, streamwise wavenumber k_r, spanwise wavenumber m_r, and height h given by

$$h(x,z) = a\cos(k_r x)\cdot\cos(m_r z), \tag{2.46}$$

the no-slip boundary condition at the wall can be given by

$$\begin{bmatrix} \overline{u}^+(x,h(x,z),z) \\ \overline{v}^+(x,h(x,z),z) \\ \overline{w}^+(x,h(x,z),z) \end{bmatrix} = \begin{bmatrix} 0 \\ 0 \\ 0 \end{bmatrix}. \tag{2.47}$$

Expanding the streamwise velocity field $\overline{u}^+$ in powers of a gives

$$\overline{u}^+(x,y,z) = u_0(x,y,z) + au_1(x,y,z) + a^2u_2(x,y,z) + \ldots, \tag{2.48}$$

which can be further expanded using Taylor series in a, i.e.,

$$u_0(x,y,z) = u_0(x,0,z) + y\partial_y u_0(x,0,z) + \ldots, \tag{2.49}$$

to give the following expression:

$$\overline{u}^+(x,h(x,z),z) = u_0(x,0,z) + a(\cos(k_r x)\cos(m_r z)\partial_y u_0(x,0,z) + u_1(x,0,z)) + \cdots = 0. \tag{2.50}$$

At order $O(1)$,

$$u_0(x,0,z) = 0, \tag{2.51}$$

and at order $O(a)$,

$$u_1(x,0,z) = -\cos(k_r x)\cos(m_r z)\partial_y u_0(x,0,z). \tag{2.52}$$

Analogously, the expansion of $\overline{w}^+$ yields similar expressions for $\overline{w}^+$,

$$\overline{w}^{+}(x, h(x,z), z) = w_0(x,0,z) + a(\cos(k_r x)\cos(m_r z)\partial_y w_0(x,0,z) + w_1(x,0,z)) + \cdots = 0, \tag{2.53}$$

w_0,

$$w_0(x,0,z) = 0, \tag{2.54}$$

and w_1,

$$w_1(x,0,z) = -\cos(k_r x)\cos(m_r z)\partial_y w_0(x,0,z). \tag{2.55}$$

The expansion of the wall-normal velocity,

$$\overline{v}^{+}(x, h(x,z), z) = v_0(x,0,z) + a(\cos(k_r x)\cos(m_r z)\partial_y v_0(x,0,z) + v_1(x,0,z)) + \cdots = 0, \tag{2.56}$$

gives a boundary condition for order $O(1)$,

$$v_0(x,0,z) = 0, \tag{2.57}$$

as well as order $O(a)$,

$$v_1(x,0,z) = -\cos(k_r x)\cos(m_r z)\partial_y v_0(x,0,z). \tag{2.58}$$

Applying Equations 2.50, 2.53, and 2.56 to the continuity equation for incompressible flow yields the following expression at order $O(1)$:

$$0 = \partial_x u_0(x,0,z) + \partial_y v_0(x,0,z) + \partial_z w_0(x,0,z). \tag{2.59}$$

Substituting Equation 2.58 and solving for v_1 gives

$$v_1(x,0,z) = \cos(k_r x)\cos(m_r z)\left(\partial_x u_0(x,0,z) - \partial_z w_0(x,0,z)\right). \tag{2.60}$$

At order $O(a)$, continuity gives

$$
\begin{aligned}
0 =& \partial_x \Big(a\cos(k_r x)\cos(m_r z)\partial_y u_0(x,0,z) + u_1(x,0,z) \Big) \\
&+ a\cos(k_r x)\cos(m_r z)\partial_y^2 v_0(x,0,z) + a\partial_y v_1(x,0,z) \\
&+ \partial_z \Big(a\cos(k_r x)\cos(m_r z)\partial_y w_0(x,0,z) + a w_1(x,0,z) \Big).
\end{aligned} \tag{2.61}
$$

Taking the terms with subscript zero to be the spatio-temporally averaged velocity $\langle \overline{\boldsymbol{u}}^+ \rangle$ which is constant in x and z and which obeys symmetry in z, boundary conditions for the velocity components at order $O(a)$ reduce to

$$
u_1(x,0,z) = -\cos(k_r x)\cos(m_r z)\partial_y \langle \overline{u}^+ \rangle, \tag{2.62}
$$

$$
w_1(x,0,z) = 0, \tag{2.63}
$$

$$
v_1(x,0,z) = 0, \tag{2.64}
$$

and

$$
\partial_y v_1(x,0,z) = -a\cos(k_r x)\cos(m_r z)\partial_y^2 \langle \overline{v}^+ \rangle = 0. \tag{2.65}
$$

Applying the definition for vorticity η yields

$$
\eta_1(x,0,z) = m_r \cos(k_r x)\sin(m_r z)\partial_y \langle \overline{u}^+ \rangle. \tag{2.66}
$$

After performing spatial Fourier transforms in the x and z directions, the order $O(a)$ boundary conditions give the boundary conditions for the $(k, m, \omega) = (\pm k_r, \pm m_r, 0)$ resolvent modes, which have zero frequency and are coherent with the roughness. Higher-order terms in the expansion will give boundary conditions for $(k, m, \omega) = (\pm 2k_r, \pm 2m_r, 0), (\pm 2k_r, 0, 0)$, etc. The boundary conditions differ from the smooth-wall case only for static (zero frequency) modes which are harmonic with the roughness, and this difference amounts to a "slip" velocity in the streamwise direction right on the $y = 0$ plane, which must be derived analytically for each wavenumber. The magnitude of this slip boundary condition depends on the slope of the mean velocity profile at the wall, which is not directly available from the experiments. For these reasons, the modified boundary conditions were not implemented for any resolvent calculations in this thesis.

Volume penalization within the resolvent method

Another method of incorporating the rough wall boundary condition into the resolvent was introduced by Luhar and Chavarin [12], using a volume penalization approach that is similar to the immersed boundary method for fluid simulations. The technique sets the zero point of the wall-normal coordinate y at the very lowest point of the roughness. A scalar permeability K is assigned to each point in the volume $y > 0$, which is $<< 1$ within the solid surface of the wall and infinite above the wall. An additional Darcy-type linear body force is added to the momentum equation,

$$\frac{\partial \boldsymbol{u}^+}{\partial t^+} + \boldsymbol{u}^+ \cdot \nabla \boldsymbol{u}^+ = -\nabla p^+ + \frac{1}{Re_\tau}\nabla^2 \boldsymbol{u}^+ - K^{-1}\boldsymbol{u}^+, \tag{2.67}$$

which is linearly proportional to local velocity and the inverse of permeability. While the technique is applicable to general roughness, Luhar and Chavarin consider only streamwise-constant roughness, and this section will reproduce their derivation without extending it to three-dimensional roughness. The inverse permeability K^{-1} will then be a function of y and z, and representable as a sum of Fourier modes in z:

$$K^{-1}(y, z) = \sum_{n=-\infty}^{\infty} a_n(y) \exp(inm_r z). \tag{2.68}$$

The time-average streamwise velocity can be represented in the same way,

$$\overline{u}^+(y, z) = \sum_{n=-\infty}^{\infty} u_n(y) \exp(inm_r z), \tag{2.69}$$

with the other components of mean velocity taken to be zero. Luhar and Chavarin calculate the mean velocity field using an eddy viscosity.

The momentum and continuity equations are Fourier-transformed in space and time,

$$\left(-i\omega + ik\langle\overline{u}^+\rangle + a_0 - \frac{1}{Re_\tau}\nabla^2\right)\hat{\boldsymbol{u}}^+(k,m,\omega) + \nabla\hat{p}(k,m,\omega)$$
$$+\hat{v}^+(k,m,\omega)\partial_y\langle\overline{u}^+\rangle\begin{bmatrix}1\\0\\0\end{bmatrix} + \sum_{\substack{n=-\infty\\n\neq 0}}^{\infty}(a_n + iku_n)\hat{\boldsymbol{u}}^+(k,m-nm_r,\omega)$$
$$+\sum_{\substack{n=-\infty\\n\neq 0}}^{\infty}\left(\hat{v}^+(k,m-nm_r,\omega)\partial_y + inm_r\hat{w}^+(k,m-nm_r,\omega)\right)u_n\begin{bmatrix}1\\0\\0\end{bmatrix} = \begin{bmatrix}\hat{f}_x{}^+(k,m,\omega)\\ \hat{f}_y{}^+(k,m,\omega)\\ \hat{f}_z{}^+(k,m,\omega)\end{bmatrix}, \tag{2.70}$$

giving a similar expression to the smooth wall case with the addition of terms corresponding to the effect of spatially-averaged inverse permeability, a_0, and to interactions between the wall-roughness wavenumbers nm_r and triadically compatible pairs of convecting modes. Defining a four-component phase vector $\hat{\boldsymbol{u}}_s = [\hat{\boldsymbol{u}}, \hat{p}]^T$ for a given wavenumber, multiple four-component phase vectors and their corresponding resolvent operators can be concatenated into Equation 2.71,

$$\begin{bmatrix}\hat{\boldsymbol{u}}_s^+(k,m+n_hm_r,\omega)\\ \vdots\\ \hat{\boldsymbol{u}}_s^+(k,m,\omega)\\ \vdots\\ \hat{\boldsymbol{u}}_s^+(k,m-n_hm_r,\omega)\end{bmatrix} = H_s\begin{bmatrix}\hat{\boldsymbol{f}}_s^+(k,m+n_hm_r,\omega)\\ \vdots\\ \hat{\boldsymbol{f}}_s^+(k,m,\omega)\\ \vdots\\ \hat{\boldsymbol{f}}_s^+(k,m-n_hm_r,\omega)\end{bmatrix}, \tag{2.71}$$

with the multiple-wavenumber resolvent operator H_s operating on a concatenation of four-component forcing vectors $\hat{\boldsymbol{f}}_s = [\hat{\boldsymbol{f}}, 0]^T$. The multiple-wavenumber resolvent operator H_s is defined as

$$H_s = \left(-i\omega\begin{bmatrix}\grave{I} & & & \\ & \ddots & & \\ & & \grave{I} & \\ & & & \ddots \\ & & & & \grave{I}\end{bmatrix} + \begin{bmatrix}\grave{L}_{k,m+n_hm_r,\omega} & F_1 & \dots & \dots & F_{2n_h}\\ F_{-1} & \ddots & & & \vdots\\ \vdots & & \grave{L}_{k,m,\omega} & & \vdots\\ \vdots & & & \ddots & F_1\\ F_{-2n_h} & \dots & \dots & F_{-1} & \grave{L}_{k,m-n_hm_r,\omega}\end{bmatrix}\right)^{-1}, \tag{2.72}$$

with the four-component linearized Navier-Stokes operator $\grave{L}$ defined as

$$\grave{L}_{k,m,\omega} = \begin{bmatrix} -ik\langle\overline{u}^+\rangle + Re_\tau^{-1}\nabla^2 - a_0 & \partial_y\langle\overline{u}^+\rangle & 0 & -ik \\ 0 & -ik\langle\overline{u}^+\rangle + Re_\tau^{-1}\nabla^2 - a_0 & 0 & -\partial_y \\ 0 & 0 & -ik\langle\overline{u}^+\rangle + Re_\tau^{-1}\nabla^2 - a_0 & -im \\ ik & \partial_y & im & 0 \end{bmatrix}, \tag{2.73}$$

and the off-block-diagonal interaction operator F_n as

$$F_n = \begin{bmatrix} a_n + iku_n & \partial_y\langle\overline{u}^+\rangle & inm_r u_n & 0 \\ 0 & a_n + iku_n & 0 & 0 \\ 0 & 0 & a_n + iku_n & 0 \\ 0 & 0 & 0 & 0 \end{bmatrix}. \tag{2.74}$$

While the volume-penalization method seems to incorporate general boundary conditions in a rational manner, it also introduces new complications to the resolvent calculation. The volume penalization method cannot be applied to calculate the resolvent operator for static modes, because it takes the spatially-varying velocity field as an input. The resolvent can be calculated for pairs of convecting modes that are triadically consistent with the roughness, but interpretation of the most-amplified SVD modes requires the assumption that the non-linear forcing is evenly distributed across wavenumbers as well as in y. For these reasons, it was not implemented for any calculations in this thesis.

2D (3D) Resolvent

The work of Gomez et al. [24] provides an additional method of accommodating a spatially-varying boundary condition, by calculating the 2D or 3D resolvent. In this method, the Navier-Stokes equations are Fourier-transformed only in time and (in the 2D case) one wall-parallel direction. The no-slip condition can then be applied in physical space directly by setting the appropriate entries in the phase vector to zero. This method does, however, present additional difficulties. The 2D or 3D resolvents require as a base flow a time-averaged velocity field, so it cannot be consistently applied to calculate a static velocity Fourier mode. Even the calculation of convecting modes presents a problem for the modelling in this thesis, because the convecting modes contain multiple wavenumbers, complicating a comparison to observed energy spectra in the flow. Additionally, the SVD of the 2D resolvent is

computationally expensive, as the resolvent matrix for a domain with N discretization points in the y-direction and N points in another spatial direction will be of size $N^2 \times N^2$, compared to $N \times N$ for the conventional resolvent. This work will employ only the conventional, one-dimensional resolvent operator.

2.3 Experimental Methods

Run Conditions

Experimental rough- and smooth-wall boundary layer experiments were performed in the Merrill wind tunnel at Caltech. The test section of the wind tunnel measures $2440mm$ in the streamwise direction, with a square cross-section that measures $610mm$ on each edge. The boundary layers were developed over an acrylic plate which spans the width of the wind tunnel. The boundary layers are tripped $19mm$ downstream of the parabolic leading edge by a $0.76mm$ diameter piano wire glued to the plate surface, as described by Duvvuri [17]. Hot-wire measurements were taken $1250mm$ downstream of the trip. The pressure gradient is controlled by a deformable ceiling, which is adjustable at ten points along the test section. Freestream velocity U_∞ and velocity profiles were measured with hot-wire anemometry. Momentum thickness θ and 99% thickness δ were calculated directly from the velocity profiles (or spatially-averaged velocity profiles in the case of the rough-wall measurements). The friction velocity u_τ was determined in the smooth case by empirical relations to the momentum thickness. In the rough cases, u_τ was determined by a single iteration of the modified Clauser method [56] as described algorithmically by LeHew [37]. Physically, there is likely spatial variation in the shear stress at the wall, but the result of this calculation is an estimate of spatially-averaged shear stress at the wall, consistent with its definition in the roughness literature. Smooth- and rough-wall run conditions are summarized in Table 2.1. Run conditions were selected to roughly match the friction Reynolds number Re_τ in order to fulfill the conditions for wall similarity given by Raupach et al. [60]. The acceleration parameter $K = \frac{\nu}{4U_\infty^3 \rho}\frac{dp}{dx}$, as defined by DeGraaf and Eaton [15], was of the order 1×10^{-8} for both the smooth and the rough cases, indicating a nominal zero-pressure gradient turbulent boundary layer. In all cases, the spatio-temporally averaged boundary layer statistics were found to vary slowly over a single roughness wavelength, indicating a slowly-developing (quasi-parallel) boundary layer and validating the assumption of streamwise homogeneity in the smooth case and periodic mean flow in the rough cases.

Table 2.1: Run Conditions

Set	U_∞ (m/s)	δ (mm)	ν (m^2/s)	θ (mm)	u_τ (m/s)	Re_δ	Re_τ	Re_θ
Smooth	18.0	24.4	1.53E-05	3.03	0.71	29000	1100	3600
R1M	20.3	23.4	1.56E-05	2.82	0.84	30000	1300	3700
R2M	16.3	24.8	1.56E-05	3.08	0.74	26000	1200	3200

Geometry

Two roughness surfaces were 3D-printed for wind-tunnel testing. The first surface, labeled R1M in Tables 2.1-2.3, was printed with a spatially-varying height $h_{R1M}(x, z)$ consisting of a single Fourier mode of amplitude a which varies in x and z with a single wavelength λ_x and λ_z in each direction, respectively, as given in Equation 2.75. A second roughness surface, labeled R2M, was designed with height $h_{R2M}(x, z)$ consisting of a single streamwise-varying Fourier mode with amplitude a and wavelength λ_x added to a single spanwise-varying Fourier mode with identical amplitude a and wavelength λ_z, as given in Equation 2.76. In each case, the $y = 0$ plane is located at the mean roughness height.

$$h_{R1M}(x, z) = a\cos(2\pi x/\lambda_x) \cdot \cos(2\pi z/\lambda_z). \tag{2.75}$$

$$h_{R2M}(x, z) = a\cos(2\pi x/\lambda_x) + a\cos(2\pi z/\lambda_z). \tag{2.76}$$

The wavelengths, given in Table 2.2, were chosen as a compromise between targeting the observed spectral peak of the near-wall cycle and hot-wire accessibility between peaks. The amplitude of both modes of the roughness was chosen to be approximately 9 viscous units, physically $0.182mm$. This allowed the roughness to obey the previously-cited limitation of k/δ (with roughness height k taken to be twice the roughness amplitude a) for a rough wall while also accommodating the resolution of the 3D-printer. Diagrams of the roughness surfaces with exaggerated amplitude are shown in Figures 2.2a and 2.3a. The 3D-printed surface was mounted into an existing test section in the Merrill wind tunnel at Caltech, with a span of $597mm$ and a length of $1605mm$. Hot-wire measurements were taken $1000mm$ downstream of the leading edge of the roughness. Flow reversal in the measurement domain is not expected, due to the low amplitude and shallow aspect ratio of the roughness.

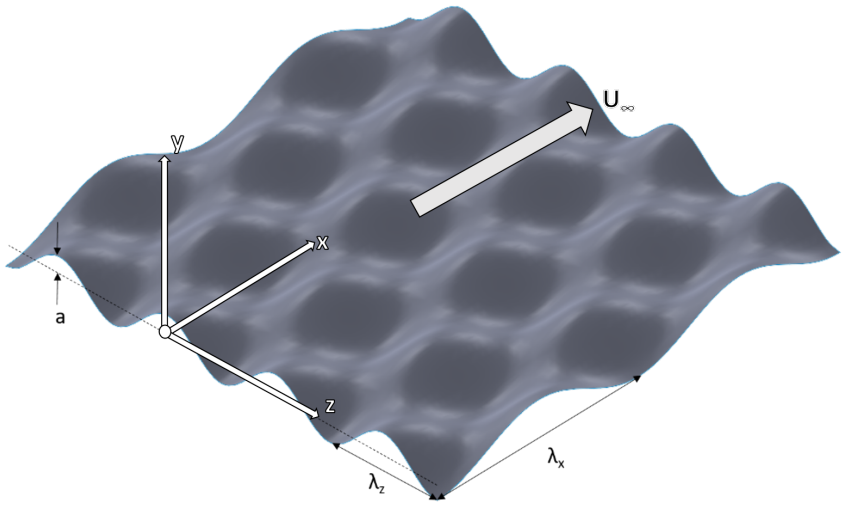

(a) An illustration of the R1M roughness geometry, with exaggerated y-dimension.

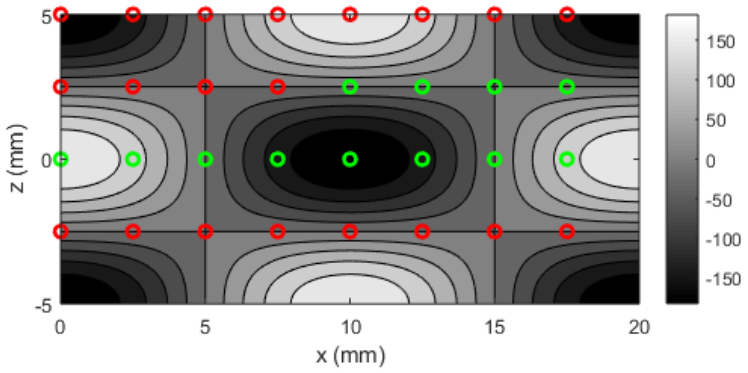

(b) Hot-wire measurement locations within a single streamwise and spanwise wavelength of the roughness. Lighter colors denote higher-than-average roughness elevation, with peaks at y=182 μm, while darker colors denote lower-than-average roughness elevation, with troughs at y=-182 μm. Green circles show the locations of hot-wire traverses in y, while red circles show locations for which the velocity statistics can be imputed from the hot-wire data using symmetries of the roughness geometry.

Figure 2.2: R1M roughness geometry and measurement locations.

Table 2.2: Roughness Geometry Parameters

Set	λ_x (mm)	λ_z (mm)	a (mm)	λ_x^+	λ_z^+	a^+	λ_x/δ	λ_z/δ	a/δ	δ/a
R1M	20	10	0.182	1080	540	10	0.86	0.43	0.008	128
R2M	20	10	0.182	950	475	9	0.81	0.40	0.008	136

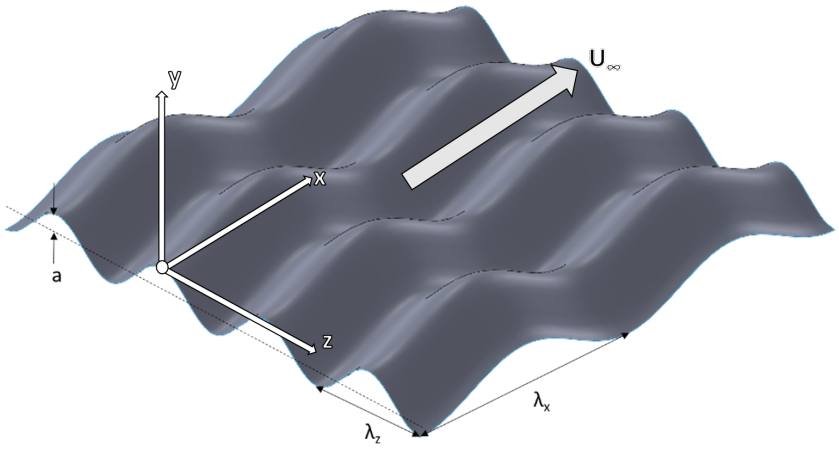

(a) An illustration of the R2M roughness geometry, with exaggerated y-dimension.

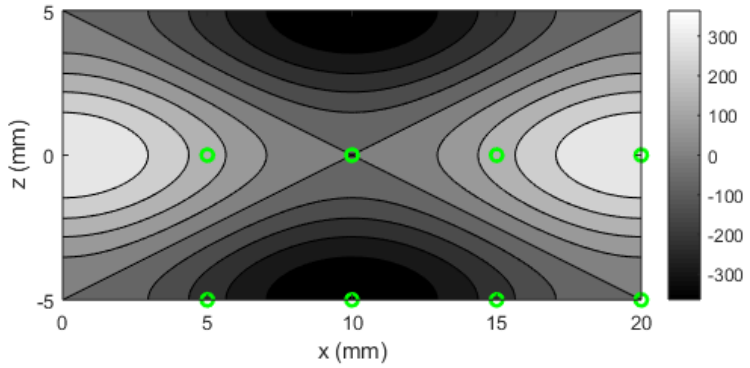

(b) Hot-wire measurement locations within a single streamwise and spanwise wavelength of the roughness. Lighter colors denote higher-than-average roughness elevation, with peaks at y=364 μm, while darker colors denote lower-than-average roughness elevation, with troughs at y=-364 μm. Green circles show the locations of hot-wire traverses in y.

Figure 2.3: R2M roughness geometry and measurement locations

Figure 2.4: R1M traverse hot-wire probe setup. The pressure probe “A” is used for hot-wire calibration in the freestream. The hot-wire probe holder “B” holds a hot-wire probe (not shown). Linear stages “C” and “D” allow for streamwise and spanwise adjustment of the hot-wire probe. The post “E” extends below the roughness surface and is mounted to a powered traverse that allows wall-normal adjustment during the experiment.

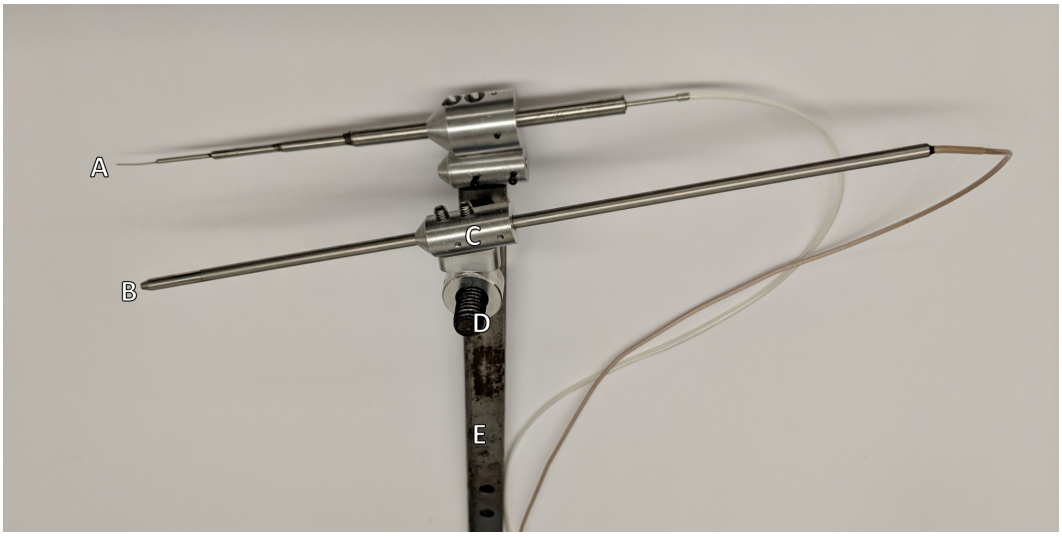

Figure 2.5: R2M traverse hot-wire probe setup. The pressure probe “A” is used for hot-wire calibration in the freestream. The hot-wire probe holder “B” holds a hot-wire probe (not shown). The collar “C” holds the probe holder in place with a set screw, allowing streamwise adjustment. It is mounted on rod “D” with another set screw, allowing for spanwise adjustment of the hot-wire probe. The post “E” extends below the roughness surface and is mounted to a powered traverse that allows wall-normal adjustment during the experiment.

Hot-wire Parameters

Velocity time series were obtained using single normal wire anemometry. A hot-wire probe was mounted on a post, labeled “E” in Figures 2.4 and 2.5, which was

fixed below the test surface and extended through a port cut into the roughness and test section. A traverse allowed measurements at multiple wall-normal distances during a single test run, and the hot wire probe was adjusted between experiments in the streamwise and spanwise directions to alter the position of the measurement volume. For each station and y-location, $100s$ of streamwise velocity data were recorded using a 55P05 boundary-layer type hot-wire probe and Dantec Streamline Pro anemometer, equal to 74,000 eddy turnover times (δ/U_∞). Hot-wire measurement parameters including sampling rate f_s, active length L, active diameter D, and hot-wire low-pass filter cutoff frequency f_c are detailed in Table 2.3 below along with their associated non-dimensional values.

Single-Mode Roughness

For the R1M case, two micrometer-equipped linear stages labeled "C" and "D" were used to adjust the streamwise and spanwise position of the hot-wire probe holder "B" between runs, as shown in Figure 2.4. Twelve wall-normal traverses were performed within a single period of roughness, denoted by green circles in Figure 2.2b. The velocity statistics for twenty additional locations, shown in red circles, can be imputed from the hot-wire data using symmetries of the roughness geometry and the assumption of a non-developing periodic flow. For example, under these assumptions, the red circle located at $(x, z) = (0mm, 5mm)$ is expected to have velocity statistics which are identical to those at the measured location $(x, z) = (10mm, 5mm)$, exploiting the symmetry in this geometry of a $10mm$ streamwise translation combined with a reflection in z. This set of 32 points allows for spatial phase averaging to decompose the field into components directly correlated with the wavenumber content of the roughness. Specifically, performing a Fourier transform of mean velocity $\bar{u}(x, y, z)$ in x and a cosine transform in z (to ensure spanwise symmetry) yields a set of spatial Fourier modes $\hat{\bar{u}}(y, k, m)$, where k is the streamwise wavenumber and m the spanwise wavenumber. Following the Nyquist criterion, one can determine from the eight-by-four grid of data modes with $k = 0, k_r, 2k_r$ and $m = 0, m_z, 2m_r$, where k_r and m_r are the streamwise and spanwise roughness wavenumbers, respectively. A series of time-averaged velocity profile measurements were taken at $10mm$ increments across the span of the tunnel to verify streamwise homogeneity in run conditions around the measurement volume.

The origin of the y-axis is taken to be the spatial average of the roughness height, i.e. h=0 in Equation 2.75. Hot-wire measurements were taken starting at $150\mu m$

above the local roughness height. Spatial averages and spatial Fourier transforms are performed in this paper only for values of y for which data from all measurement stations exist. As a result, the lower bound on y for these quantities is $150\mu m$ above the crest of the roughness, $y = 334\ \mu m = 0.01\delta$. Estimated error for y-positioning of the hot-wire probe is $\pm 9\mu m$. The estimated errors for the (x,z) positioning of the hot-wire are $0.3mm$ in each dimension.

Two-Mode Roughness

For the R2M case, the hotwire probe was adjusted between runs in the streamwise direction by sliding the hot-wire probe holder "B" within its collar "C", while adjustment in the spanwise directions was accomplished by moving the collar along a spanwise rod "D", as shown in Figure 2.5. Eight wall-normal traverses were performed over a single period of roughness, in a grid that spanned four stations in the streamwise direction and two stations in the spanwise direction, as shown in Figure 2.3b. This set of points allows for spatial phase averaging to decompose the field into components directly correlated with the wavenumber content of the roughness. Specifically, performing a Fourier transform of mean velocity $\bar{u}(x, y, z)$ in x and a cosine transform in z (to ensure spanwise symmetry) yields a set of spatial Fourier modes $\hat{\bar{u}}(y, k, m)$, where k is the streamwise wavenumber and m the spanwise wavenumber. Following the Nyquist criterion, one can determine from the four-by-two grid of data modes with $k = 0, k_x$ and $m = 0, k_z$, where k_x and k_z are the streamwise and spanwise roughness wavenumbers, respectively.

The origin of the y-axis is taken to be the spatial average of the roughness height, i.e. h=0 in Equation 2.76. Hot-wire measurements were taken starting at $150\mu m$ above the local roughness height. Spatial averages and spatial Fourier transforms are performed in this paper only for values of y for which data from all measurement stations exist. As a result, the lower bound on y for these quantities is $150\mu m$ above the crest of the roughness, $y = 514\ \mu m = 0.02\delta$. Estimated error for y-positioning of the hot-wire probe is $\pm 40\mu m$. The estimated errors for the (x,z) positioning of the hot-wire are 0.5mm in each dimension.

Table 2.3: Hot-wire acquisition parameters

Set	f_s (kHz)	f_s^+	L (mm)	D (μm)	L/D	L^+	f_c (kHz)	f_c^+
Smooth	60	1.8	1.25	5	250	56	30	0.9
R1M	60	1.3	1.25	5	250	67	30	0.9
R2M	60	1.7	1.25	5	250	60	30	0.7

Chapter 3

EXPERIMENTAL MEASUREMENT OF PERIODIC ROUGH WALL TURBULENT BOUNDARY LAYERS

This chapter will present the measured flow characteristics of the simply periodic rough wall boundary layer. Spatially-averaged profiles of time-averaged velocity and velocity statistics reveal the bulk effect of roughness on the boundary layer. The spatially-varying parts of these fields are correlated to the periodic roughness, revealing the direct effect of the roughness on boundary layer physics. In a novel contribution to the field, the spatial variation of the streamwise power spectrum is also correlated to the roughness, showing the modulation of individual scales in the flow by the roughness.

3.1 Spatio-temporal average flow statistics

The velocity, velocity deficit, and variance profiles for the spatio-temporal averages, i.e. $\langle \bar{u}^+ \rangle(y)$, $U_\infty^+ - \langle \bar{u}^+ \rangle(y)$, and $\langle \overline{u'u'}^+ \rangle(y)$, are shown for the smooth and the rough wall cases in Figures 3.1 and 3.2. For the smooth wall which is homogeneous in x and z, $\langle \bar{Q} \rangle(y) = \bar{Q}(y)$ for all quantities Q. There are significant differences between the spatio-temporal average profiles over the rough and the smooth wall case for both velocity deficit and variance. As would be expected, there is a significant deviation between the profiles close to the wall, but there is also a marked divergence between the two cases well outside the traditional roughness sublayer. For the R1M case, the lack of collapse extends to approximately $y/\delta = 0.4$ for the velocity deficit and $y/\delta = 0.05$ for the variance. The lack of collapse extends through most of the boundary layer until approximately $y/\delta = 0.6$ for the R2M case.

Contrary to the majority of results associated with three-dimensional, multi-scale roughnesses, the influence of the wall is felt far beyond the usual estimate of a roughness sublayer, 5 times the roughness height k [32], which is equal to approximately $y/\delta = 0.08$ for both rough cases. This appears inconsistent with the Townsend hypothesis, which predicts that mean flow quantities and statistics outside the roughness sublayer (a thin layer which is within several roughness heights of the wall) are altered from the smooth case only by the change in u_τ. Townsend's hypothesis requires a separation of scales between the roughness and the boundary layer thickness, usually expressed in terms of the roughness height. Similar to het-

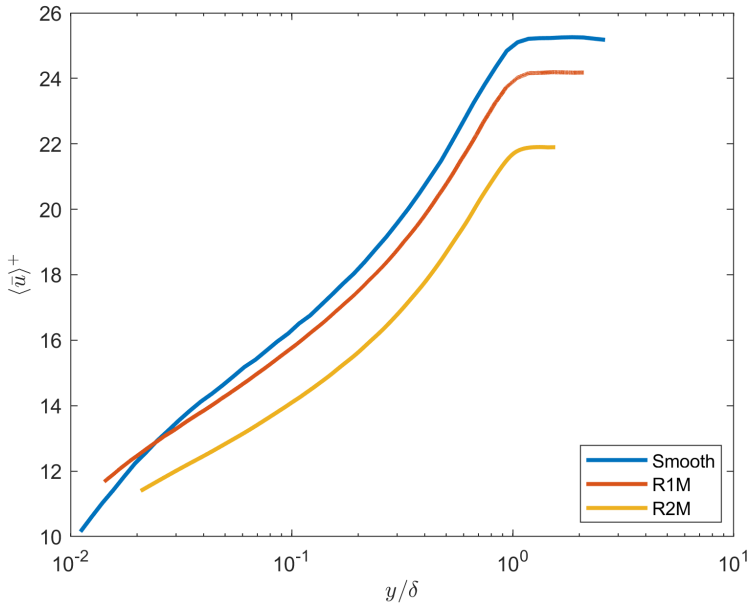

(a)

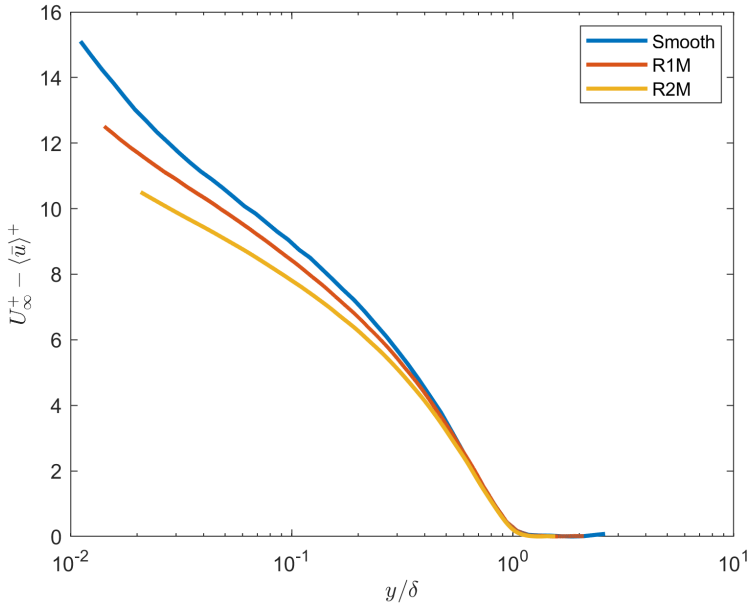

(b)

Figure 3.1: Spatio-temporally averaged (a) velocity profile and (b) velocity deficit profile for smooth and rough wall geometries, as defined in Section 2.3.

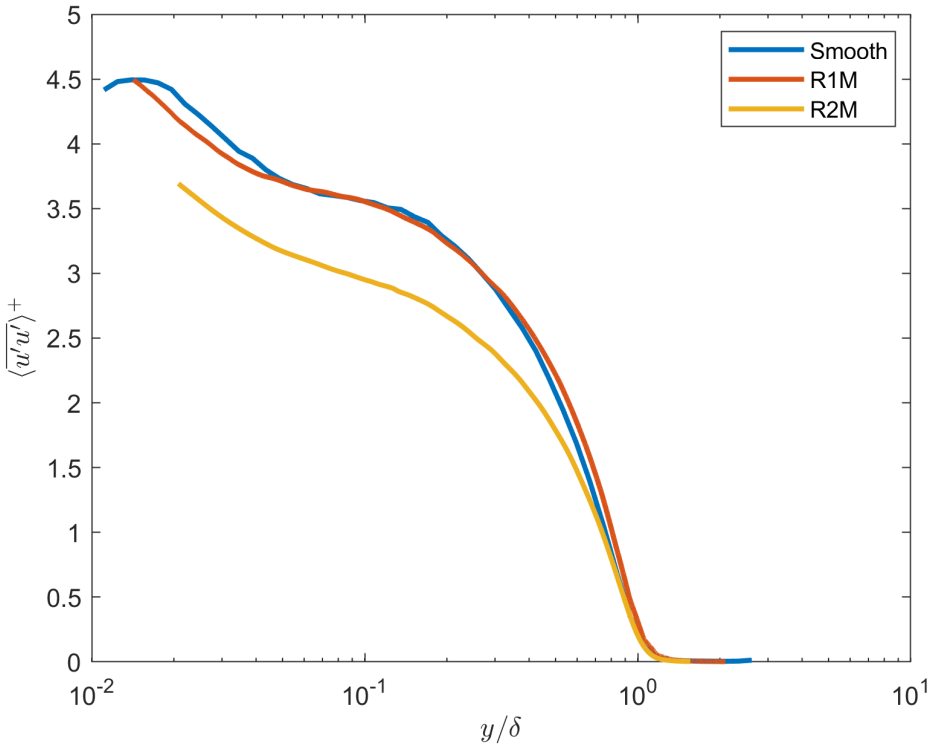

Figure 3.2: Spatio-temporally averaged velocity variance of rough and smooth walls

erogeneous roughnesses with coherence in the streamwise and spanwise directions, this roughness has large length-scales corresponding to the roughness wavelengths. These large length scales are not separated in scale from the boundary layer thickness, so the Townsend hypothesis does not hold. Consistent with Volino et al. [72], the R2M roughness with a spanwise-aligned mode creates the most persistent deviation from Townsend's hypothesis.

3.2 Spatial variation of the time-averaged velocity field

The spatially-averaged quantities shown in Figures 3.1 and Figure 3.2 obscure the secondary flow associated with the roughness, which takes the form of substantial spatial variation in the mean velocity outside the roughness sublayer. By performing a number of traverses at stations separated in x and z within a single period of roughness, at the locations shown in Figures 2.2b and 2.3b, it is possible to map (by spatial interpolation) the streamwise and spanwise variation in the time-averaged velocity, $\tilde{\bar{u}}^{+}(x, y, z)$.

Figures 3.3a and 3.4a show the streamwise velocity $\bar{u}^{+}(x, y, z)$ in the $z = 0$ plane for

both rough geometries, as defined in Figures 2.2b and 2.3b. Color scales are not kept consistent between the two plots because no similarity is expected between two different roughnesses for raw mean velocity (as opposed to the velocity deficit form shown in Figure 3.1b). For the R1M case, this streamwise-aligned plane is one with maximum variation in the roughness height, hitting both absolute maxima and minima. For the R2M case, this is a streamwise-aligned plane that sits over a crest in the spanwise roughness (Figure 2.3). In both geometries, the position $x/\lambda_x = 0$ corresponds to a peak in the streamwise direction while $x/\lambda_x = 0.5$ corresponds to a trough in the streamwise direction. There is clear variation in mean velocity close to the wall, which is made clear by plotting the same data with the spatial average subtracted, $\tilde{\tilde{u}}^+(x, y, z)$, in Figures 3.3b and 3.4b. The pattern in each case is very close to singly-periodic with a wavelength matching the roughness wavelength. Note that the x-averages of the data plotted in Figures 3.3b and 3.4b are not necessarily identically zero, as there are other planes of data which contribute to the spatial average.

In the R1M case, the streamwise and spanwise variation in the time-averaged velocity, $\tilde{\tilde{u}}^+(x, y, z)$, is faster over a trough in the roughness located at $x/\lambda_x = 0.5$ and slower over a peak in roughness located at $x/\lambda_x = 0$. This is consistent with a "profile displacement" model of velocity variation, in which an elevated roughness element displaces a velocity profile upwards, causing lower mean velocities at a given y.

For the R2M case, close to the wall, there is a strong velocity deficit (negative $\tilde{\tilde{u}}^+(x, y, z)$) located on the rising portion of the peak. Further from the wall, velocity deficits sit over troughs while pockets of excess velocity sit over peaks. The placement of positive $\tilde{\tilde{u}}^+(x, y, z)$ over a roughness peak is consistent with a "streamtube deformation" model of velocity variation, in which an elevated roughness element accelerates the flow above it by locally compressing streamtubes. This effect may be more pronounced in the R2M case compared to the R1M case due to its streamwise-constant mode: the streamtubes cannot curve around the spanwise-constant peaks.

3.3 Signature of the roughness geometry in the spatial variation of the time-averaged velocity field

As described in Section 2.3, spatial phase averaging of flow statistics can be used to decompose the field into components directly correlated with the wavenumber content of the roughness. Specifically, performing a Fourier transform of mean velocity

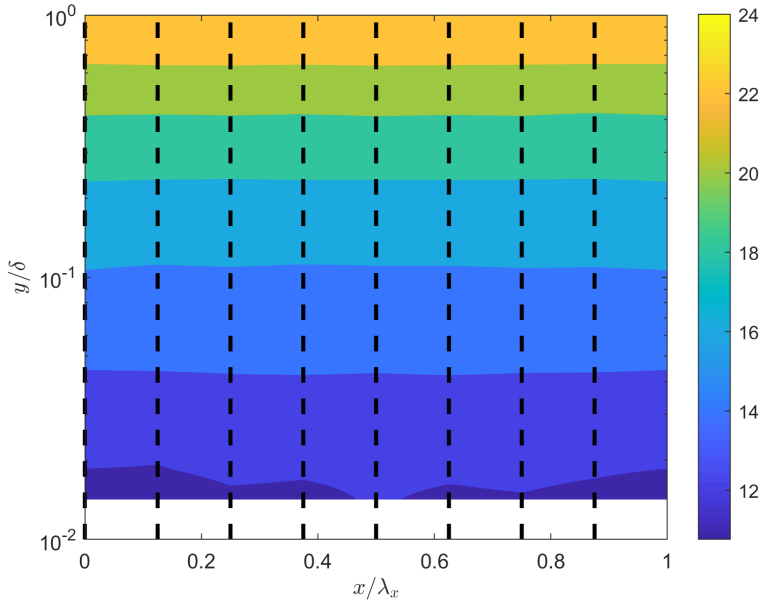

(a)

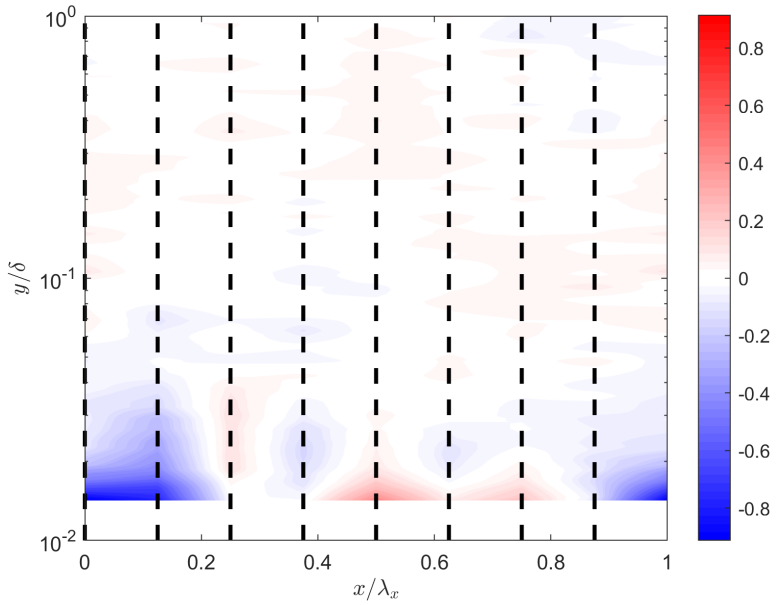

(b)

Figure 3.3: Spatial representations for the R1M case of (a) the mean velocity field $\bar{u}^+(x,y,z)$ on the $z = 0$ plane, (b)the spatial variation in the mean velocity field $\tilde{\bar{u}}^+(x,y,z)$ on the $z = 0$ plane. Red contours indicate a region in which the flow is faster than at other points at the same y-location. Measurement locations at x/λ_x=0,0.125,0.25,0.5,0.625,0.75,0.875 are marked with a dashed line.

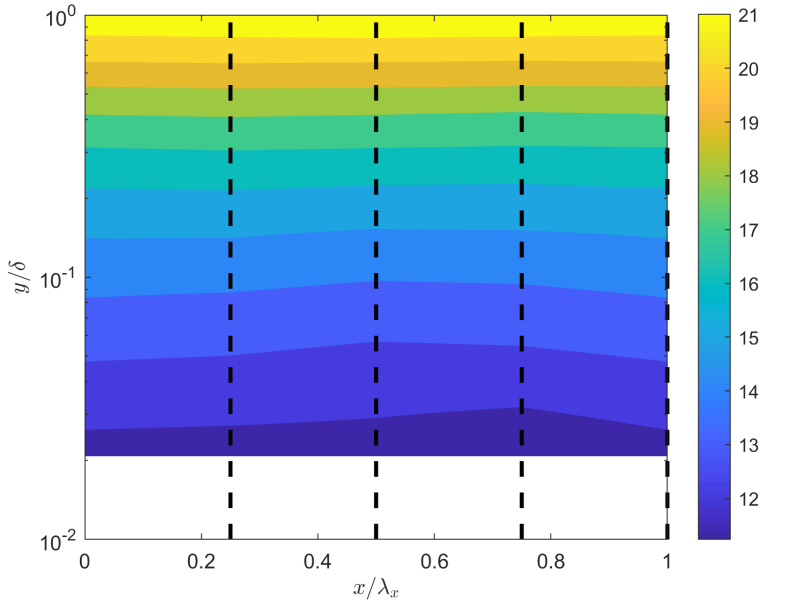

(a)

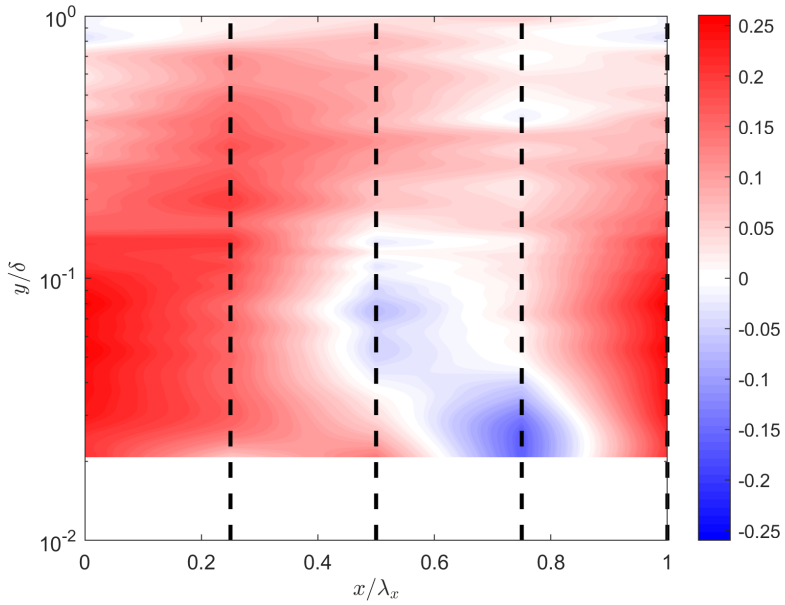

(b)

Figure 3.4: Spatial representations for the R2M case of (a) the mean velocity field $\bar{u}^+(x,y,z)$ on the $z = 0$ plane, (b)the spatial variation in the mean velocity field $\tilde{\bar{u}}^+(x,y,z)$ on the $z = 0$ plane. Red contours indicate a region in which the flow is faster than at other points at the same y-location. Measurement locations at x/λ_x=0.25,0.5,0.75,1 are marked with a dashed line.

$\bar{u}^+(x,y,z)$ in x and a cosine transform in z (to ensure spanwise symmetry) yields a set of stationary velocity Fourier modes $\hat{u}^+(y,k,m,0)$, where k is the streamwise wavenumber and m the spanwise wavenumber, and with zero frequency. Following the Nyquist criterion, one can determine from the eight-by-four grid of data for the R1M case modes with $k = 0, k_r, 2k_r$ and $m = 0, m_z, 2m_r$, where k_r and m_r are the streamwise and spanwise roughness wavenumbers, respectively. The R2M case permits calculation of modes with $k = 0, k_r$ and $m = 0, m_r$. There is no indication of such static velocity modes in smooth-wall data for the same wind tunnel.

Contributions to the R1M spatial variation in mean velocity $\tilde{\bar{u}}^+(x,y,z)$ from resolvable spatial modes are plotted as spatial reconstructions in Figures 3.5a - 3.5d. Modes for which $(k,m) = (k_r,0),(0,m_r)$ contribute identically zero to observed $\tilde{\bar{u}}^+(x,y,z)$ due to symmetry. Stationary velocity mode $\hat{u}^+(y;k_r,m_r,0)$ is the stationary velocity mode with the highest amplitude, reaching 0.54 in inner units at the lower limit of the measurement volume and accounting for most of the spatial variation in mean velocity. This is expected, as this is the only mode with the same frequency content as the roughness, allowing the roughness geometry and this velocity mode to be connected through linear mechanisms. The qualitative features of the full $\tilde{\bar{u}}(x,y,z)$ field are evident in this mode, including the x- and y- locations of the velocity deficits and the change in phase with y. This mode also decays more quickly with y than the other wavenumbers.

Stationary velocity modes $\hat{u}^+(y;2k_r,2m_r,0)$, $\hat{u}^+(y;2k_r,0,0)$,and $\hat{u}^+(y;0,2m_r,0)$ for case R1M are plotted in Figures 3.5b-3.5d. They are substantially weaker than $\hat{u}^+(y;k_r,m_r,0)$, as they can only be formed by non-linear interactions within the flow. Compared to $\hat{u}^+(y;k_r,m_r,0)$, they also decay more slowly in y and have less phase variation. The spanwise-varying-only stationary velocity mode $\hat{u}^+(y;0,2m_r,0)$ is constrained by symmetry from varying continuously in phase, but does notably invert in sign around $y/\delta = 0.05$.

The relative uncertainty in the amplitude of the R1M mode $\hat{u}^+(y;k_r,m_r,0)$ is 6% of the mode amplitude at the lower limit of the measurement volume, and stays below 25% everywhere with significant finite mode amplitude. The relative uncertainty of the other R1M modes are all below 18% of mode amplitudes at the lower limit of the measurement volume, and stay below 33% where the mode amplitudes are significantly non-zero.

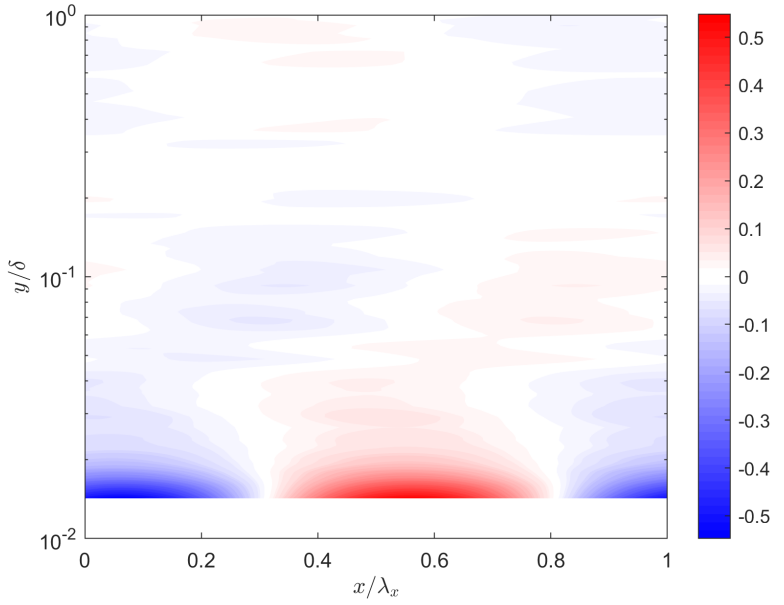

(a)

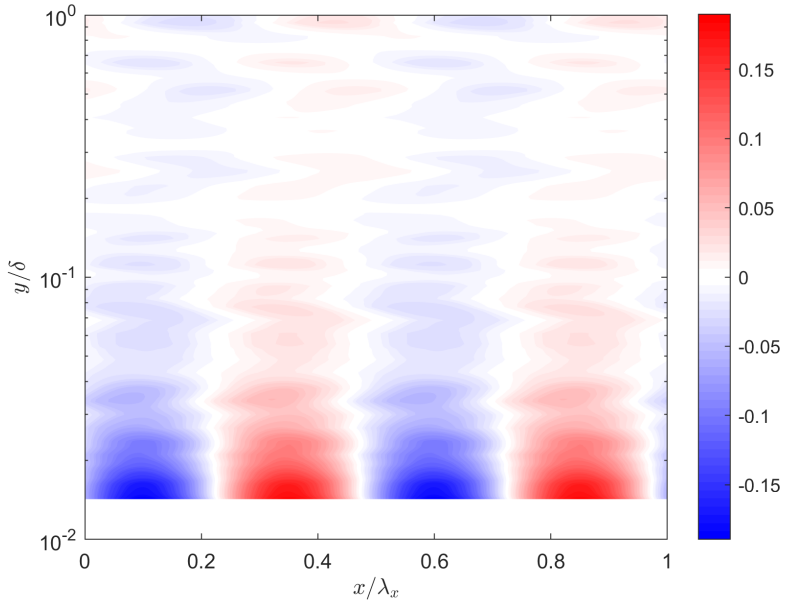

(b)

Contributions to the R2M spatial variation in mean velocity $\tilde{\tilde{u}}(x, y, z)$ from resolvable spatial modes are plotted as spatial reconstructions in Figures 3.6a - 3.6c. For the R2M case, the streamwise-varying-only mode, $\hat{u}^+(y; k_r, 0, 0)$, has the largest amplitude of these modes, as could be anticipated from the blockage effect created by spanwise-constant features. The qualitative features of the full mean velocity field variation over the roughness unit (Figure 3.4b) are also evident in this mode, with its

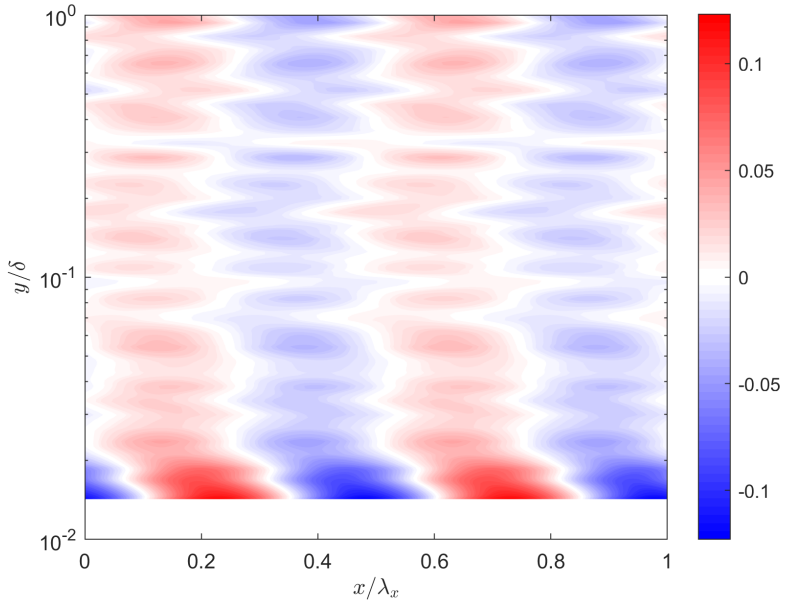

(c)

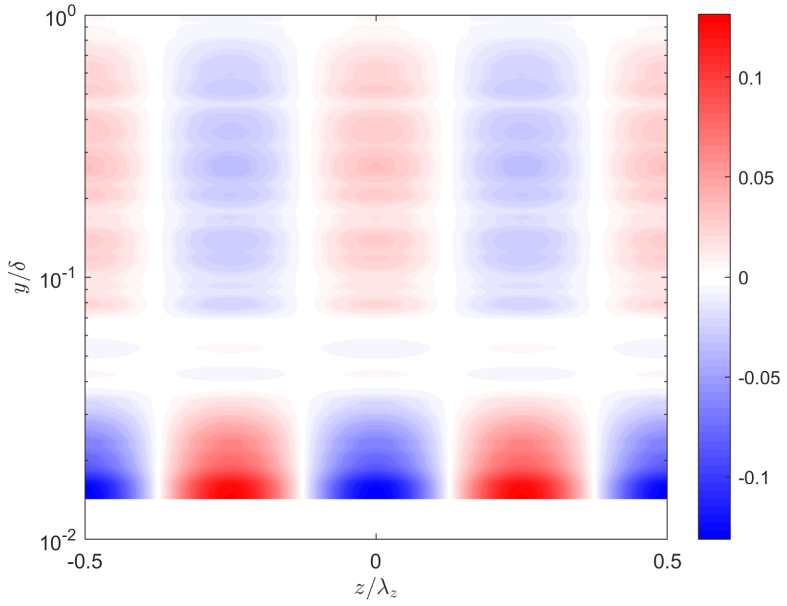

(d)

Figure 3.5: Spatial representations for the R1M case of (a) the stationary velocity Fourier mode $\hat{u}^+(y;k_r,m_r,0)$, (b) the stationary velocity Fourier mode $\hat{u}^+(y,2k_r,2m_r,0)$, (c) the stationary velocity Fourier mode $\hat{u}^+(y,2k_r,0,0)$, and (d) the stationary velocity Fourier mode $\hat{u}^+(y,0,2m_r,0)$. Red contours indicate a region in which the flow is faster than at other points at the same y-location.

amplitude peaking near the wall and the high-speed regions over roughness peaks. The mode $\hat{u}^+(y; k_r, 0, 0)$ attains a maximum amplitude of 0.23 inner units at the lower limit of the measurement volume and decays slowly in amplitude with y. The other stationary velocity mode $\hat{u}^+(y; 0, m_r, 0)$ with a linear connection to the roughness geometry, shown in Figure 3.6b, also has a fairly large amplitude, peaking at 0.11 at $y/\delta = 0.26$. Spanwise symmetry constrains the phase of this mode such that a maximum in velocity must lie directly over either a roughness crest or a roughness trough. In this case, regions of high velocity in this mode lie above the roughness crests in the z-direction and permeate the entire boundary layer. This is consistent with observations of high-momentum zones in streamwise-aligned roughnesses by Vandervel and Ganapathisubramani [71] and others. The mode $\hat{u}^+(y; k_r, m_r, 0)$ is the smallest measured stationary velocity mode, as it can be created only by non-linear interactions involving the other stationary modes. It attains a maximum amplitude of 0.09 at the lower limit of the measurement volume and changes only slightly in phase with y.

The relative uncertainty in the amplitude of the R2M mode $\hat{u}^+(y; k_r, 0, 0)$ has a maximum of 28% of the local amplitude at the lower limit of the measurement volume, and the relative uncertainty is below 10% for all $y/\delta > 0.073$. The uncertainty is mostly due to errors in the y-positioning of the hot-wire probe. The other measurable spatial Fourier modes $\hat{u}^+(y; 0, m_r, 0)$ and $\hat{u}^+(y, k_r, m_r)$ have relative uncertainties of 91% and 83%, respectively, at the lower limit of the measurement volume. The relative uncertainty of $\hat{u}^+(y; 0, m_r, 0)$ is below 25% for all $y/\delta > 0.048$, while uncertainty in $\hat{u}^+(y, k_r, m_r)$ persists throughout the boundary layer.

3.4 Spatially-averaged velocity power spectra

Due to the highly time-resolved instantaneous velocity data available at each measurement point, the spatial distribution of streamwise stress $\overline{u'u'}(x, y, z)$ can be decomposed into contributions from each individual frequency measured in the flow. We consider first the spatial average over the roughness unit of the power spectrum $\Phi(y, x, z, \omega)$ of the streamwise fluctuating velocity, $u'(x, y, z, t)$.

Figures 3.7a-3.7c plot the spatially-averaged, pre-multiplied power spectra $\langle \omega\Phi(y, \omega) \rangle$ for the smooth wall, R1M, and R2M cases, respectively. The plotted spectra were obtained by first computing Welch's power spectral density estimate for the velocity time series in MATLAB. The power spectra were pre-multiplied and then transformed into a log-frequency basis by interpolation. A moving average fil-

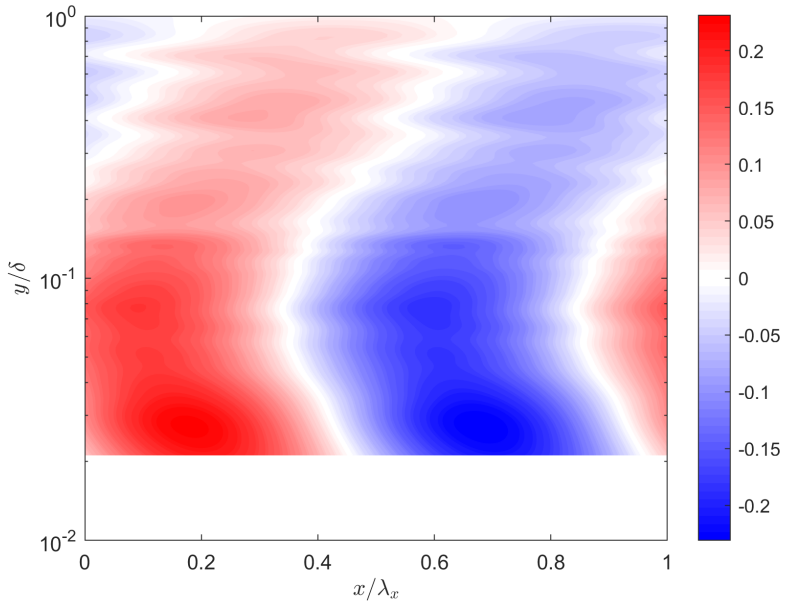
10^0
10^{-1}
10^{-2}
y/δ
0
0.2
0.4
0.6
0.8
1
x/λ_x
0.2
0.15
0.1
0.05
0
-0.05
-0.1
-0.15
-0.2

(a)

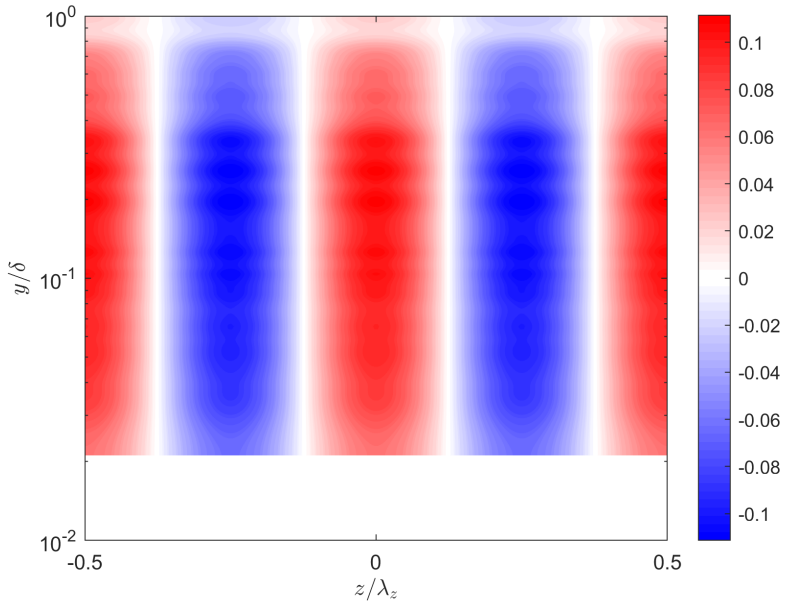
10^0
10^{-1}
10^{-2}
y/δ
-0.5
0
0.5
z/λ_z
0.1
0.08
0.06
0.04
0.02
0
-0.02
-0.04
-0.06
-0.08
-0.1

(b)

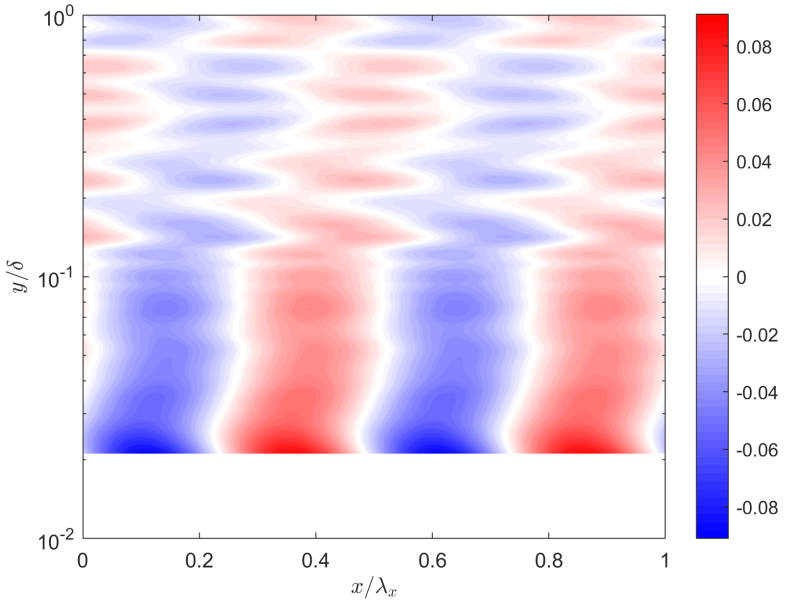

(c)

Figure 3.6: Spatial representations for the R2M case of (a) the mean velocity spatial Fourier mode $\hat{u}^+(y;k_x,0,0)$, (b) the mean velocity spatial Fourier mode $\hat{u}^+(y,0,k_z,0)$, and (c) the mean velocity spatial Fourier mode $\hat{u}^+(y,k_x,k_z,0)$. Red contours indicate a region in which the flow is faster than at other points at the same y-location.

ter was applied to the power spectra with a width equal to one tenth of a decade in wavenumber in order to smooth the data and simplify the comparison between cases. Consistent with the results for velocity variance, the R1M case is very similar to the smooth-wall case while the R2M boundary layer contains less energy than the smooth case at all values of (y,ω). Consistent with the observations of Chan et al. for sinusoidal roughness in pipe flow [11], the R2M roughness, with substantial secondary flow throughout the boundary layer, has a power spectrum that is shifted toward higher frequencies.

3.5 Signature of the roughness geometry in the velocity power spectra

Just as with mean velocities earlier in the chapter, the same spatial variation, i.e. the spatial dependence that is correlated to the roughness geometry and thus stationary in space, can be examined for the power spectrum of the stress by decomposition into spatial Fourier modes. We examine the contributions to this spatial dependence by wavenumber of the time-dependent signal by examining the spectral content of the variation, i.e. $\widehat{\omega\Phi}^+(y,\omega;k,m)$. These plots contain some noise as a result of ap-

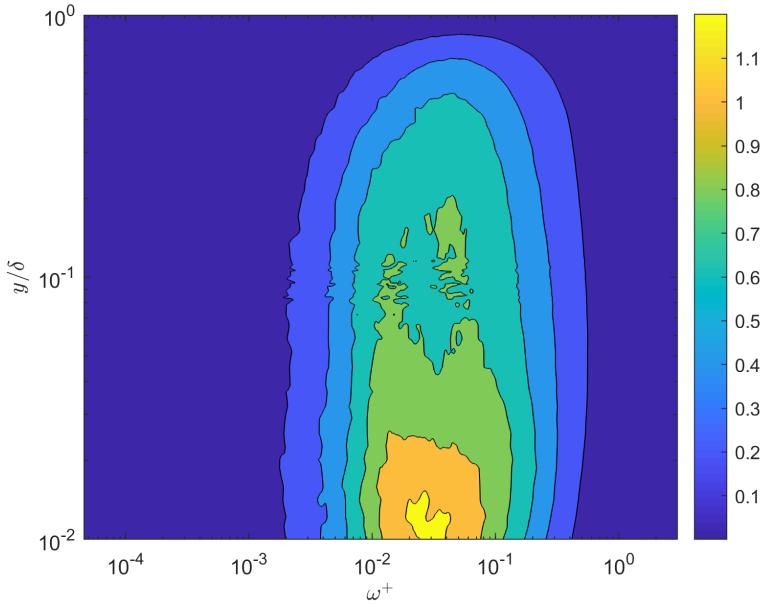
10^0
10^{-1}
10^{-2}
y/δ
10^{-4}
10^{-3}
10^{-2}
10^{-1}
10^0
ω^+
1.1
1
0.9
0.8
0.7
0.6
0.5
0.4
0.3
0.2
0.1

(a)

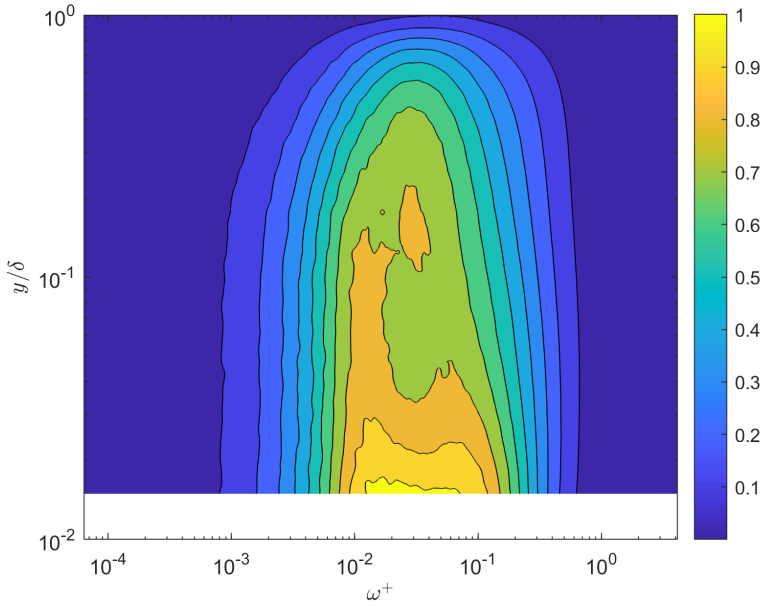
10^0
10^{-1}
10^{-2}
y/δ
10^{-4}
10^{-3}
10^{-2}
10^{-1}
10^0
ω^+
1
0.9
0.8
0.7
0.6
0.5
0.4
0.3
0.2
0.1

(b)

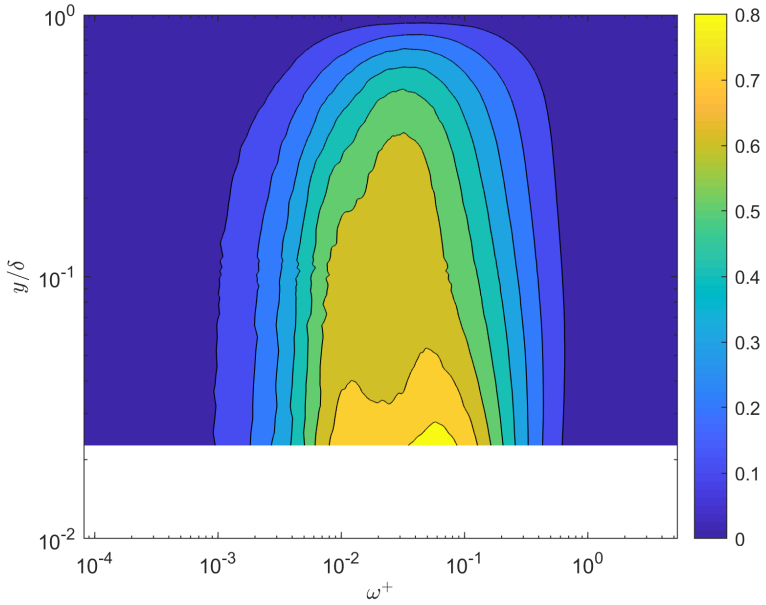

(c)

Figure 3.7: Comparison of spatially-averaged premultiplied angular frequency power spectra $\langle \omega \Phi(y, \omega) \rangle$ for (a) the smooth-wall case, (b) the R1M case and (c) the R2M case .

plying Welch's method to experimental data. As with the spatially-averaged spectra, these plots were smoothed with a moving average filter with a width equal to one tenth of a decade in frequency. A larger filter width would result in additional smoothing, at the cost of reducing frequency precision. It must be stressed that the stationary velocity Fourier modes shown earlier do not contribute to the power spectra. The only velocity Fourier modes which contribute to the measured power spectrum are modes with non-zero frequency which convect past the hotwire. The finite frequency associated with these modes ensures that they have no linear interaction with the zero-frequency static roughness. With reference to the triadic interactions shown in Figure 2.1(a), note that contributions to the spatio-temporal average stress can only arise from interactions with $(k_2, m_2, \omega_2) = -(k_1, m_1, \omega_1)$. A temporally stationary but spatially varying stress at $(k_1 + k_2, m_1 + m_2, 0)$ can be obtained from pairs of velocity Fourier modes with wavenumbers $\boldsymbol{K_1}, \boldsymbol{K_2}$ such that $(k_1, m_1, \omega_1) = (k_2, m_2, -\omega_1)$; this is the subject of this section.

The quantity $|\omega \widehat{\Phi}^+(y, \omega; k, m)|$ is identically zero for a smooth wall with non-zero (k, m), and is the result of convecting velocity Fourier modes which cannot be directly affected by the roughness through linear mechanisms (due to the difference

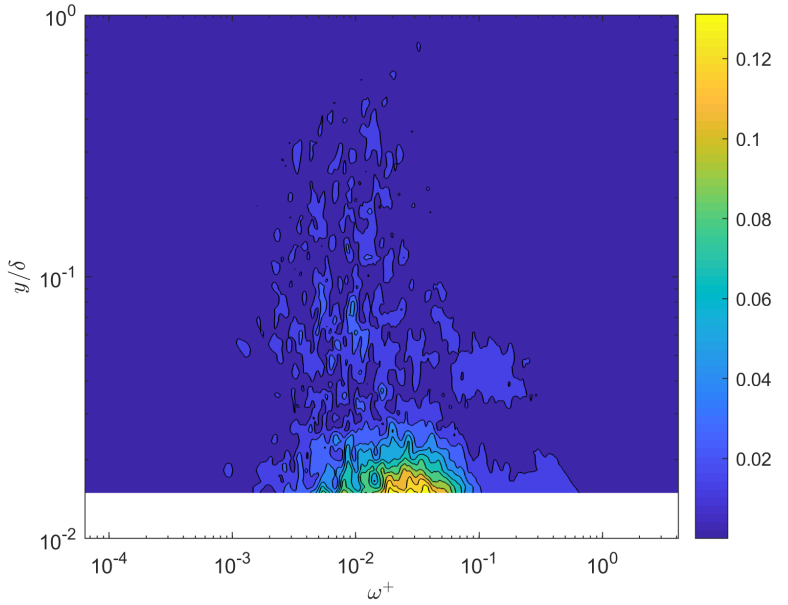

(a)

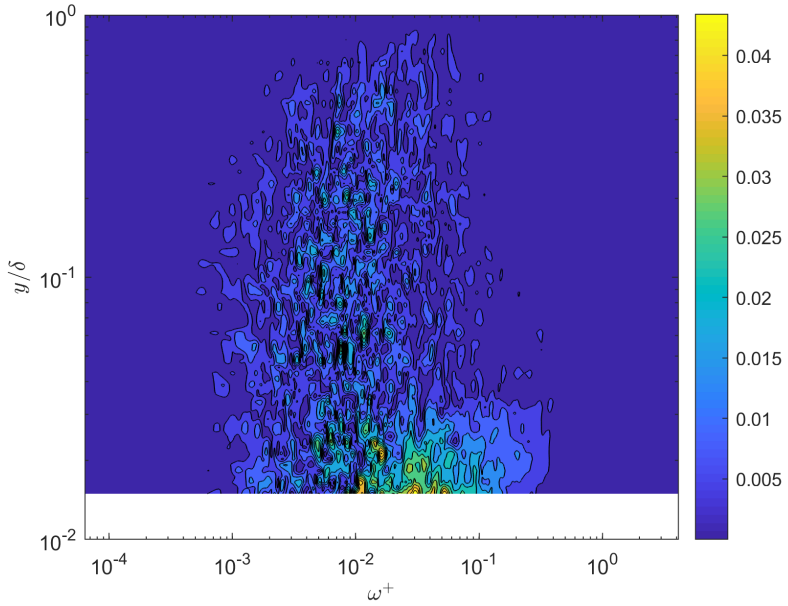

(b)

in ω). It is a measurement of the extent to which the kinetic energy present at a particular scale in the flow is modulated in space by interaction with the roughness-correlated stationary modes, so we will name it the "scale modulation" of the flow at a particular set of wavenumbers.

As with the stationary velocity Fourier modes of the R1M case, the magnitude of the

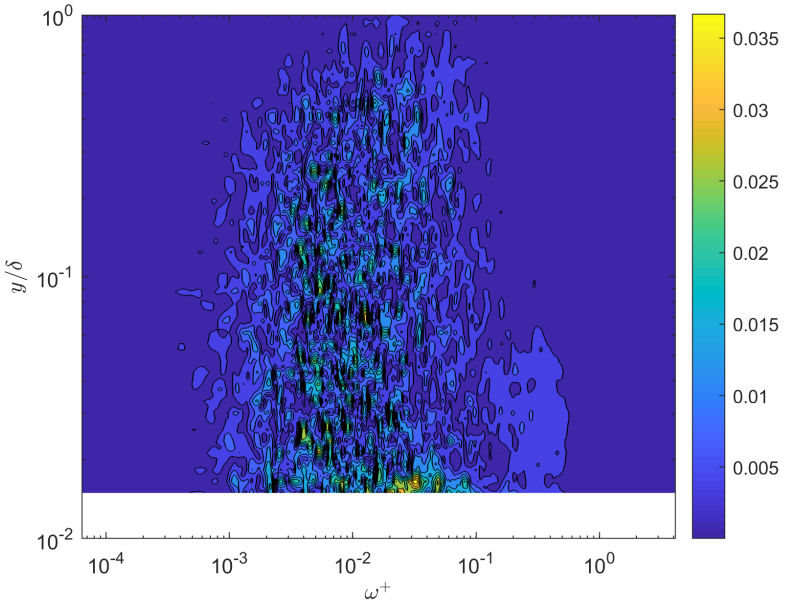

(c)

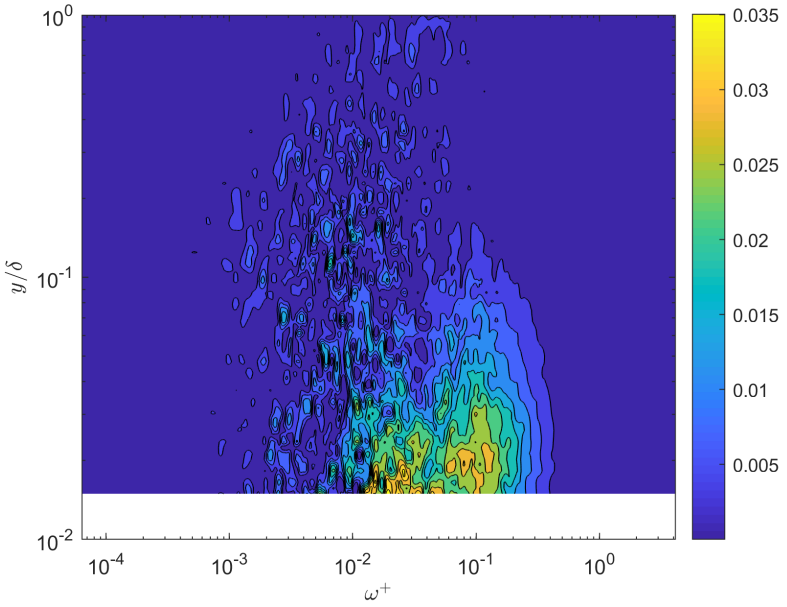

(d)

Figure 3.8: Magnitude of the R1M scale modulation $|\omega\widehat{\Phi}^+(y,\omega;k,m)|$ for (k,m) = (a)(k_r, m_r) (b)$(2k_r, 2m_r)$ (c)$(2k_r, 0)$,(d)$(0, 2m_r)$.

spatial variation in power spectra is most pronounced for $(k, m) = (k_r, m_r)$, as shown in Figure 3.8a. Notably, the scale modulation at this wavenumber is concentrated in a relatively small region in (ω, y) space, around $\omega^+ = 0.02$ and lying against the lower boundary of the measurement volume. That the scale modulation is much more concentrated than the average power spectrum from Figure 3.7b implies that certain scales are preferentially modulated by the stationary velocity Fourier modes. The modulation is also focused at low y, like the corresponding velocity Fourier mode. The scale modulation for $(k, m) = (0, 2m_r)$, from Figure 3.8d is similarly concentrated, but at a higher wavenumber around $\omega^+ = 0.1$. The scale modulation also reaches into fairly large y-values, like the velocity Fourier mode for $(k, m) = (0, 2m_r)$. The other wavenumbers show very little scale modulation at all. This implies that the strength of the scale modulation, as well as the region of preferential modulation, are strong functions of roughness wavenumber.

For the R2M case, the streamwise-varying-only mode with $(k, m) = (k_r, 0)$ displays the strongest scale modulation, as shown in Figure 3.9a. There are two lobes of high scale modulation, centered at $\omega = 0.01, 0.08$. The scale modulation for $(k, m) = (0, m_r)$, from Figure 3.9b, also shows two lobes, but separated in y as well. Here, the scale modulation extends almost to the boundary layer edge, like the corresponding velocity Fourier mode $(k, m) = (0, m_r)$ in Figure 3.6b. The remaining wavenumber $(k, m) = (k_r, m_r)$ shows little scale modulation.

3.6 Discussion

The rough-wall turbulent boundary layers examined here differs from a canonical smooth-wall boundary layer due to the imposition of a perturbation of the wall boundary condition by a small-amplitude, idealized roughness. This roughness geometry can be described in terms of the streamwise and spanwise wavelengths imposed on the flow through a small number of Fourier modes which match the roughness wavenumber and have zero frequency. Associated with the periodic roughness unit is change to the spatio-temporal mean, and a stationary variation in the mean velocity field, i.e. a time-independent spatial variation, which does not exist in the canonical smooth-wall flow. Because the latter variation is correlated with the roughness geometry, it can be interpreted as a linear response to the input boundary condition. The spatial variation in the power spectrum is also correlated to the roughness, but this cannot be a linear effect: the power spectrum is a measure of the energy of convecting modes, which cannot be linearly related to the roughness. There must be some non-linear process modulating these convecting modes to pro-

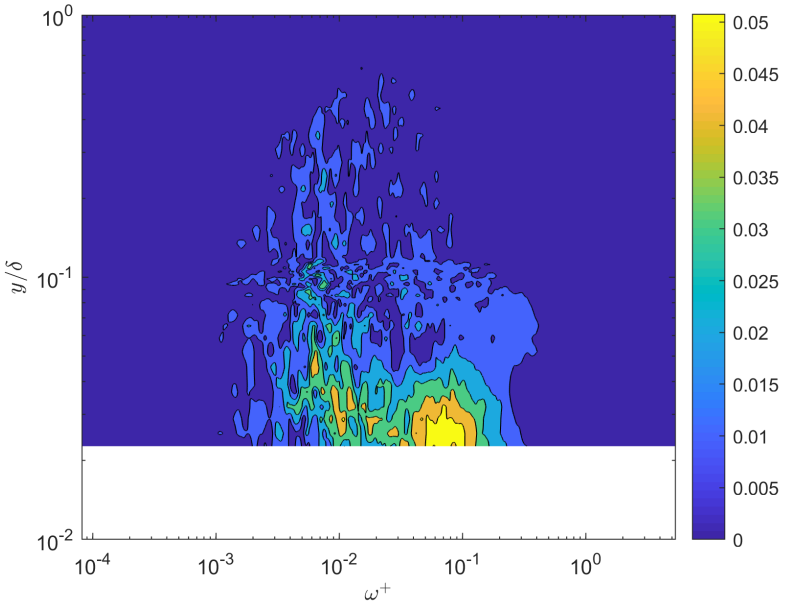
10^0
10^{-1}
10^{-2}
y/δ
10^{-4}
10^{-3}
10^{-2}
10^{-1}
10^0
ω^+
0.05
0.045
0.04
0.035
0.03
0.025
0.02
0.015
0.01
0.005
0

(a)

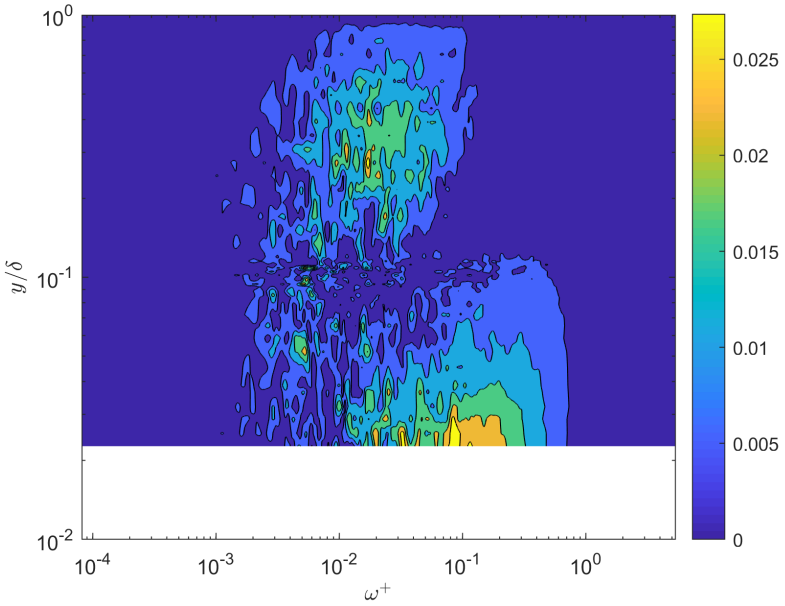
10^0
10^{-1}
10^{-2}
y/δ
10^{-4}
10^{-3}
10^{-2}
10^{-1}
10^0
ω^+
0.025
0.02
0.015
0.01
0.005
0

(b)

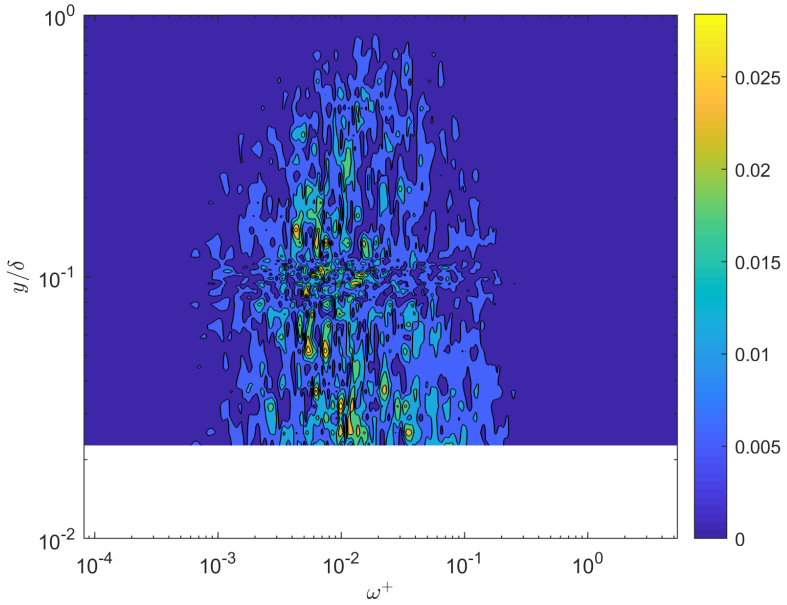

(c)

Figure 3.9: Magnitude of the R2M scale modulation $|\omega\widehat{\Phi}^+(y,\omega;k,m)|$ for $(k,m) =$ (a)$(k_r,0)$ (b)$(0,m_r)$ (c)(k_r,m_r).

duce the scale modulation recorded in this chapter. The general correspondence between the wall-normal extent of the stationary velocity Fourier modes and that of the scale modulation suggests that these stationary velocity modes are responsible, through the triadic interactions described in Chapter 2.

The next two chapters will create a model for the results shown here. Chapter 4 will model the stationary velocity Fourier modes as resolvent response modes, to obtain full-domain profiles in all three velocity components. Chapter 5 will model the nonlinear interactions themselves at low order to predict observed scale modulation.

Chapter 4

MODELING AND SCALING OF STATIC VELOCITY FOURIER MODES

The chapter evaluates the suitability of most-amplified resolvent modes for the purpose of modeling the spatial variation in mean velocity induced by a periodic roughness. With a link established between the static resolvent modes and the observed spatial Fourier modes of mean velocity, the scaling of these modes with respect to roughness wavenumber and Reynolds number is explored. While the scaling of traveling-wave resolvent modes with Reynolds number has been characterized by Moarref et al. [46], modeling efforts here require static resolvent modes with $\omega = 0$, whose scaling have not been studied.

4.1 Resolvent Modes as Models for Velocity Fourier Modes in Wall-Bounded Turbulence

Most-amplified resolvent modes, as measured by the associated singular value, have been successfully used to model convecting velocity Fourier modes associated with particular wavenumber-frequency vectors. Applications have included opposition control [39], energy density scaling [46], and response to time-periodic perturbations [17]. In this chapter, resolvent modes will be used to model non-linear (triadic) interactions within periodic rough-wall turbulent boundary layers. This will require, at minimum, a single stationary resolvent mode with non-zero wavenumber and zero frequency to model the stationary velocity mode induced by the roughness, as well as two convecting resolvent modes with non-zero frequency which are triadically compatible with the stationary mode.

Resolvent modes are an obvious model for the stationary velocity Fourier modes introduced by a periodic roughness. We may consider the addition of a periodic roughness as a perturbation to the flow with zero time frequency and identical wavenumber to the periodic roughness. One therefore expects the resulting stationary velocity Fourier mode to resemble the most-amplified resolvent mode with the same spatial wavenumbers and zero frequency. Comparison of observed stationary streamwise velocity Fourier modes, described in Chapter 3, to computed most-amplified resolvent modes does not contradict that hypothesis.

A complete quantitative comparison of the observed velocity Fourier modes to the most amplified resolvent modes presents a number of difficulties given the available experimental data. For one, the resolvent modes describe all three components of velocity, while the experiments give only streamwise data. The resolvent modes extend to the wall, while the experimental data exists only for finite y, often not capturing the predicted peak of the resolvent modes. The orthonormal nature of resolvent modes allows for a simple and robust projection of velocity fields onto that basis, with calculated mode weights that are independent of the rank of the chosen basis. However, without wall-normal velocity data and without spanwise velocity data to calculate observed wall-normal vorticity, even a partial phase vector in velocity-vorticity space cannot be constructed from the experimental data without making assumptions about the other velocity components.

Ordinary least squares (OLS) provides a straightforward way of fitting the calculated streamwise velocity profile of the resolvent modes to the observed stationary Fourier modes of streamwise velocity in a way that minimizes the sum of the squared errors at different points. As a downside to this approach, the weights obtained for each mode depend on the number and the selection of modes which are used to fit. This is a result of the lack of orthogonality among just the u-fields of the resolvent modes. To judge the suitability of single resolvent modes as a model of observed stationary velocity Fourier modes, both methods are used to create best fits and to calculate weights for each of the most-amplified resolvent modes for each wavenumber. If the best fits recreate the salient features of the observed modes, and if the weights indicate that the most-amplified mode is dominant in the fit, then the most-amplified mode can be judged to be a good model.

To project the observed velocity Fourier mode onto the basis of resolvent response modes, we exploit the orthogonality defined in Equation 2.38. The v- and w- components of the field are set to be zero, as is the u-component outside the measurement volume. The field is then converted to velocity-vorticity phase space using the definition of η in Equation 2.23 and projected onto the response mode basis ϕ using the Q-weighted inner product to produce the weight vector γ, as shown in Equation 4.1.

$$\gamma = \psi^* Q \begin{bmatrix} 0 & 1 & 0 \\ im & 0 & -ik \end{bmatrix} \begin{bmatrix} \hat{u}^+ \\ \hat{v}^+ = 0 \\ \hat{w}^+ = 0 \end{bmatrix}. \tag{4.1}$$

This weighting vector γ can then be used to create a best-fit mode by left-multiplying the basis ψ.

The least squares regression is performed using MATLAB's built in "mldivide" function. As the result depends on the selection of basis vectors, regressions are performed using the most amplified resolvent response mode, the 3 most-amplified modes, and the 5 most-amplified modes with non-zero u-components to check for robustness. Modes with zero-valued u-velocity fields are discarded. For the R1M case with (k,m)=(k_r, 0) and the R2M case with (k,m)=(k_r, 0), the modes with the second, third, fifth, seventh, and ninth highest singular values were discarded for that reason. All other cases considered here had no discarded modes. Both the basis vectors and the observed $\hat{u}^+$ field are sampled at 800 evenly-spaced points throughout the measurement volume before performing the regression.

In both methods, the basis of resolvent response modes ϕ is calculated from the resolvent as described in Section 2.2 with $N = 800$, with zero frequency and an appropriate wavenumber. The velocity profile used as a input to the resolvent is taken to be the observed spatio-temporally averaged velocity field for the appropriate roughness geometry, with linear interpolation to zero velocity at zero y below the measurement volume.

The results of both fitting processes for all the observable wavenumbers are plotted in Figures 4.1-4.7. Although all plots show only absolute values, phase information for the observed modes and for the basis was used for all fits.

Figure 4.1a shows the amplitude of the observed stationary velocity Fourier mode $\hat{u}^+(y; k_r, m_r, 0)$ for the R1M roughness. This mode presents clear challenges for fitting: the peak in observed amplitude lies on the lower boundary of the measurement volume, and the actual peak clearly lies below that. The orthonormal projection is ill-suited to fitting this mode; equal weight is given to maintaining v- and w- fields which are identically zero as is given to matching the u-field. As a result, the fitted u-amplitude is well below the observed peak, and the projected resolvent mode weights plotted in Figure 4.1b are roughly consistent in amplitude rather than declining with increasing mode number. The least-squares fit, on the other hand, captures the shape of the observed mode near the lower bound of the measurement volume. As the number of modes considered increases, the most-amplified mode remains the mode with the greatest weight, as shown in Figure 4.1. This degree of agreement is a promising sign that the most-amplified resolvent mode may be a good model for the $\hat{u}^+(y; k_r, m_r, 0)$ stationary velocity Fourier mode for the R1M

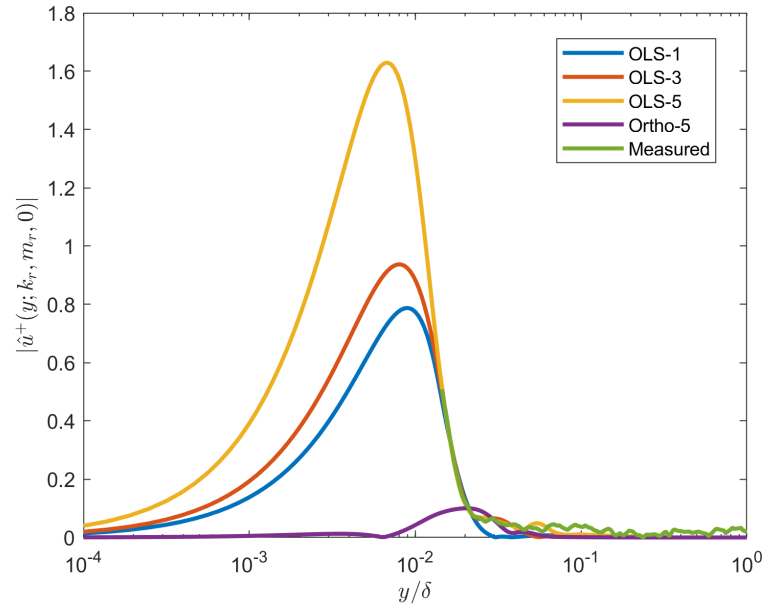

(a)

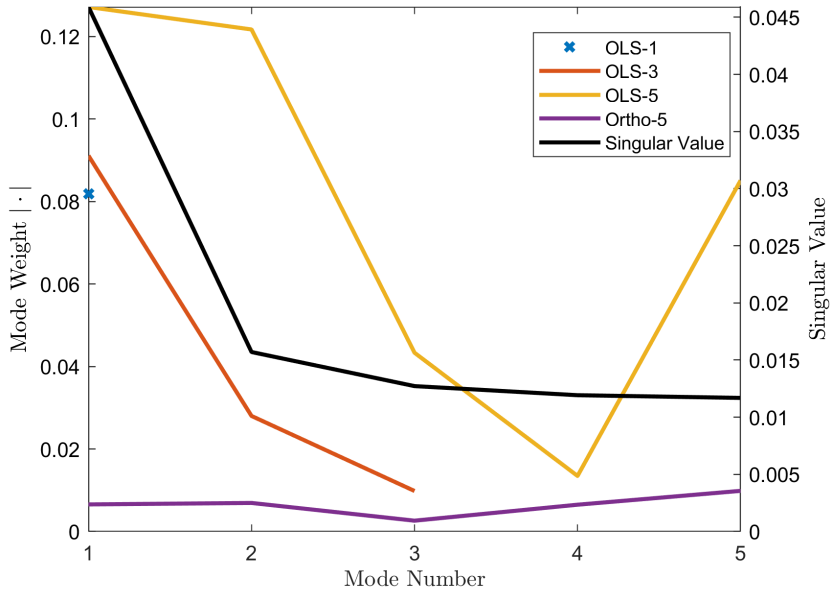

(b)

Figure 4.1: R1M roughness, $(k,m) = (k_r,m_r)$ a) Amplitude of measured stationary velocity Fourier mode $\hat{u}$ (green), least-squares fit of the measured velocity to the most-amplified 1 (blue), 3 (red), or 5 (yellow) resolvent response modes. b)Amplitude of weighting vector entries, same colors as above, plotted on the left y-axis, as well as the singular values for the corresponding resolvent modes, plotted on the right y-axis.

roughness, but there is insufficient evidence to be conclusive. This result is consistent with the singular values for the resolvent modes; the most-amplified mode has a singular value three times higher than the following one, meaning that the response of this resolvent operator when forced in an unorganized manner is expected to be dominated by the first mode.

Best fit profiles and weights are plotted for the observed stationary velocity Fourier mode $\hat{u}^+(y; 2k_r, 2m_r, 0)$ of the R1M roughness in Figure 4.2. As for the previous mode, the measurement volume does not contain the actual peak in mode amplitude, but the least squares fit captures the shape well. The most-amplified mode has the greatest weight when considering 5 resolvent modes, but not when considering just 3, and all least-squares fits capture the negative slope of the observed mode at the bottom of the measurement volume. The orthonormal projection again fails to properly capture the shape of the mode. Due to the nearly equal weighting of the first and second resolvent modes, this mode is not a good candidate for low-rank representation by resolvent modes.

Figure 4.3 plots the best fit profiles and weights for the R1M roughness for the stationary velocity Fourier mode $\hat{u}^+(y; 2k_r, 0, 0)$. The least-squares regression seems to converge quickly as more modes are considered, with the most-amplified mode dominating the fit. The orthonormal projection is identically zero, as the u-only, streamwise-varying-only velocity field used for the projection is non-solenoidal and therefore projects onto zero for the purely divergence-free basis ψ. The strong weighting of the most-amplified mode from the least-squares regression implies that it is a plausible model for the stationary velocity Fourier mode. This low-rank behavior again concurs with the behavior of the singular values, which are dominated by the highly-amplified first mode.

Figure 4.4a shows the amplitude of the observed stationary velocity Fourier mode $\hat{u}^+(y; 0, 2m_r, 0)$ for the R1M roughness. As the number of modes considered increases, the calculated mode weights do not change, as shown in Figure 4.1. These mode weights also agree with the orthonormal projection, because, in the case of a mode which varies only in the spanwise direction, all wall-normal vorticity is associated with streamwise velocity. The most dominant resolvent response mode is the second-most amplified, indicating that this may be a better model for this observed stationary velocity Fourier mode than the most-amplified mode. This is consistent with the behavior of the singular values, which do not feature a sharp decline after the first mode, and therefore predict significant contributions from multiple resol-

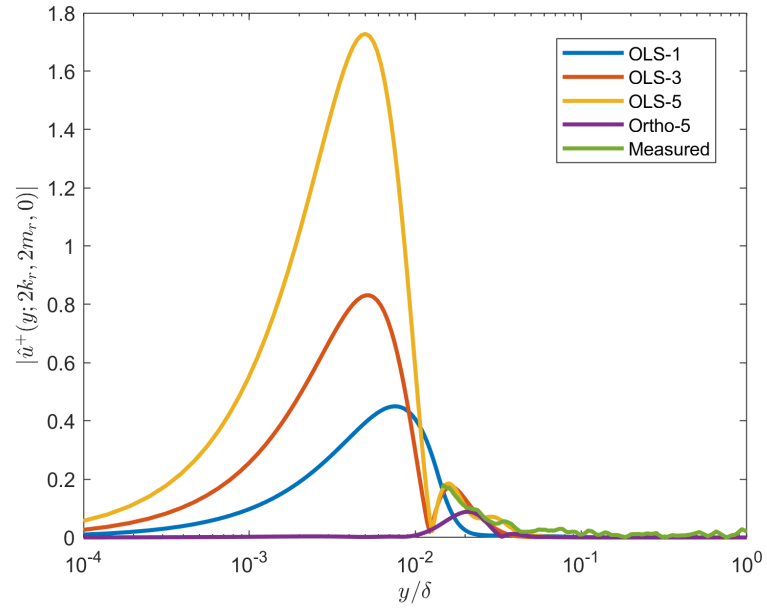

(a)

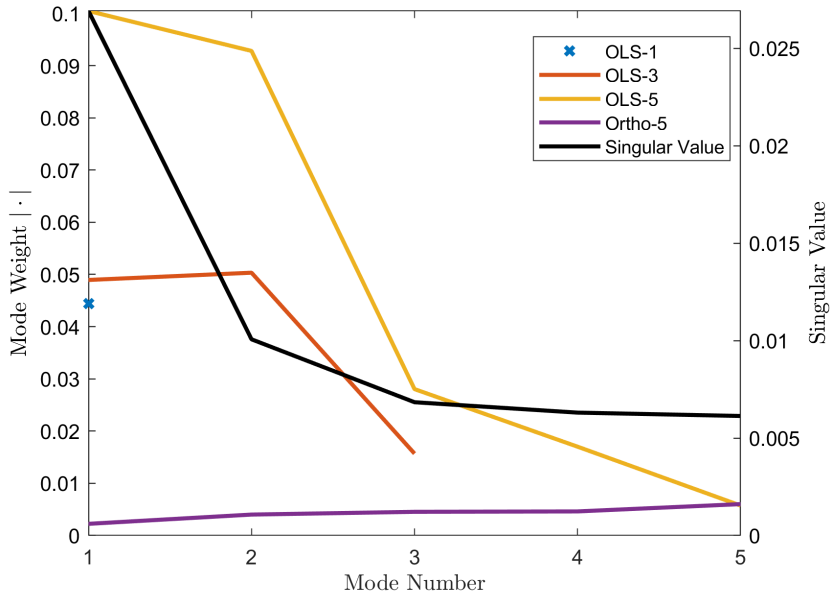

(b)

Figure 4.2: R1M roughness, $(k,m) = (2k_r, 2m_r)$ a) Amplitude of measured stationary velocity Fourier mode $\hat{u}$ (green), least-squares fit of the measured velocity to the most-amplified 1 (blue), 3 (red), or 5 (yellow) resolvent response modes. b)Amplitude of weighting vector entries, same colors as above, plotted on the left y-axis, as well as the singular values for the corresponding resolvent modes, plotted on the right y-axis.

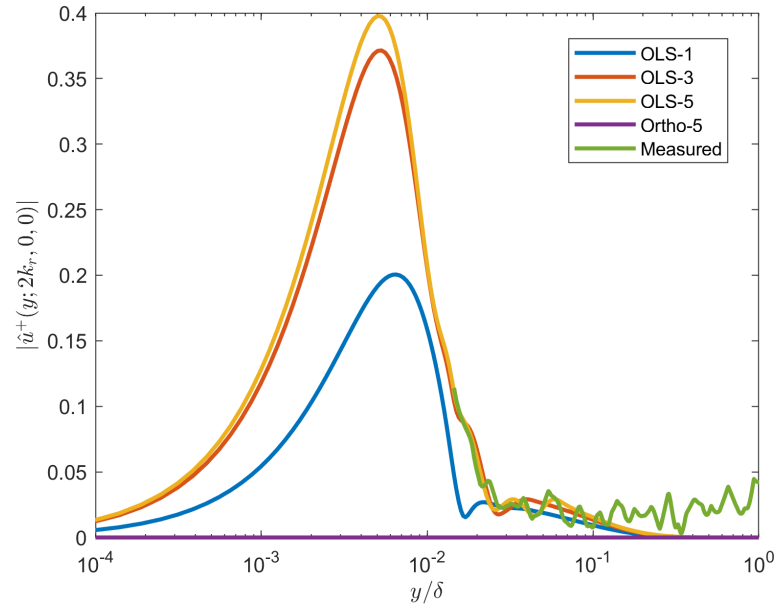

(a)

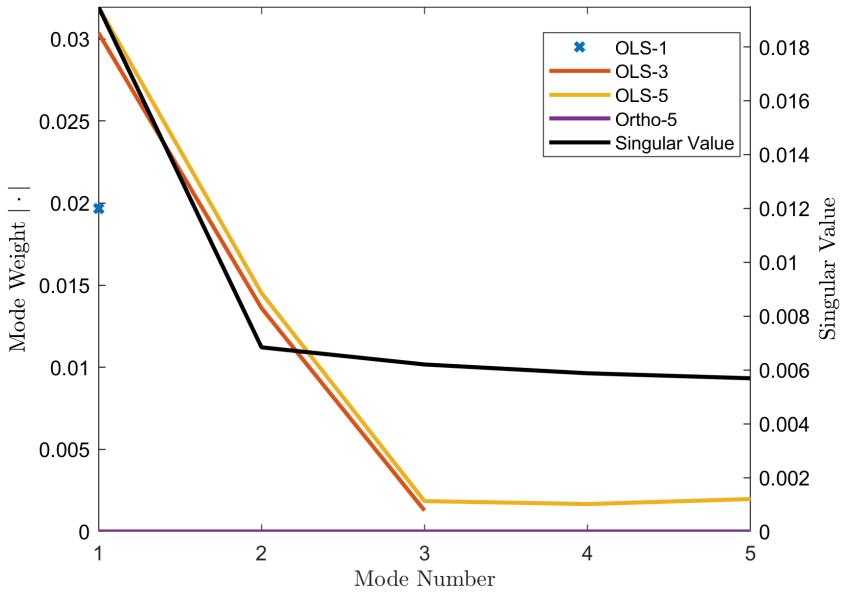

(b)

Figure 4.3: R1M roughness, $(k,m) = (2k_r,0)$ a) Amplitude of measured stationary velocity Fourier mode $\hat{u}$ (green), least-squares fit of the measured velocity to the most-amplified 1 (blue), 3 (red), or 5 (yellow) resolvent response modes. b)Amplitude of weighting vector entries, same colors as above, plotted on the left y-axis, as well as the singular values for the corresponding resolvent modes, plotted on the right y-axis.

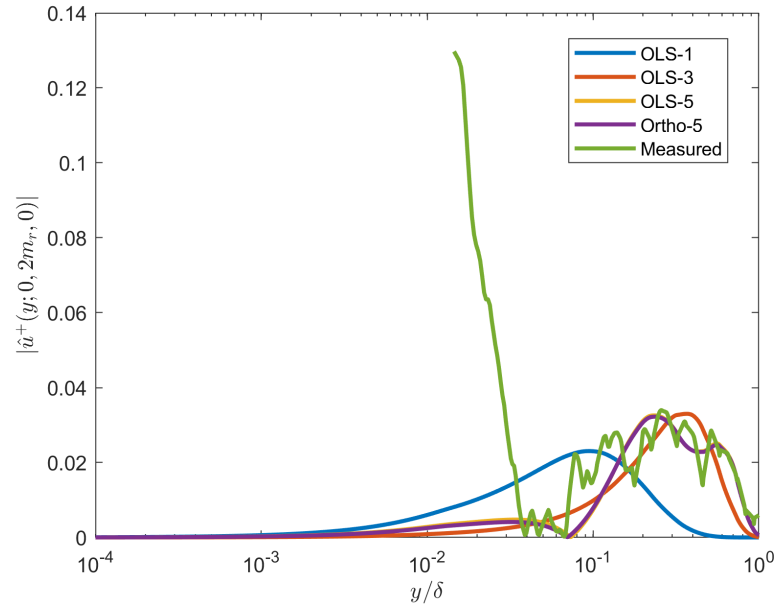

(a)

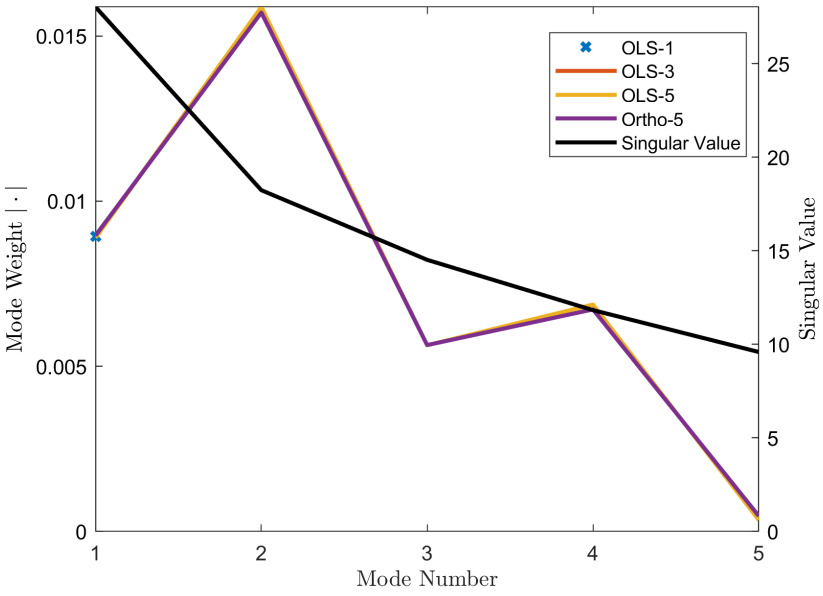

(b)

Figure 4.4: R2M roughness, $(k, m) = (0, 2m_r)$ a) Amplitude of measured stationary velocity Fourier mode $\hat{u}$ (green), least-squares fit of the measured velocity to the most-amplified 1 (blue), 3 (red), or 5 (yellow) resolvent response modes. b)Amplitude of weighting vector entries, same colors as above, plotted on the left y-axis, as well as the singular values for the corresponding resolvent modes, plotted on the right y-axis.

vent modes in response to a random forcing vector. The singular values are much higher than those of the other wavenumbers, but the predicted weights are lower. This points to a lack of correlation between the magnitude of the singular values, in an absolute sense, at a particular set of wavenumber and the magnitude of the spatial variation of the mean velocity at that wavenumber.

Turning now to the R2M roughness, the observed static velocity Fourier mode $\hat{u}^+(y; k_r, 0, 0)$ is reasonably represented by the most-amplified resolvent response mode, as shown in Figure 4.5. The least-squares regression converges quickly as the number of modes considered is increased, and the fitted modes match the tall, shallow-sloped shape of the observed velocity Fourier mode very well within the measurement volume. The orthonormally-projected mode weights are identically zero, for the reasons explained above for spanwise-constant modes. The singular values are consistent with this result, with a near-perfect match for the drop-off between the first and second modes.

The R2M spanwise-varying-only stationary velocity Fourier mode $\hat{u}^+(y; 0, m_r, 0)$ plotted in Figure 4.6 also shows that the mode is plausibly captured by a single resolvent response mode. All methods of computing the weighting vector produce the same weights, and the most-amplified resolvent mode dominates in all cases. The shape of the mode is well-captured, including a peak around $y/\delta = 0.2$. Like the spanwise-only mode from the R1M case, the singular values do not predict low-rank behavior, but the prediction in this case is incorrect. This is also another case of large singular values which do not translate to large mode weights, as calculated from observed behavior.

Best fit profiles and weights are plotted for the observed stationary velocity Fourier mode $\hat{u}^+(y; k_r, m_r, 0)$ of the R2M roughness in Figure 4.7. The weighting vector produced by orthonormal projection is low-amplitude and disagrees with the other methods for the reasons given above. The least-squares weighting vectors do not converge as the number of modes considered is increased, but the weighting for the most-amplified mode is consistently highest. The shape of the profile is well-captured by the OLS fit within the measurement volume, but increasing the number of modes in the fit drastically increases the modeled peak amplitude, possibly due to over-fitting noise in the profile. This mode may be a marginal case for representing the stationary velocity Fourier mode by a single resolvent response mode, despite a large drop in magnitude between the first and second singular values which might predict otherwise.

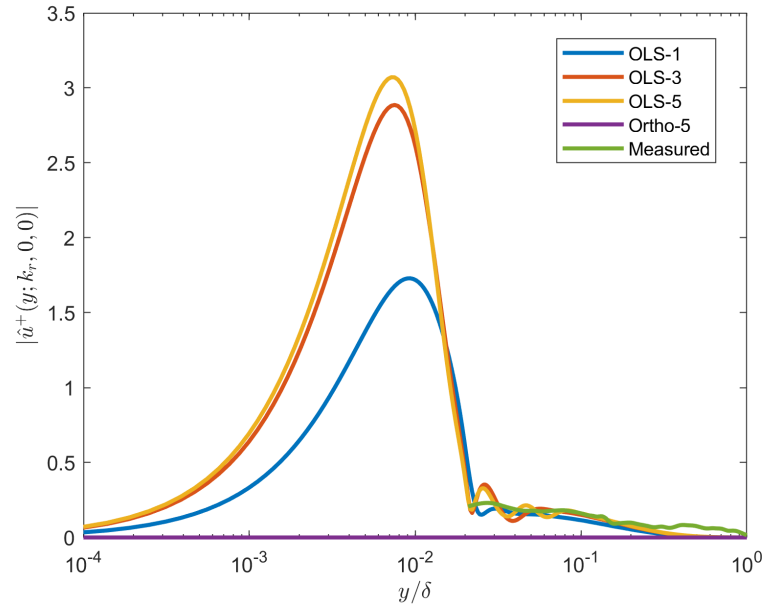

(a)

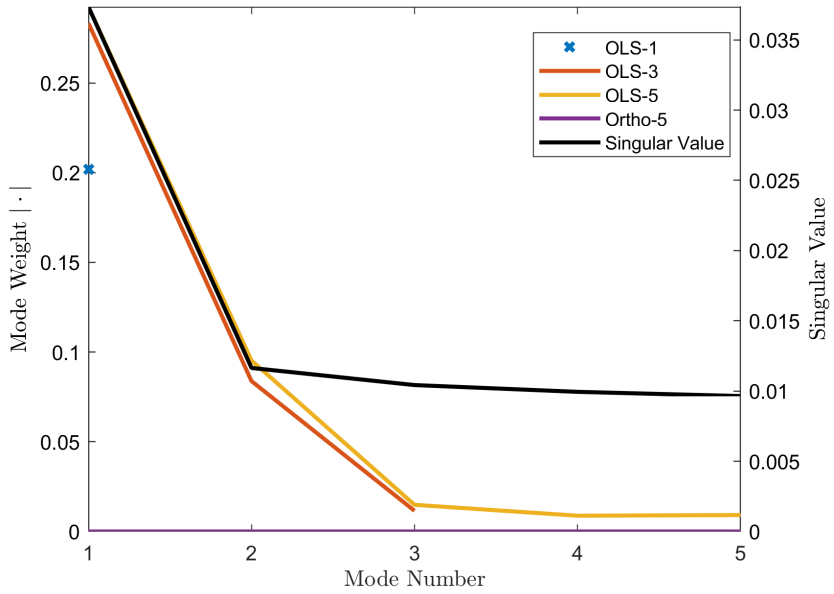

(b)

Figure 4.5: R2M roughness, $(k,m) = (k_r,0)$ a) Amplitude of measured stationary velocity Fourier mode $\hat{u}$ (green), least-squares fit of the measured velocity to the most-amplified 1 (blue), 3 (red), or 5 (yellow) resolvent response modes. b)Amplitude of weighting vector entries, same colors as above, plotted on the left y-axis, as well as the singular values for the corresponding resolvent modes, plotted on the right y-axis.

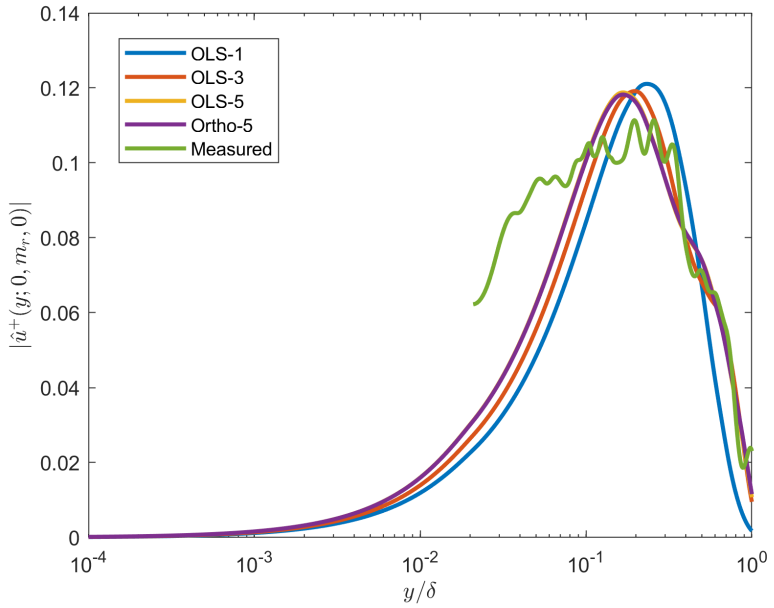

(a)

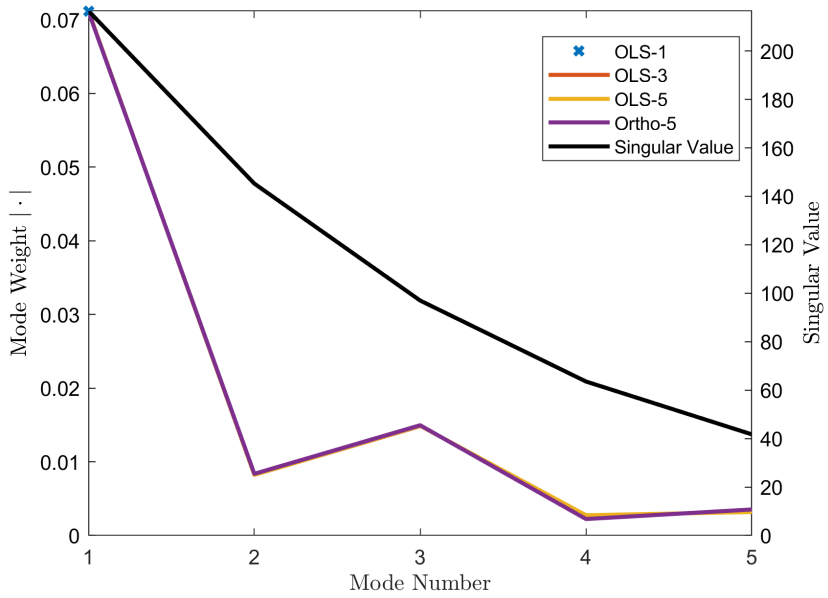

(b)

Figure 4.6: R2M roughness, $(k,m) = (0,m_r)$ a) Amplitude of measured stationary velocity Fourier mode $\hat{u}$ (green), least-squares fit of the measured velocity to the most-amplified 1 (blue), 3 (red), or 5 (yellow) resolvent response modes. b)Amplitude of weighting vector entries, same colors as above, plotted on the left y-axis, as well as the singular values for the corresponding resolvent modes, plotted on the right y-axis.

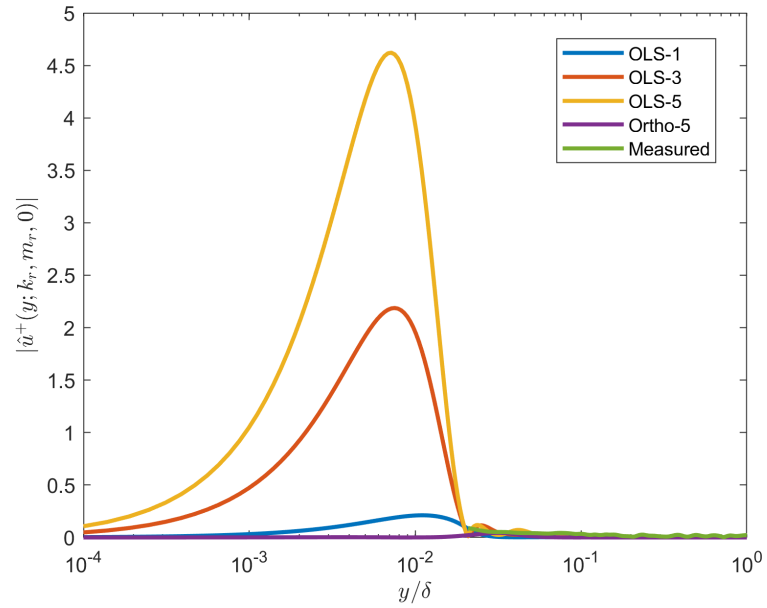

(a)

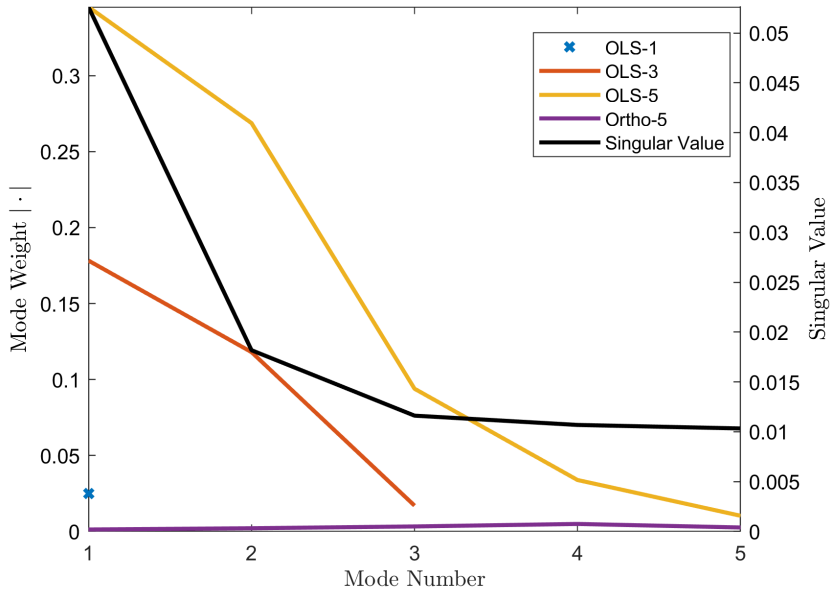

(b)

Figure 4.7: R2M roughness, $(k,m) = (k_r,m_r)$ a) Amplitude of measured stationary velocity Fourier mode $\hat{u}$ (green), least-squares fit of the measured velocity to the most-amplified 1 (blue), 3 (red), or 5 (yellow) resolvent response modes. b)Amplitude of weighting vector entries, same colors as above, plotted on the left y-axis, as well as the singular values for the corresponding resolvent modes, plotted on the right y-axis.

Given the limited experimental data available for comparison, resolvent modes are an acceptable model for the static velocity Fourier modes which are caused by a periodic roughness. The correspondence is greatest for the modes which are two-dimensional, with either k or m equal to zero. More data, including all components of time-averaged velocity and measurements down to the wall, might improve the quality of the fitting or eliminate the need for this modeling all together. Even if a resolvent mode is not a perfect match for experimental data, it is valuable as a physics-based profile in y which satisfies boundary conditions and incompressibility for the roughness wavenumber and which can be calculated cheaply for modeling nonlinear interactions.

4.2 Approximation and Scaling of Resolvent Modes

In order to derive the scaling of the boundary layer resolvent operator, the properties of the resolvent will first be related to the better-studied eigenvectors and eigenvalues of the Orr-Sommerfeld-Squire operator. In this section, we follow Trefethen et al. [70] and Symon et al. [67], starting with an eigenvector decomposition of the linear operator $M^{-1}L$ from Equation 2.30. Here, $V = [V_1, V_2, ...]$ is a matrix whose columns V_j are right eigenvectors and J is a diagonal matrix of unique eigenvalues λ_j. Each eigenvector-eigenvalue pair solves the eigenvalue problem $M^{-1}LV_j = i\lambda_j V_j$. The derivation still holds for an operator with duplicated eigenvalues (the matrix J would be slightly modified), but the assumption of unique eigenvalues is retained for simplicity.

$$M^{-1}L = VJV^{-1}. \tag{4.2}$$

Recalling the definition of the resolvent operator H as well as its singular value decomposition from Equations 2.31 and 2.41 gives the equality in Equation 4.3:

$$H = (-i\omega + M^{-1}L)^{-1} = \psi\Sigma\phi^* Q. \tag{4.3}$$

Exploiting the identity $I = VJV^{-1}$, applying the distributive property to scalar $-i\omega$, and right multiplying by the inverse of Q produces the following expression:

$$\psi\Sigma\phi^* = (-i\omega I + VJV^{-1})^{-1}M^{-1}Q^{-1} = V(-i\omega I + J)^{-1}V^{-1}M^{-1}Q^{-1}. \tag{4.4}$$

The inverse of the the right eigenvector matrix V^{-1} can be rewritten as the product of a diagonal matrix $K = (U^*V)^{-1} = diag(\kappa_1, \kappa_2, ...)$ and the Hermitian transpose of

the left eigenvector matrix $U = [U_1, U_2, ...]$ whose columns U_i are left eigenvectors solving the eigenvalue problem $U_j^* M^{-1} L = i\lambda_j U_j^*$.

$$V^{-1} = KU^* = (U^* V)^{-1} U^*. \tag{4.5}$$

Representing both the resolvent SVD and eigenvalue decomposition as summations in Equation 4.6 makes clear the similarity in structure. The representations are not equivalent due to the different constraints placed on the eigenvectors and singular vectors: singular vectors must be mutually orthogonal, while eigenvectors must solve the eigenvalue problem. By definition, eigenvectors will be singular vectors only when the matrix $M^{-1}L$ is normal.

$$H = \sum_{j=1} \sigma_j \psi_j \phi_j^* Q = \sum_{j=1} \frac{\kappa_j}{-i\omega + i\lambda_j} V_j U_j^*. \tag{4.6}$$

In the case where the frequency ω approaches an eigenvalue λ_j, the eigenvalue representation will dominated by a single term of the summation. The singular value will then also be dominated by the most singular mode, so that an equality exists in the limit, as expressed in Equation 4.7.

$$\lim_{\omega \to \lambda_j} H = \sigma_1 \psi_1 \phi_1^* Q = (-i\omega + i\lambda_j)^{-1} \kappa_j V_j U_j^*. \tag{4.7}$$

It is clear from the structure of the left- and right-hand sides that ψ_1 and ϕ_1 approach the expressions given in Equations 4.8 and 4.9. Multiplying both sides of Equation 4.7 on the left by $\psi_1^* Q$ and on the right by ϕ_1 gives the expressions for the leading singular value σ_1 in Equation 4.10.

$$\lim_{\omega \to \lambda_j} \psi_1 \propto V_j. \tag{4.8}$$

$$\lim_{\omega \to \lambda_j} \phi_1^* \propto U_j^* Q^{-1}. \tag{4.9}$$

$$\lim_{\omega \to \lambda_j} \sigma_1 = \frac{\sqrt{V_j^* Q V_j}}{U_j^* Q^{-1} U_j (-i\omega + i\lambda_j)} = \frac{1}{\phi_1^* Q \psi_1^* (-i\omega + i\lambda_j)}. \tag{4.10}$$

Following Symon et al. [67], the singular value σ_1 can therefore be expressed as a product of resonance contribution $\frac{1}{-i\omega+i\lambda_j}$ and a non-normality contribution $\frac{1}{\phi_1^* Q \psi_1^*}$. The relation between σ_1 and ω_j is useful, as ω_j must satisfy the eigenvalue problem, allowing for the use of the OSS equation in physics-based scaling arguments for σ_1. While the expression in Equation 4.10 is only exact in the limit, it predicts trends in σ_1 for modes with $\omega = 0$ very well when λ_j is taken to be the closest eigenvalue to the origin. While previous work has investigated the scaling of eigenvectors of the linear Navier-Stokes operator, or of self-similar convecting resolvent modes [46], no work has yet used the relations shown by Symon et al. [67] to develop polynomial scalings for low-order representations of zero-frequency resolvent operators.

4.3 Scaling

Reynolds number-wavenumber scaling

When there is a near-constant amount of non-normality as measured by the criterion $\frac{1}{\phi_1^* Q \psi_1^*}$ identified by Symon et al., one would expect a good match between σ_1 and λ^{-1} for the $\omega = 0, m = 0$ resolvent over a range of wavenumbers and Reynolds numbers. Scaling plots here are limited to Blasius profiles, which make a useful model as analytical profiles exist for all Reynolds numbers, but scaling analyses here do not rely on the particulars of a profile so long as it has a finite skin friction at the wall and is monotonic. The scalings are therefore expected to apply to a turbulent mean profile as well. As shown in Figure 4.8, there is only a small, fairly constant amount of non-normality throughout this parameter space.

Figure 4.9 shows a comparison between σ_1 and λ^{-1} for a Blasius profile. Consistent with the plot of $\frac{1}{\phi_1^* Q \psi_1^*}$, there is very little variation between σ_1 and λ^{-1} throughout the parameter space. The divergence between the two is slightly larger than predicted, but is consistent in pattern. The quantities related to the singular value decomposition are calculated as described in Chapter 1, with N = 400. Eigenvectors and eigenvalues are calculated from the linearized Navier-Stokes operator defined in Equation 2.26, using MATLAB's built-in "eig" command. The figures show that there is good agreement between the singular values and the resonance. Scaling plots here are limited to Blasius profiles as exact profiles exist for all Reynolds numbers, but scaling analyses here do not rely on the particulars of a profile so long as it has a finite skin friction at the wall and is monotonic.

Figure 4.10 plots the quantity y_m/δ, where y_m satisfies Equation 4.11 for the leading resolvent response mode of the resolvent operator at a particular set of wavenum-

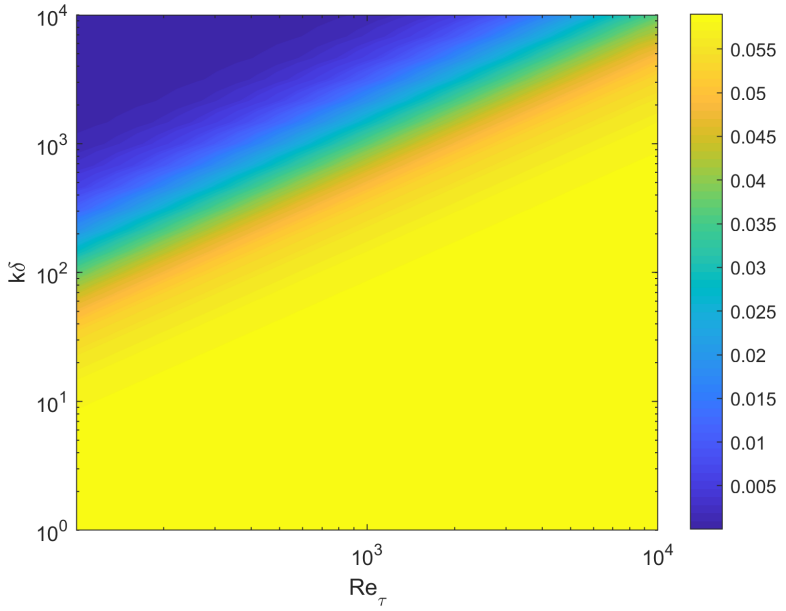

Figure 4.8: Contribution to σ_1 of non-normality $\log(\frac{1}{\phi_1^* Q \psi_1^*})$ for a Blasius boundary layer with $m = 0, \omega = 0$.

bers.

$$|\hat{u}(y_m)|^2 + |\hat{v}(y_m)|^2 + |\hat{w}(y_m)|^2 = \max_y |\hat{u}(y)|^2 + |\hat{v}(y)|^2 + |\hat{w}(y)|^2 \tag{4.11}$$

As the wall-normal location at which the leading response mode attains maximal kinetic energy, y_m is an important parameter for estimating the effect of a periodic roughness on the flow. This is the point at which there is expected to be the greatest spatial variation in mean velocity, and consequently the greatest potential for modulation of the convecting turbulent flow.

The asymptotic scaling of the leading resolvent response mode can be revealed by taking partial derivative of the logarithms of σ_1 and of y_m with respect to the logarithms of Reynolds number and wavenumber. Regions where these partial derivatives are constant are regions where a power-law relationship exists for σ_1, with the exponents being the values of the partial derivatives. These partial derivatives are plotted in Figures 4.11 and 4.12, revealing two regions of note.

Region 1

Figure 4.11 shows a region 1 where the leading singular value scales as $\sigma_1 \propto Re_\tau k^{-2}$. Analysis of the eigenvectors associated with the closest eigenvalues to the

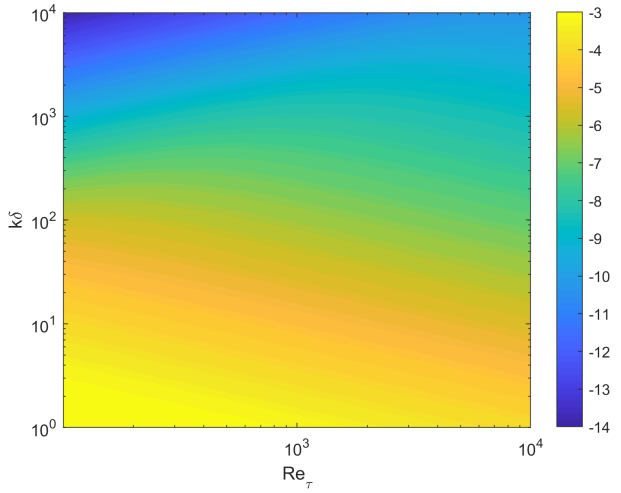

(a) $\log(\lambda^{-1})$

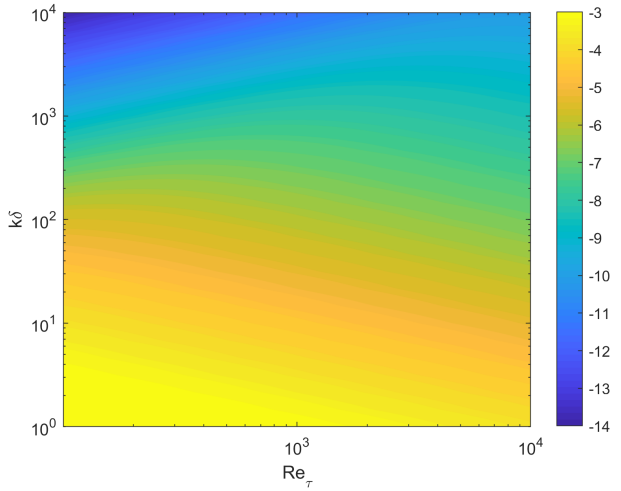

(b) $\log(\sigma_1)$

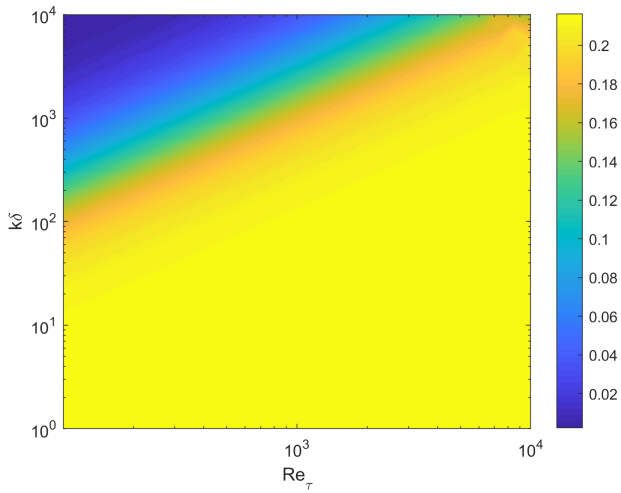

(c) $\log(\sigma_1)$

Figure 4.9: Resonance $\log(\lambda^{-1})$, leading singular value $\log(\sigma_1)$, and their difference $\log(\sigma_1) - \log(\lambda^{-1})$ for a Blasius boundary layer with $m = 0, \omega = 0$.

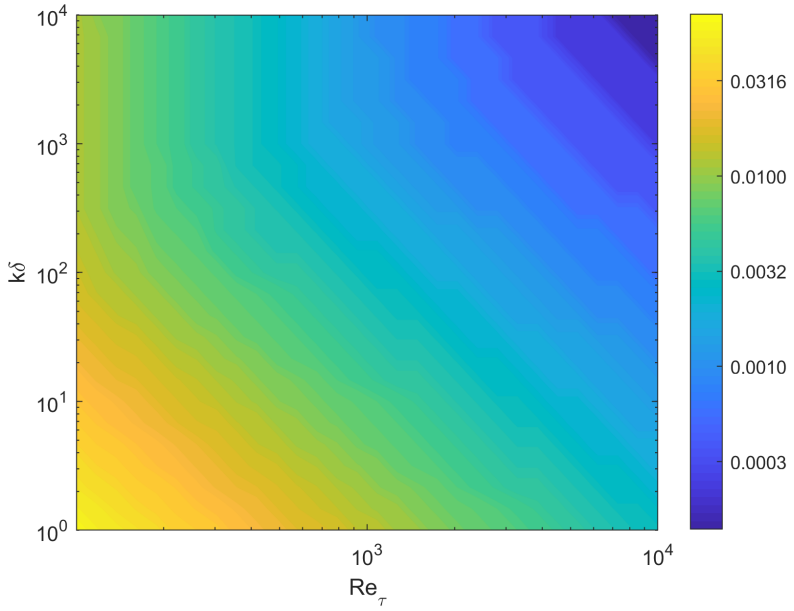

Figure 4.10: Wall-normal location at which the leading response mode attains maximum kinetic energy y_m/δ as a function of Reynolds number and wavenumber for a Blasius boundary layer with $m = 0, \omega = 0$.

origin for the Reynolds number-wavenumber combinations in region 1 reveal that the dominant balance lies between the first and third terms in the Squire equation below.

$$-i\lambda\eta + ik\langle\overline{u}\rangle\eta + \frac{b^2}{Re_\tau}\eta - \frac{1}{Re_\tau}\partial_y^2\eta + im\partial_y\langle\overline{u}\rangle\eta = 0. \tag{4.12}$$

Isolating these terms and applying the condition that $m = 0$ yields the following balance:

$$-i\lambda\eta + \frac{k^2}{Re_\tau}\eta = 0. \tag{4.13}$$

The linearity of both terms in η reveals an obvious scaling between λ, k, and Re_τ, and applying Equation 4.10 and assuming a constant non-normality contribution give a scaling for σ_1 as well, which matches well with the observed trends.

$$\lambda \propto \frac{k^2}{Re_\tau}. \tag{4.14}$$

$$\sigma_1 \propto Re_\tau k^{-2}. \tag{4.15}$$

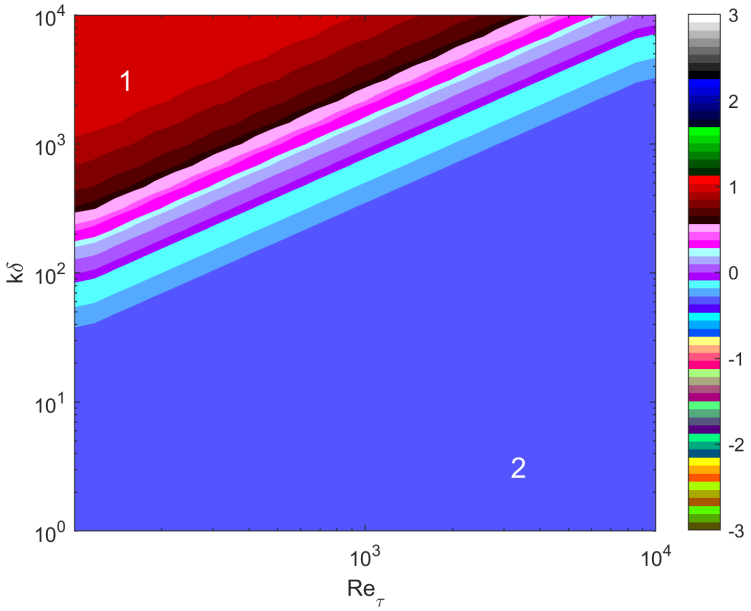

(a) $\frac{\partial \log(\sigma_1)}{\partial \log(Re_\tau)}$

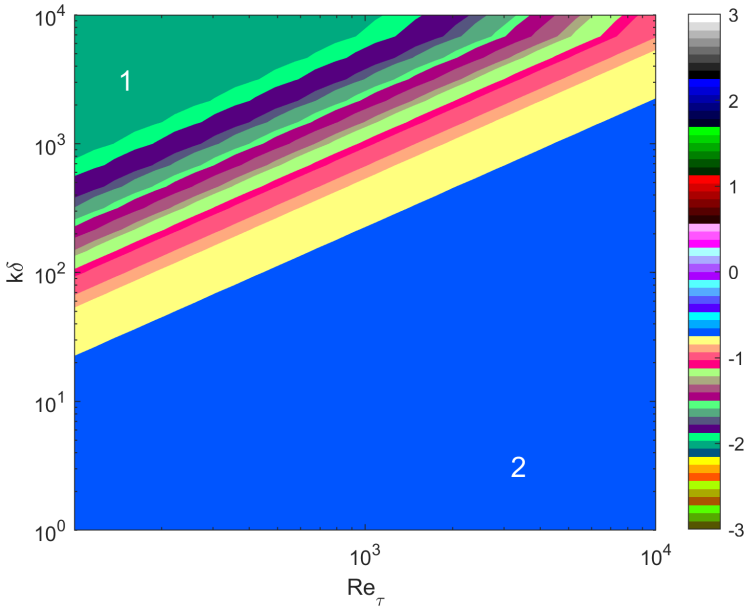

(b) $\frac{\partial \log(\sigma_1)}{\partial \log(k\delta)}$

Figure 4.11: Partial derivatives of the logarithm of σ_1 with respect to the logarithms of Reynolds number and wavenumber for a Blasius boundary layer with $m = 0, \omega = 0$. Constant-color areas represent areas with a single power law for σ_1 in terms of Re_τ and k.

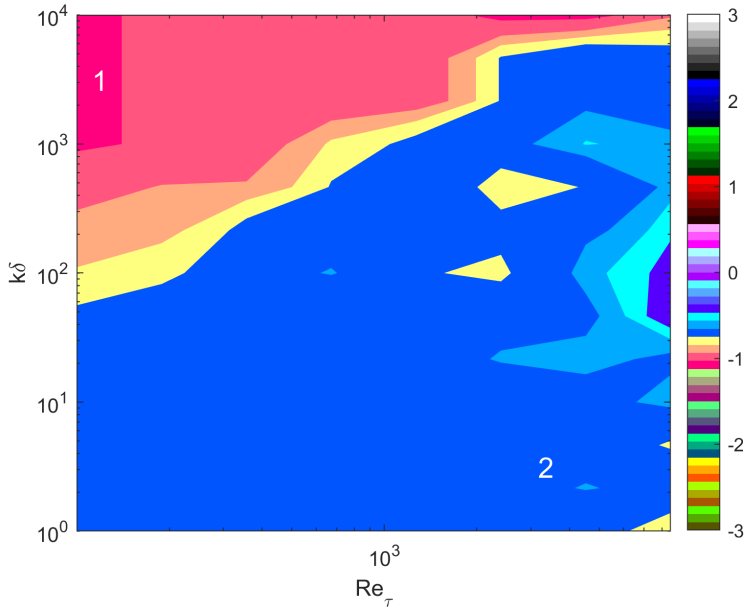

(a) $\frac{\partial \log(y_m/\delta)}{\partial \log(Re_\tau)}$

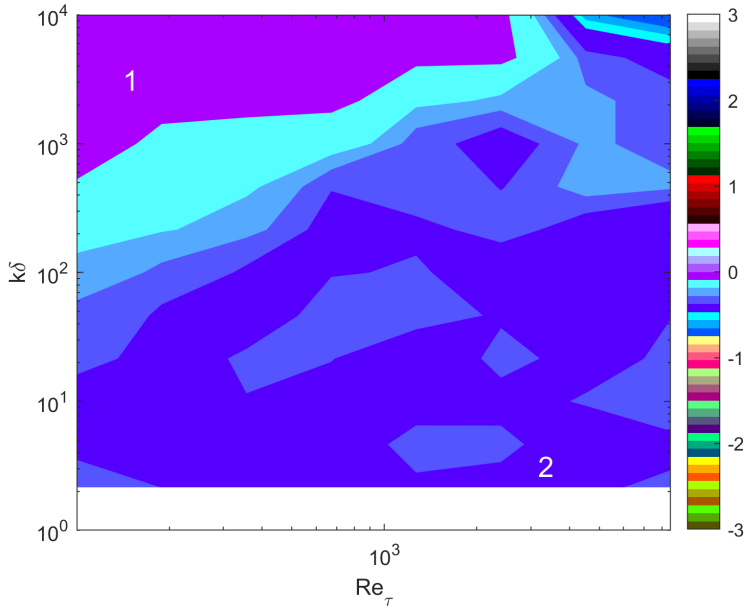

(b) $\frac{\partial \log(y_m/\delta)}{\partial \log(k\delta)}$

Figure 4.12: Partial derivatives of the logarithm of y_m/δ with respect to the logarithms of Reynolds number and wavenumber for a Blasius boundary layer with $m = 0, \omega = 0$. Constant-color areas represent areas with a single power law for y_m in terms of Re_τ and k.

Figure 4.12 shows and asymptotic scaling for y_m in Region 1 which is decidedly noisier than the σ_1 scaling, but which appears to be best characterized as in Equation 4.16. The dominant balance in this region, which gives an algebraic equation for η rather than a differential equation, cannot explain the profile of η in y.

$$y_m \propto Re_\tau^{-1} k^0. \tag{4.16}$$

Region 2

In region 2 of Figure 4.11, the leading singular value scales as $\sigma_1 \propto Re_\tau^{-1/3} k^{-2/3}$. Analysis of the eigenvectors associated with the closest eigenvalues to the origin for the Reynolds number-wavenumber combinations in region 2 reveals a dominant balance between terms 1, 2, and 4 in the Squire equation, reproduced below.

$$-i\lambda\eta + ik\langle\overline{u}\rangle\eta + \frac{b^2}{Re_\tau}\eta - \frac{1}{Re_\tau}\partial_y^2\eta + im\partial_y\langle\overline{u}^+\rangle v = 0. \tag{4.17}$$

Isolating these terms and applying the condition that $m = 0$ yields the following balance:

$$-i\lambda\eta + ik\langle\overline{u}\rangle\eta - \frac{1}{Re_\tau}\partial_y^2\eta = 0. \tag{4.18}$$

In this low-k regime, modes lie close to the wall, so that the spatio-temporally averaged velocity profile $\langle\overline{u}\rangle$ can be approximated by a Taylor series at the wall.

$$-i\lambda\eta + iky\left.\frac{\mathrm{d}\langle\overline{u}^+\rangle}{\mathrm{d}(y/\delta)}\right|_{y=0}\eta - \frac{1}{Re_\tau}\partial_y^2\eta = 0. \tag{4.19}$$

Given that velocities are normalized by u_τ and length scales by δ, the velocity gradient at the wall can be rewritten as Re_τ.

$$-i\lambda\eta + ikyRe_\tau\eta - \frac{1}{Re_\tau}\partial_y^2\eta = 0. \tag{4.20}$$

The equation can then be transformed to an ordinary differential equation for ξ in terms of Y, using the transformation from Schmid and Henningson [63], defined in Equation 4.21 and 4.22. The result is given in Equation 4.23

$$Y = \left(iRe_\tau^2 k\right)^{1/3} \left(y - \frac{\lambda}{kRe_\tau}\right). \tag{4.21}$$

$$\xi(Y) = \eta(y). \tag{4.22}$$

$$Y\xi - \frac{\mathrm{d}^2\xi}{\mathrm{d}Y^2} = 0. \tag{4.23}$$

Boundary conditions require that $\xi(Y) = \eta(y)$ go to zero as y approaches zero. For Equation 4.23 to have a self-similar solution and obey this boundary condition, the value of Y corresponding to $y = 0$ must be constant, as expressed in Equation 4.24 and leading to the scalings for λ and σ_1 in Equations 4.25 and 4.26, matching the observed scaling trends in region 2

$$\left(iRe_\tau^2 k\right)^{1/3} \left(\frac{\lambda}{kRe_\tau}\right) = const. \tag{4.24}$$

$$\lambda \propto Re_\tau^{1/3} k^{2/3}. \tag{4.25}$$

$$\sigma_1 \propto Re_\tau^{-1/3} k^{-2/3}. \tag{4.26}$$

The similarity expressed in Equation 4.22 implies that y_m will occur at a fixed value of Y, Y_m, throughout Region 2, where the dominant balance in Equation 4.17 holds. Solving Equation 4.22 for y_m and substituting the proportional relationship found in Equation 4.25 yields the following expression for y_m:

$$y_m \propto Y_m k^{-1/3} Re_\tau^{-2/3}. \tag{4.27}$$

Although the apparent scaling for y_m in Region 2 from Figure 4.12 is noisy due to the discretization of y, it is consistent with the expression in Equation 4.27.

Wavenumber Scaling

A similar analysis can be performed to determine the scaling of resolvent modes with k and m at constant Re_τ. The non-normality within this parameter space is mapped in Figure 4.13. The region of very low k and very low m has been masked,

as the calculated resolvent operator there is poorly conditioned, so that calculated resolvent quantities suffer from significant numerical error. Unlike the previous parameter space with $m = 0$, there is a significant region of non-normality at moderate m and very low k. We expect this to complicate any scaling analysis for σ_1 in that region.

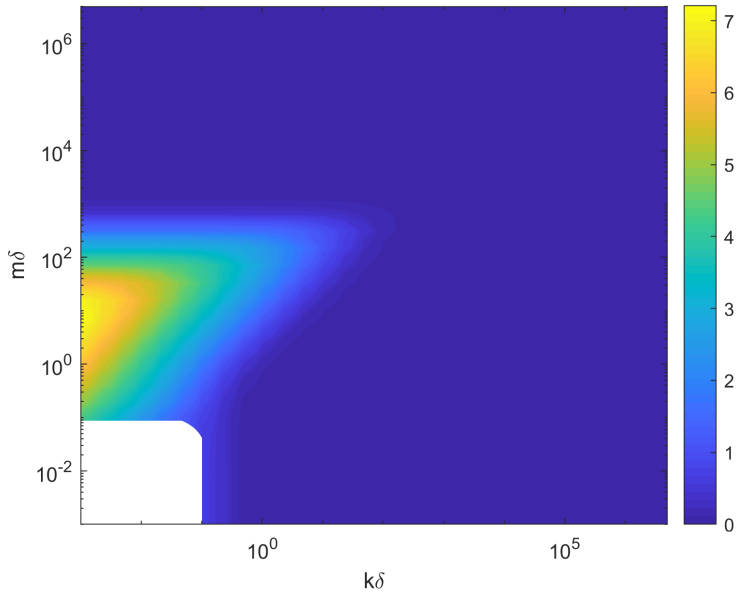

Figure 4.13: Contribution to σ_1 of non-normality $\log(\frac{1}{\phi_1^* Q \psi_1^*})$ for a Blasius boundary layer with $Re_\tau = 1000, \omega = 0$. The region where $k\delta < 0.1$ and $m\delta < 0.1$ has been masked due to the poorly-conditioned nature of the resolvent operator as all wavenumbers approach zero.

Figure 4.14 shows a comparison between resonance λ^{-1} and leading singular value σ_1 for a Blasius profile with $Re_\tau = 1000$ over a range of wavenumbers and $\omega = 0$, and show that there is good agreement between the singular values and the resonance outside the non-normal region identified above. The difference between the two, plotted in Figure 4.14c, matches the plot of non-normality in Figure 4.13 almost exactly.

Power law regions for σ_1 are identified in Figure 4.15 in the same way as in Figure 4.11, revealing four regions of note.

Additionally, we plot the wall-normal location at which the leading response mode attains maximal kinetic energy, y_m, defined in Equation 4.11, in Figure 4.16 and its gradients in Figure 4.17, marking the same regions as above.

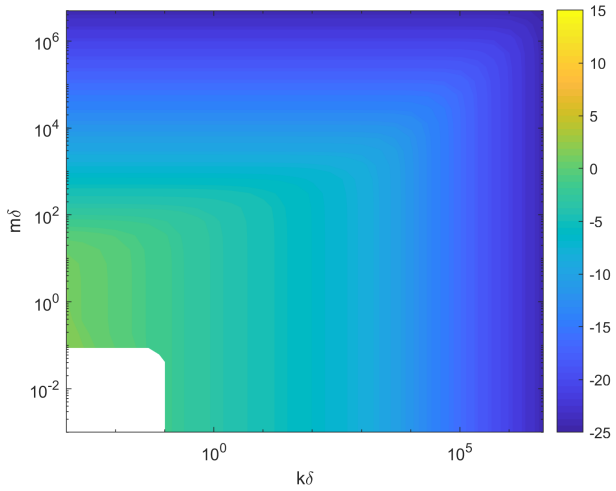

(a) $\log(\lambda^{-1})$

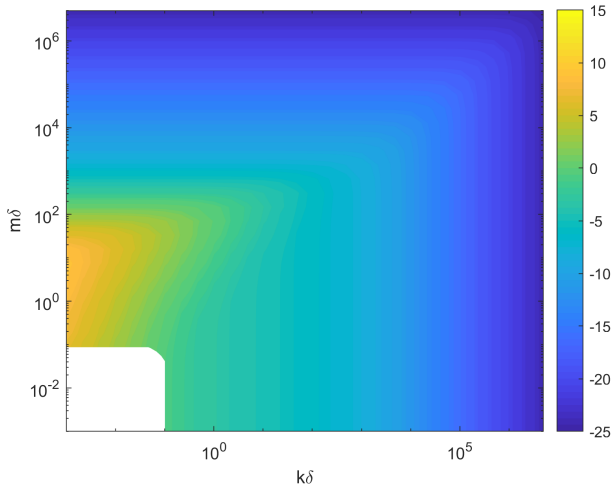

(b) $\log(\sigma_1)$

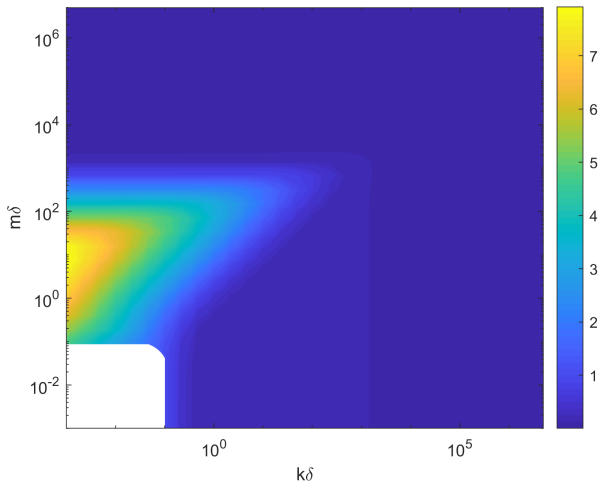

(c) $\log(\sigma_1)$

Figure 4.14: Resonance $\log(\lambda^{-1})$, leading singular value $\log(\sigma_1)$, and their difference $\log(\sigma_1) - \log(\lambda^{-1})$ for a Blasius boundary layer with $Re_\tau = 1000, \omega = 0$. The region where $k\delta < 0.1$ and $m\delta < 0.1$ has been masked due to the poorly-conditioned nature of the resolvent operator as all wavenumbers approach zero.

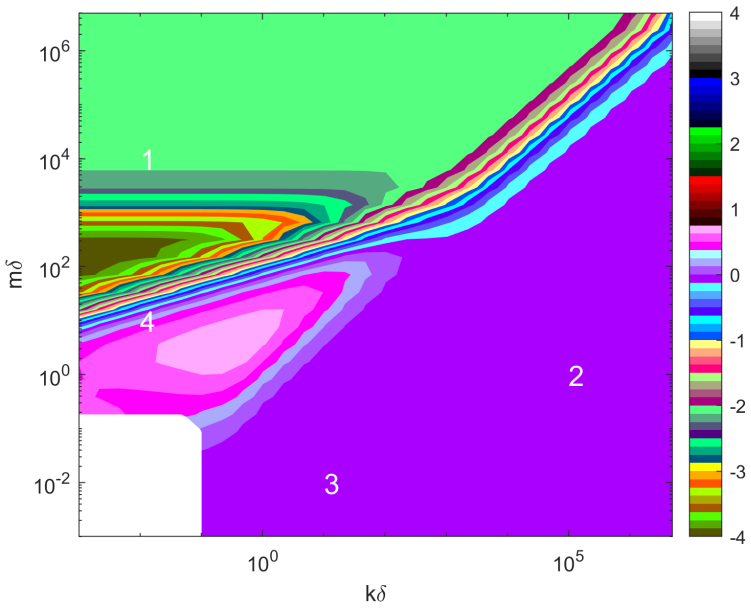

(a) $\frac{\partial \log(\sigma_1)}{\partial \log(k\delta)}$

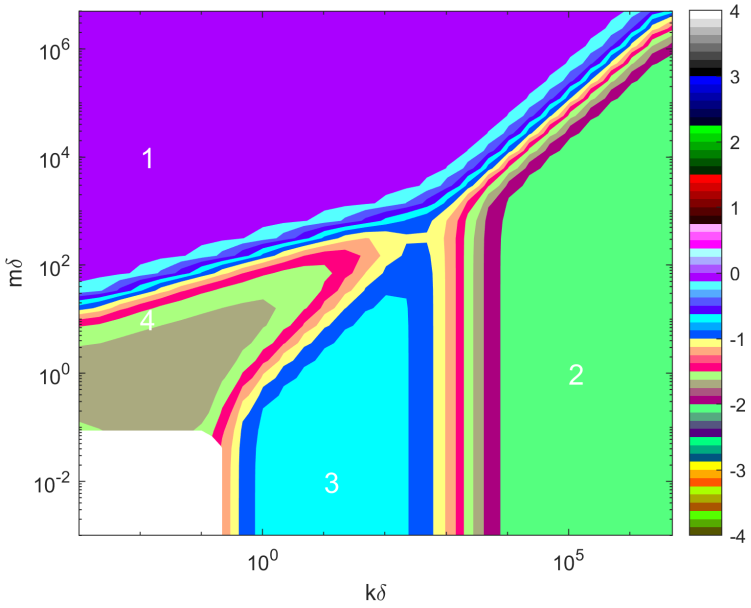

(b) $\frac{\partial \log(\sigma_1)}{\partial \log(m\delta)}$

Figure 4.15: Partial derivatives of the logarithm of σ_1 with respect to the logarithms of streamwise and spanwise wavenumber for a Blasius boundary layer with $Re_\tau = 1000, \omega = 0$. Constant-color areas represent areas with a single power law for σ_1 in terms of k and m. The region where $k\delta < 0.1$ and $m\delta < 0.1$ has been masked due to the poorly-conditioned nature of the resolvent operator as all wavenumbers approach zero.

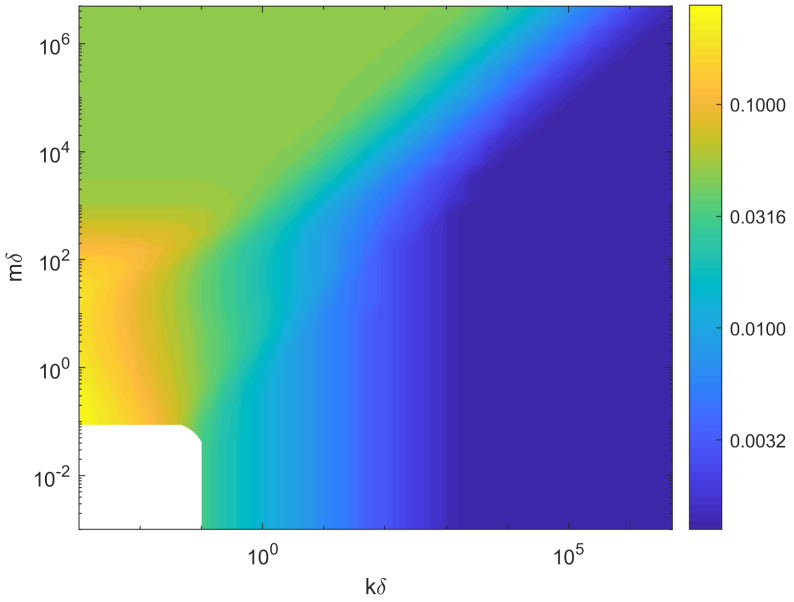

Figure 4.16: Wall-normal location at which the leading response mode attains maximum kinetic energy y_m as a function of streamwise and spanwise wavenumber for a Blasius boundary layer with $Re_\tau = 1000, \omega = 0$.

Regions 1 and 2

In regions 1 and 2 of Figures 4.15a and 4.15b, analysis of the eigenvectors associated with the closest eigenvalues to the origin for the wavenumber combinations in regions 1 and 2 reveal a dominant balance in the Squire equation given in Equation 4.28 below.

$$-i\lambda\eta + \frac{k^2 + m^2}{Re_\tau}\eta = 0 \tag{4.28}$$

As both terms are linear in η, the scaling is easily identified as in Equations 4.29 and 4.30.

$$\lambda \propto k^2 + m^2. \tag{4.29}$$

$$\sigma \propto (k^2 + m^2)^{-1}. \tag{4.30}$$

In region 1, $k << m$ and therefore the scaling becomes $\sigma_1 \propto m^{-2}$, while in region 2, $k >> m$ and $\sigma_1 \propto k^{-2}$.

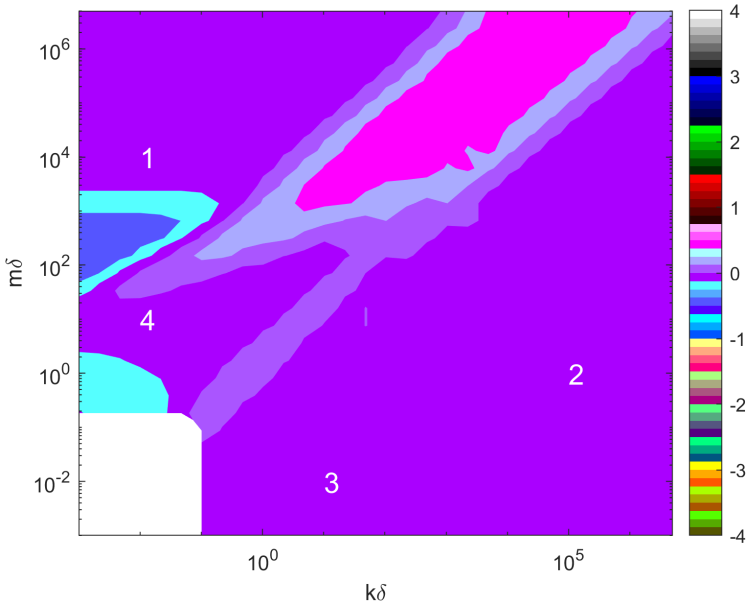

(a) $\frac{\partial \log(y_m/\delta)}{\partial \log(k\delta)}$

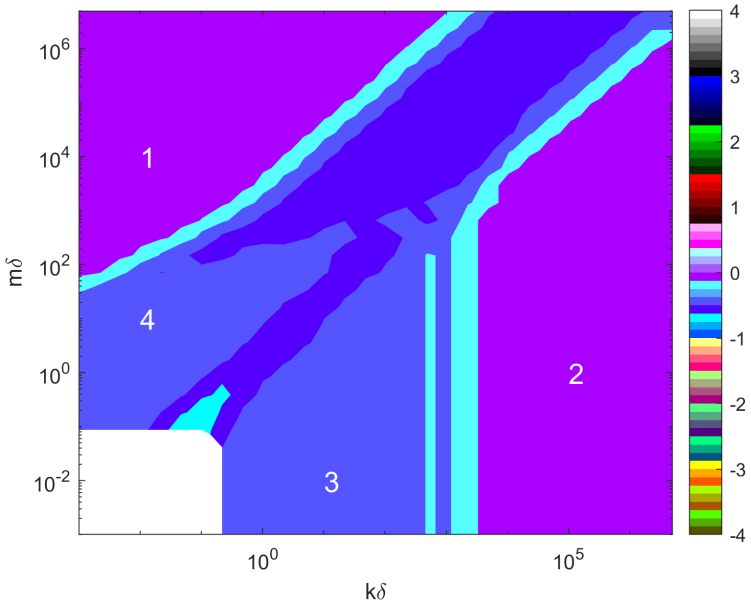

(b) $\frac{\partial \log(y_m/\delta)}{\partial \log(m\delta)}$

Figure 4.17: Partial derivatives of the logarithm of y_m/δ with respect to the logarithms of streamwise and spanwise wavenumber for a Blasius boundary layer with $Re_\tau = 1000, \omega = 0$. Constant-color areas represent areas with a single power law for y_m in terms of Re_τ and k.

Because the dominant balance results in an algebraic equation for η, rather than a differential equation, there is no obvious analytic result for the scaling of y_m, but the form is obvious from Figure 4.17. Each region is associated with a constant value of y_m/δ (0.050 for Region 1 and 0.0013 for Region 2) which is approached asymptotically as k or m approaches infinity.

Region 3

In region 3, m is sufficiently small that the scaling of region 2 in Section 4.3 holds, resulting in the observed scalings of $\sigma_1 \propto k^{-2/3}$ and $y_m \propto k^{-1/3}$.

Region 4

The complicated scaling in region 4 of Figures 4.15a and 4.15b is due to effects of non-normality, as quantified by $\frac{1}{\phi_1^* Q \psi_1^*}$ in Figure 4.13.

The source of the non-normality is easily identified as the only cross-term in the Squire equation, $im\partial_y\langle\overline{u}\rangle v$, which is non-zero for $m \neq 0$. Given the dominant balance identified for regions 1 and 2 in Equation 4.28, this term is expected to be most influential where its coefficient is large compared to the other coefficients in the balance. In other words, non-normality is expected where the quantity $\frac{m}{k+(k^2+m^2)/Re_\tau}$ is large. This quantity is plotted in Figure 4.18, showing a very good match between the relative strength of the "lift-up" mechanism 5.9b and the effect of non-normality on σ_1.

4.4 Discussion

If resolvent response modes function as a good model for the stationary velocity fields induced by a periodic roughness, then the existence of scalings for low-order representations of the resolvent operator presents a possible design tool for selecting roughness surfaces. For example, researchers desiring a roughness surface which creates spatial variation in mean velocity throughout the boundary layer may choose a spanwise-varying roughness which maximizes non-normal effects in order to achieve the high y_m exhibited in the small-k, moderate-m region of Figure 4.16. Indeed the non-normal mechanism may be responsible for the boundary-layer-spanning secondary flows reported for streamwise-aligned roughness by, e.g., Barros et al. [6].

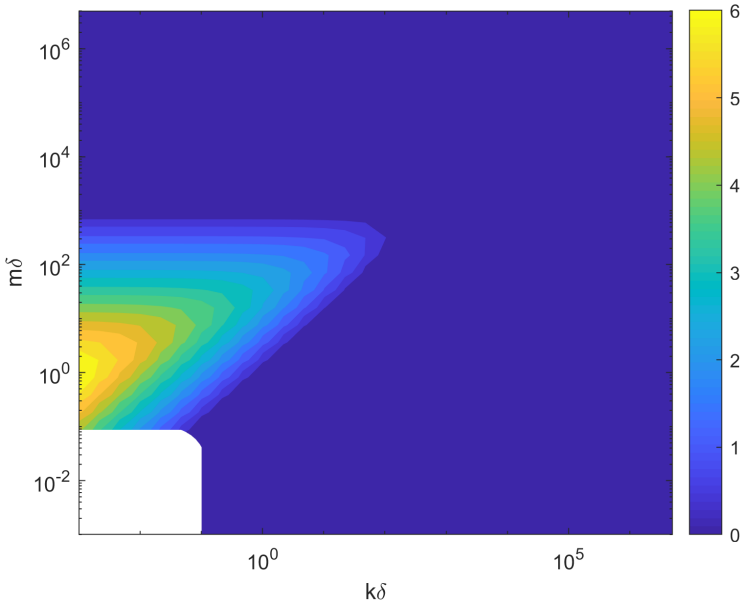

Figure 4.18: Relative influence on σ_1, as estimated by $\frac{m}{k+(k^2+m^2)/Re_\tau}$ for a Blasius boundary layer with $Re_\tau = 1000, \omega = 0$. In the white region, computed singular values did not converge sufficiently as grid resolution was increased.

Chapter 5

MODELING NON-LINEAR INTERACTIONS IN A ROUGH-WALL BOUNDARY LAYER

This chapter will introduce a novel, efficient, low-order model to qualitatively predict the power spectrum modulation measured in Chapter 3. The model limits computational cost by considering only a single pair of convecting wavenumbers and their interactions with a static velocity Fourier mode which has zero frequency and is identical in wavenumber to the roughness. The three wavenumbers are triadically compatible, and each Fourier mode is represented by the most-amplified response mode of the corresponding resolvent operator.

5.1 Modeling Scale Modulation

The scale-dependent modulation of the power spectrum presented in Chapter 3 was identified as a feature that is unique to boundary layers with static roughness and which is the result of non-linear interactions between the stationary velocity Fourier modes (which are induced linearly by the roughness) and pairs of triadically-compatible convecting velocity Fourier modes. This section will explore this relationship and provide a methodology for modeling these interactions at low order.

Consider a full, arbitrary velocity field $\boldsymbol{u}(x, y, z, t)$ as a sum of velocity Fourier modes $\hat{\boldsymbol{u}}_p = \hat{\boldsymbol{u}}(y; k_p, m_p, \omega_p)$, as in Equation 5.1.

$$\boldsymbol{u}(x, y, z, t) = \sum_p \hat{\boldsymbol{u}}_p e^{i(k_p x + m_p z - \omega_p t)} + c.c. \tag{5.1}$$

The Fourier transform in time of $\boldsymbol{u}(x, y, z, t)$ is defined to be $\mathcal{U}(x, y, z; \omega)$ in Equation 5.2 and can be evaluated as Equation 5.3 after applying the restriction that $\omega_p, \omega \geq 0$.

$$\mathcal{U}(x, y, z; \omega) = \overline{e^{i\omega t} \sum_{p=1} \hat{\boldsymbol{u}}_p e^{i(k_p x + m_p z - \omega_p t)} + c.c.} \tag{5.2}$$

$$\mathcal{U}(x, y, z; \omega) = \sum_{\substack{p=1 \\ \omega=\omega_p}} \hat{\boldsymbol{u}}_p e^{i(k_p x + m_p z)} \tag{5.3}$$

The velocity power spectrum in time $\Phi(x, y, z; \omega)$ of such a flow is the energy associated with a particular angular frequency ω, defined in Equation 5.4. Expanding the multiplication then results in Equation 5.5, which is an expression of the power spectrum as a double summation.

The streamwise power spectrum $\Phi(x, y, z; \omega)$ at a particular point can then be given as a sum over pairs of streamwise velocity Fourier modes $\hat{u}_p$ and $\hat{u}_q$ with the same frequency:

$$\Phi(x, y, z; \omega) = |\mathcal{U}(x, y, z; \omega)|^2 = \left(\sum_{\substack{p=1 \\ \omega=\omega_p}}^{\infty} \hat{\boldsymbol{u}}_p e^{i(k_p x + m_p z)} \right) \left(\sum_{\substack{q=1 \\ \omega=\omega_q}}^{\infty} \hat{\boldsymbol{u}}_q e^{i(k_q x + m_q z)} \right)^* . \tag{5.4}$$

$$\Phi(x, y, z; \omega) = \sum_{\omega_p=\omega} \sum_{\omega_q=\omega} \hat{u}_p \hat{u}_q^* e^{i((k_p - k_q)x + (m_p - m_q)z)}. \tag{5.5}$$

Further performing a Fourier transform in the streamwise and spanwise directions gives an expression for Fourier modes of the streamwise power spectrum as in Equation 5.6, with conditions on the summation which enforce triadic compatibility of the pairs of modes with the selected wavenumbers k and m.

$$\hat{\Phi}(y, \omega; k, m) = \sum_{\omega_p=\omega} \sum_{\substack{k_p - k_q = k \\ m_p - m_q = m \\ \omega_q = \omega}} \hat{u}_p \hat{u}_q^* . \tag{5.6}$$

If a mode $\hat{u}_p^0$ corresponds to a Fourier mode of streamwise velocity in a smooth wall boundary layer, then the equivalent Fourier mode for an arbitrary rough-wall boundary layer $\hat{u}_p$ may be represented as $\hat{u}_p^0 + \Delta\hat{u}_p$, with the Δ term representing the difference between the smooth- and the rough-wall boundary layers. These relationships are represented visually in Figure 5.1. In Figure 5.1a, non-linear interactions within a smooth-wall flow result in $\hat{f}_p^0$, forcing at wavenumber (k_p, m_p, ω_p). This smooth-wall forcing at wavenumber p is acted on by the corresponding resolvent operator H_p to produce a velocity Fourier mode $\hat{u}_p^0$ at wavenumber p. This velocity Fourier mode interacts with the triadically-compatible velocity Fourier mode $\hat{u}_q^0$ at wavenumber q to contribute to the scale modulation $\hat{\Phi}_r$ which is necessarily zero for a spatially homogeneous smooth-wall boundary layer. When a static velocity Fourier mode at the roughness wavenumber $\hat{u}_r$ is introduced by a coherent

roughness, the forcing terms are augmented by a change term $\Delta\hat{f}$ due to additional triadic interactions with the roughness mode. When the linear resolvent operators act on the augmented forcing terms, the resulting convecting velocity Fourier modes are also augmented by $\Delta\hat{u} = H\Delta\hat{f}$. The total convecting velocity Fourier modes $\hat{u} = \hat{u}^0 + \Delta\hat{u}$ interact to produce a non-zero scale modulation $\hat{\Phi}_r$. Subtracting the two diagrams yields Figure 5.1c, which serves as a sketch of the algorithm presented in this section to predict scale modulation.

$$\hat{\Phi}(y,\omega;k,m) = \sum_{\omega_p=\omega} \sum_{\substack{k_p-k_q=k \\ m_p-m_q=m \\ \omega_q=\omega}} (\hat{u}_p^0 + \Delta\hat{u}_p)(\hat{u}_q^0 + \Delta\hat{u}_q)^*. \tag{5.7}$$

For the case of a zero pressure gradient smooth-wall boundary layer which is homogeneous in x and z, the above quantity $\hat{\Phi}(y,\omega;k,m)$ is identically zero for non-zero wavenumbers, as all flow statistics are homogeneous in the x and z directions. In other words, with a superscript 0 indicating a smooth-wall quantity, Equation 5.8 holds.

$$\hat{\Phi}^0(y,\omega;k,m) = \sum_{\omega_p=\omega} \sum_{\substack{k_p-k_q=k \\ m_p-m_q=m \\ \omega_q=\omega}} \hat{u}_p^0 \hat{u}_q^{0*} = 0. \tag{5.8}$$

Subtracting Equation 5.8 from Equation 5.7 and eliminating the second-order term in $\Delta\hat{u}$ yields the approximation for $\hat{\Phi}(y,\omega;k,m)$ in Equation 5.9. The approximation will hold when changes in the velocity field due to roughness are small compared to the velocity field.

$$\hat{\Phi}(y,\omega;k,m) \approx \sum_{\omega_p=\omega} \sum_{\substack{k_p-k_q=k \\ m_p-m_q=m \\ \omega_q=\omega}} \hat{u}_p^0 \Delta\hat{u}_q^* + \hat{u}_q^{0*} \Delta\hat{u}_p. \tag{5.9}$$

Through a similar subtraction process the $\Delta\hat{u}$ terms can be expressed in terms of the resolvent operator H and forcing vector $\hat{f}$ at that wavenumber-frequency.

$$\Delta\hat{u}_p = H_p \Delta\hat{f}_p. \tag{5.10}$$

$$\Delta\hat{u}_q = H_q \Delta\hat{f}_q. \tag{5.11}$$

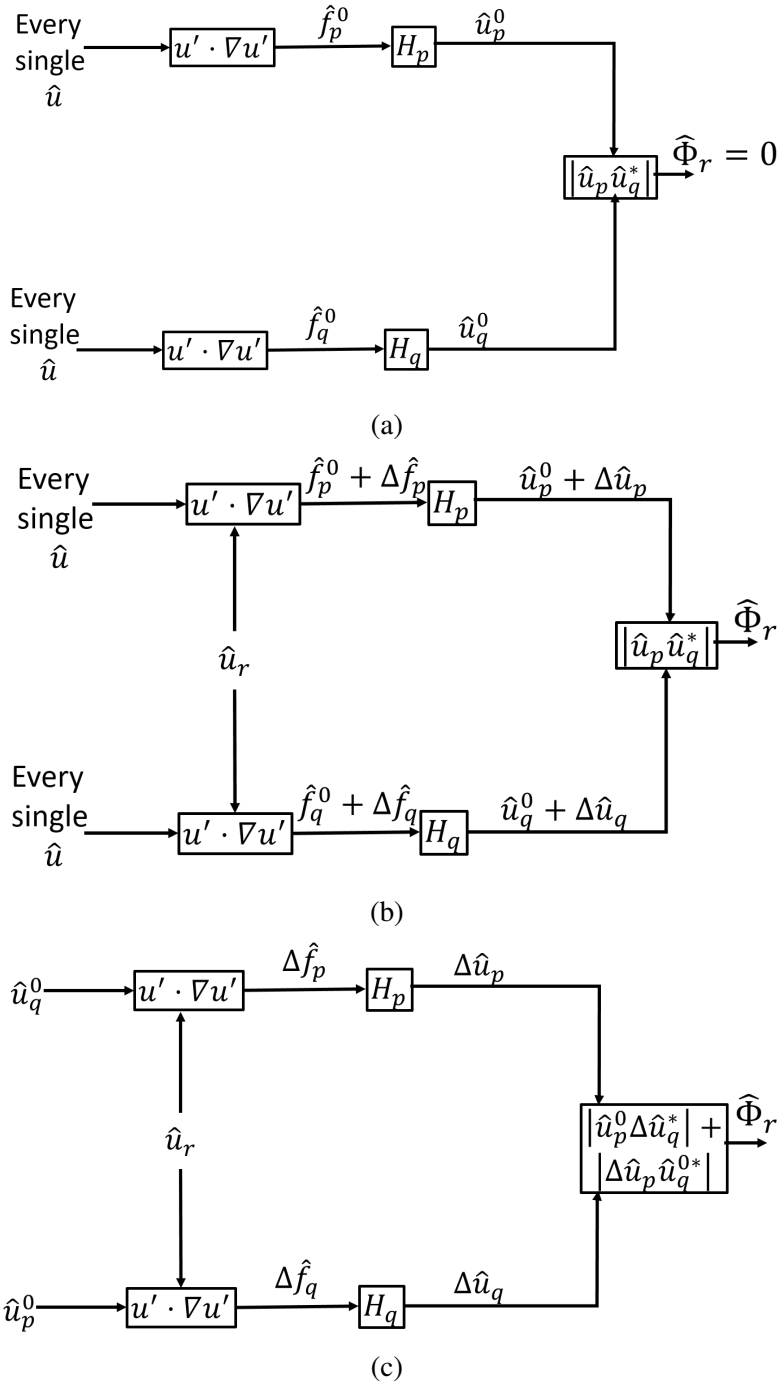

Figure 5.1: Block diagram representation of scale modulation $\hat{\Phi}_r = \hat{\Phi}(y, \omega; k, m)$ for a) the smooth-wall case, b)the rough-wall case, and c) the smooth-wall case subtracted from the rough-wall case.

Modeling the velocity Fourier mode at each wavenumber as a scalar multiple (with complex coefficient a) of the most-amplified resolvent response mode (e.g. $\psi_{p,1}$ for mode p) and the resolvent operator as the product of the most-amplified singular value and singular vectors yields Equations 5.12 and 5.13. This assumption is warranted if the resolvent is low-rank, with a large first singular value compared to the rest, and the forcing vector is not orthogonal to the leading resolvent forcing mode.

$$\hat{u}_p^0 \approx a_p^0 C_p \psi_{p,1}. \tag{5.12}$$

$$H_p \approx \sigma_{p,1} \psi_{p,1} \phi_{p,1}^* Q_p. \tag{5.13}$$

As we wish to model the non-linear interactions involving the roughness, we introduce the roughness mode $\hat{u}(k, m, 0)$ which has zero frequency and non-zero wavenumber. For the experimental data in Chapter 3, these modes are non-zero when k and m are integer multiples of the roughness wavelength.

$$\hat{u}(k, m, 0) \approx a_r C_r \psi_{r,1}. \tag{5.14}$$

In this low-order framework, the change in forcing vectors $\Delta\hat{f}$ can be represented in terms of resolvent response modes ψ as in Equations 5.15 and 5.16, following the definition of forcing in Chapter 3.

$$\Delta\hat{f}_p \approx -a_q^0 C_q \psi_{q,1} \cdot \nabla a_r C_r \psi_{r,1} - a_r C_r \psi_{r,1} \cdot \nabla a_q^0 C_q \psi_{q,1}. \tag{5.15}$$

$$\Delta\hat{f}_q \approx -a_p^0 C_p \psi_{p,1} \cdot \nabla (a_r C_r \psi_{r,1})^* - (a_r C_r \psi_{r,1})^* \cdot \nabla a_p^0 C_p \psi_{p,1}. \tag{5.16}$$

Substituting Equations 5.13, 5.15, and 5.16 into Equations 5.10 and 5.11 gives Equations 5.17 and 5.18 as approximations for the change in velocity Fourier modes due to roughness.

$$\begin{aligned} \Delta\hat{u}_p &\approx \Delta a_p C_p \psi_{p,1} \\ &\approx -\sigma_{p,1} C_p \psi_{p,1} \phi_{p,1}^* Q_p M_p^{-1} B_p (a_q^0 C_q \psi_{q,1} \cdot \nabla a_r C_r \psi_{r,1} + a_r C_r \psi_{r,1} \cdot \nabla a_q^0 C_q \psi_{q,1}). \end{aligned} \tag{5.17}$$

$$\begin{aligned}\Delta\hat{u}_q &\approx \Delta a_q C_q \psi_{q,1} \\ &\approx -\sigma_{q,1} C_q \psi_{q,1} \phi^*_{q,1} Q_q M_q^{-1} B_q (a_p^0 C_p \psi_{p,1} \cdot \nabla (a_r C_r \psi_{r,1})^* + (a_r C_r \psi_{r,1})^* \cdot \nabla a_p^0 C_p \psi_{p,1}).\end{aligned} \tag{5.18}$$

For conciseness, we define interaction coefficients N_p and N_q as follows. These are scalar values which are functions only of the three sets of wavenumbers and frequencies.

$$N_p = -\sigma_{p,1} \phi^*_{p,1} Q_p M_p^{-1} B_p (C_q \psi_{q,1} \cdot \nabla C_r \psi_{r,1} + C_r \psi_{r,1} \cdot \nabla C_q \psi_{q,1}). \tag{5.19}$$

$$N_q = -\sigma_{q,1} \phi^*_{q,1} Q_q M_q^{-1} B_q (C_p \psi_{p,1} \cdot \nabla (C_r \psi_{r,1})^* + (C_r \psi_{r,1})^* \cdot \nabla C_p \psi_{p,1}). \tag{5.20}$$

$$\Delta\hat{u}_p \approx N_p a_q^0 a_r C_p \psi_{p,1}. \tag{5.21}$$

$$\Delta\hat{u}_q \approx N_q a_p^0 a_r^* C_q \psi_{q,1}. \tag{5.22}$$

Substituting all of this back into Equation 5.9 yields Equation 5.23, which can be rearranged to obtain Equation 5.24.

$$\hat{\Phi}(y, \omega; k, m) \approx \sum_{\omega_p = \omega} \sum_{\substack{k_p - k_q = k \\ m_p - m_q = m \\ \omega_q = \omega}} a_p^0 C_p \psi_{p,1} (N_q a_p^0 a_r^* C_q \psi_{q,1})^* + (a_q^0 C_q \psi_{q,1})^* (N_p a_q^0 a_r C_p \psi_{p,1}). \tag{5.23}$$

$$\hat{\Phi}(y, \omega; k, m) \approx \sum_{\omega_p = \omega} \sum_{\substack{k_p - k_q = k \\ m_p - m_q = m \\ \omega_q = \omega}} a_r C_p \psi_{p,1} (C_q \psi_{q,1})^* (|a_p^0|^2 N_q^* + |a_q^0|^2 N_p). \tag{5.24}$$

The expression can be further simplified by modeling the entire summation with only two convecting modes, which must satisfy the triadic constraint with the static mode.

$$\hat{\Phi}(y, \omega; k, m) \approx a_r C_p \psi_{p,1} (C_q \psi_{q,1})^* (|a_p^0|^2 N_q^* + |a_q^0|^2 N_p). \tag{5.25}$$

While the interaction coefficients can be calculated exactly from the resolvent modes, the coefficients a must be modeled from the data. These quantities are proportional to the squared coefficient of the velocity Fourier modes, as is the power spectrum, shown in Equation 5.5. The squared coefficients for each mode (p and q) are therefore modeled as proportional to the power spectrum evaluated at the critical layer y^c for that mode, defined in Equation 5.28, where they are expected to have the greatest amplitude and therefore the clearest signature in the power spectrum.

$$|C_p\psi_{p,1}(C_q\psi_{q,1})^*||a_p^0|^2 \propto \langle\Phi(y_p^c,\omega)\rangle. \tag{5.26}$$

$$|C_p\psi_{p,1}(C_q\psi_{q,1})^*||a_q^0|^2 \propto \langle\Phi(y_q^c,\omega)\rangle. \tag{5.27}$$

$$\langle\overline{u}(y_p^c)\rangle = \omega/k_p. \tag{5.28}$$

Finally the model for the spatial Fourier modes of the premultiplied streamwise power spectrum $\omega\hat{\Phi}(y;k,m,\omega)$ measured in Chapter 3 is collected in one quantity named ζ:

$$|\omega\hat{\Phi}(y,\omega;k,m)| \propto \zeta(y,\omega;k,m) \equiv \omega|\langle\Phi(y_p^c;\omega)\rangle^+ N_q^* + \langle\Phi(y_q^c;\omega)N_p\rangle|. \tag{5.29}$$

This quantity is the result of a number of assumptions about the roughness, the velocity field, the resolvent operator, and the nature of the non-linear interactions within a boundary layer, and it gives a quantitative prediction of the behavior of the measurable quantity $|\omega\hat{\Phi}(y,\omega;k,m)|$ as y and ω are varied for a given set of roughness wavenumbers k,m.

5.2 Calculation of ζ

With most-amplified resolvent response modes established as a plausible model for stationary velocity Fourier modes, the quantity ζ defined in Equation 5.29 can now be computed and compared to $|\omega\hat{\Phi}(y,\omega;k,m)|$ to assess its suitability as a model for non-linear interactions in a turbulent rough-wall boundary layer.

As $|\omega\hat{\Phi}(y,\omega;k,m)|$ varies in y and ω for a given set of wavenumbers, $\zeta(y,\omega;k,m)$ will be calculated on a grid in y-ω space for each set of wavenumbers. For each y-ω combination, a set of spatial wavenumbers (k_p,m_p) must be chosen. Once these are

set, the wavenumbers (k_q, m_q) are uniquely determined by triadic constraints to be $(k + k_p, m + m_p)$. The streamwise wavenumber k_p is chosen such that the critical layers y_p^c and y_q^c are equidistant from the nominal y-location y. This is intended to ensure that the chosen modes overlap at y so that they can interact. In the case where $k = 0$, the two modes share a critical layer $y^c = y$. The spanwise wavenumber m_p is chosen such that $m_p^+ = 0.015 - m^+/2$, and therefore $m_q^+ = 0.015 + m^+/2$. In this way, the two modes bracket an inner-normalized spanwise wavenumber of 0.015, which was found by LeHew et al. [38] to contain significant energy in the ω-m streamwise velocity power spectrum over a range of ω and y. The calculated ζ distributions are not highly sensitive to this choice of spanwise wavenumber.

Due to the symmetry of the zero-frequency resolvent operator with respect to (k, m), a given static velocity Fourier mode is equally well-described by $(\pm k, \pm m)$. When one of the wavenumbers (k, m) is zero, the calculation of ζ is unaffected by negating one of the wavenumbers. When both of the wavenumbers are non-zero, the value of ζ is changed by negating one of the wavenumbers. For example, when $(k, m) = (k_r, m_r)$, $(k_p, m_p) = (k_1, 0.015Re_\tau - m_r/2)$ for some k_1 that is a function of the mean velocity profile, y and ω. This will yield the other convecting wavenumber as $(k_q, m_q) = (k_1 + k_r, 0.015Re_\tau + m_r/2)$. Calculating ζ for $(k, m) = (k_r, -m_r)$ will instead give $(k_p, m_p) = (k_1, 0.015Re_\tau + m_r/2)$ and $(k_q, m_q) = (k_1 + k_r, 0.015Re_\tau - m_r/2)$ which, by inspection, are not related to the other pair of convecting wavenumbers by any symmetry.

The resolvent is calculated as described in Section 2.2 with $N = 800$. The velocity profile used as a input to the resolvent is taken to be the observed spatio-temporally averaged velocity field $\langle \overline{u}(y) \rangle$ for the appropriate roughness geometry, with linear interpolation to zero velocity at zero y below the measurement volume.

Figure 5.3a replots the observed static spatial Fourier mode of the streamwise power spectrum $|\omega \hat{\Phi}^+(y, \omega; k_r, m_r)|$ for the R1M roughness, while $\zeta(y, \omega; k_r, m_r)$ is plotted for comparison below. Absolute quantities at particular values of y and ω are not directly comparable, as ζ is modeled as merely proportional to the scale modulation. However, we do expect ζ to predict the relative distribution of scale modulation within y-ω space. Although the match is not perfect, some key features are reproduced. The span in ω of non-zero scale modulation at low y, from roughly $\omega^+ = 0.002$ to $\omega^+ = 0.5$ is predicted well by ζ. The predicted location of the peak in ω is accurate to within an octave. The predicted y-location of the peak is inaccurate, however, with a prediction of $y/\delta = 0.03$ compared to an actual value of

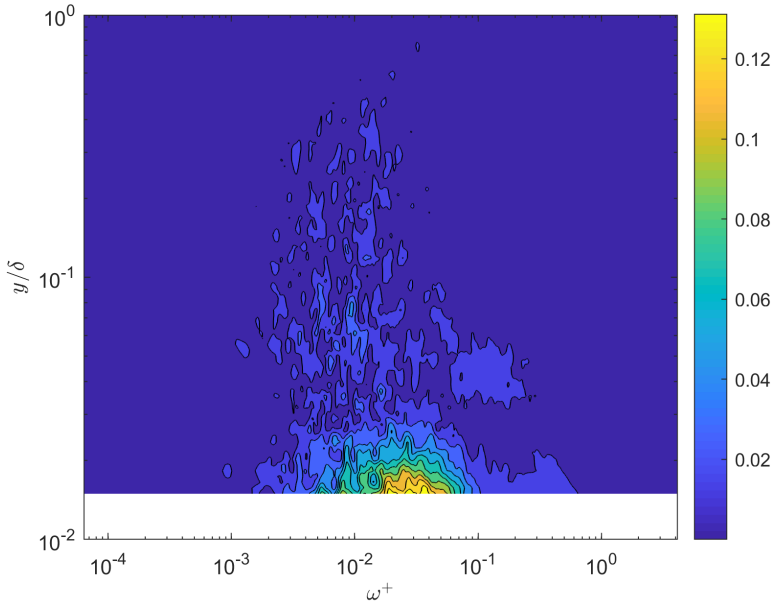

(a)

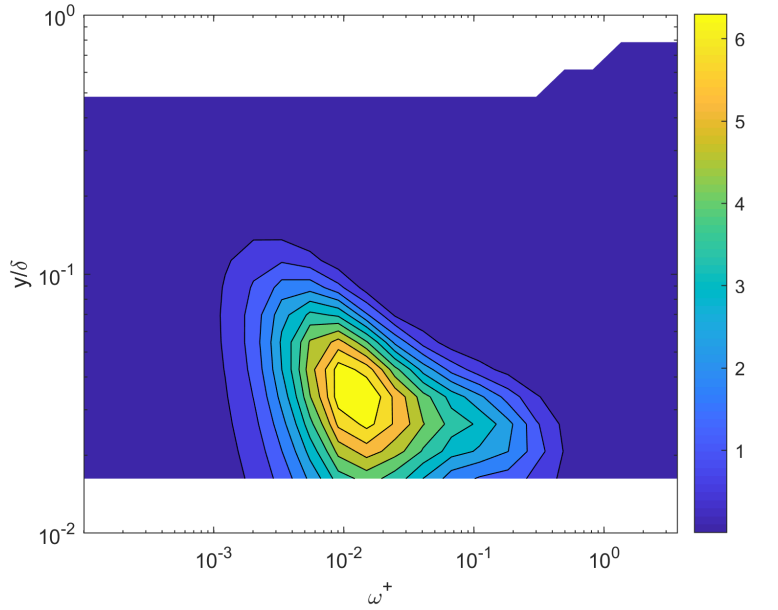

(b)

Figure 5.2: a)Magnitude of the R1M scale modulation $|\widehat{\omega\Phi}^+(y,\omega;k_r,m_r)|$ b)Predicted Scale Modulation $\zeta(y,\omega;k_r,m_r)$.

$y/\delta = 0.015$.

The observed static spatial Fourier mode of the streamwise power spectrum for the R1M roughness $|\omega\hat{\Phi}^+(y, \omega; k_r, -m_r)|$, which is identical to $|\omega\hat{\Phi}^+(y, \omega; k_r, m_r)|$ due to symmetry, is plotted in Figure 5.3, while $\zeta(y, \omega; k_r, -m_r)$ is plotted for comparison below. The match is qualitatively improved from the (k_r, m_r) case. The predicted location of the peak in ω has moved closer to the observed location, located at roughly $y/\delta = 0.02$ compared to an actual value of $y/\delta = 0.015$. The fainter, outer contours are also a better match, with nearly vertical contours on the left, low-frequency side, while contours on the right, high-frequency side skew quickly to lower wavenumbers as y increases. This improved match implies that this set of non-linear interactions is more significant to the physics of this rough-wall flow. The concentration of scale modulation at low y is consistent with the observed roughness velocity Fourier mode, which attained its highest measured amplitude at the bottom of the measurement volume. Because ζ is linear with regard to the roughness-coherent velocity Fourier mode, the greatest modulation is expected where this mode has large magnitude.

Actual and predicted scale modulation for the R1M roughness with $(k, m) = (2k_r, 2m_r)$ is plotted in Figure 5.4. The model $\zeta(y, \omega; 2k_r, 2m_r)$ predicts that the scale modulation at low y/δ is skewed toward higher ω^+ compared to the scale modulation higher in the boundary layer, consistent with the data. The scale modulation is noisy due to the low observed amplitude, making more detailed comparison difficult.

Figure 5.5 compares the predicted scale modulation for $(k, m) = (2k_r, 0)$ to the actual scale modulation for R1M roughness. This mode's observed scale modulation is also noisy, but there does appear to be a nearly two-lobed structure in both plots, with a stronger lobe centered around roughly $\omega^+ = 0.02$ and extending well into the boundary layer, while a weaker lobe centered around roughly $\omega^+ = 0.15$ is much more constrained in height.

Finally, predicted and measured scale modulation for R1M roughness for $(k, m) = (0, 2m_r)$ are plotted in Figure 5.6. There is almost no relation between the two plots, indicating that the model is entirely unpredictive for this set of wavenumbers. This may be due to modeling the stationary velocity Fourier mode as the most-amplified resolvent mode. As discussed in the previous section, the second resolvent mode was actually a better fit for this set of wavenumbers.

Moving on to R2M roughness, Figure 5.7 shows the ζ and $|\omega\hat{\Phi}^+|$ fields for the

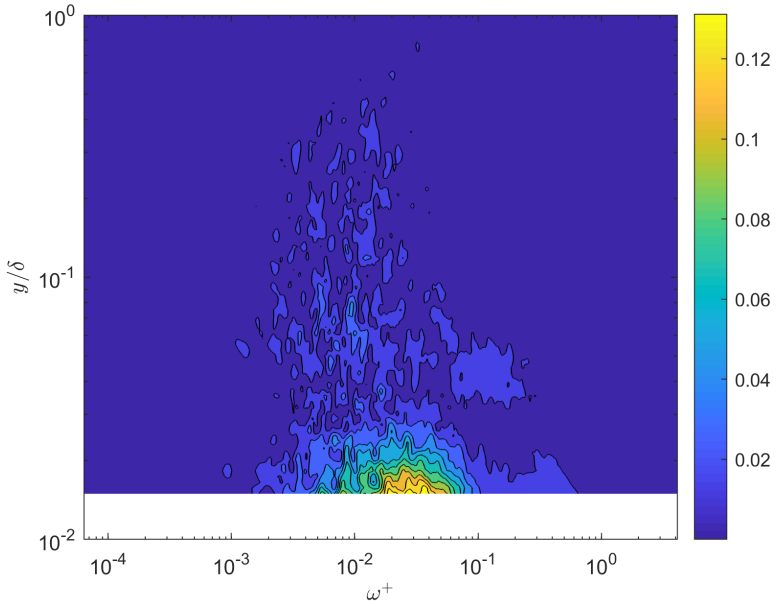

(a)

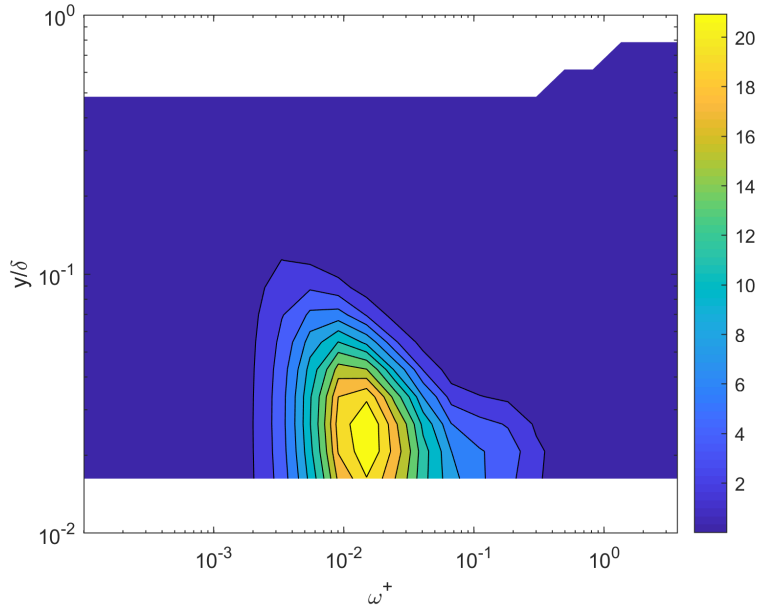

(b)

Figure 5.3: a)Magnitude of the R1M scale modulation $|\widehat{\omega\Phi}^{+}(y,\omega;k_r,-m_r)|$ b)Predicted Scale Modulation $\zeta(y,\omega;k_r,-m_r)$.

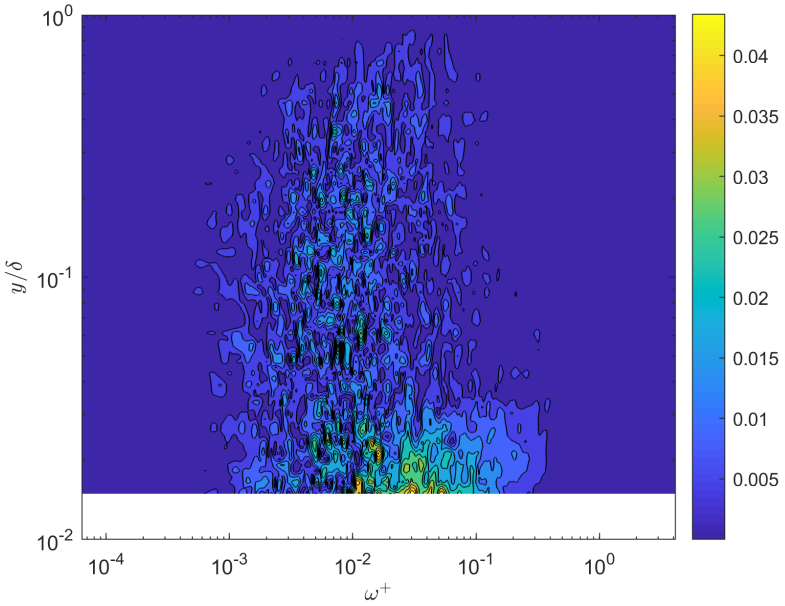

(a)

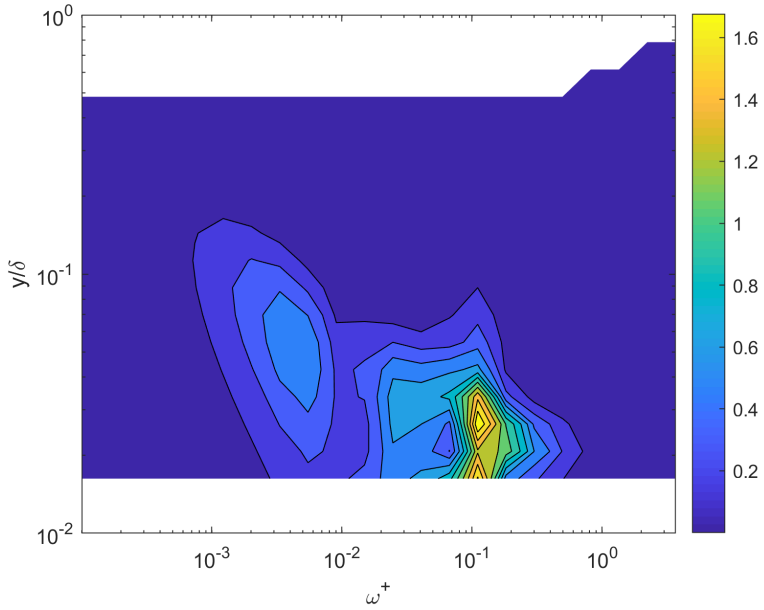

(b)

Figure 5.4: a)Magnitude of the R1M scale modulation $|\widehat{\omega\Phi}^+(y,\omega;2k_r,2m_r)|$ b)Predicted Scale Modulation $\zeta(y,\omega;2k_r,2m_r)$.

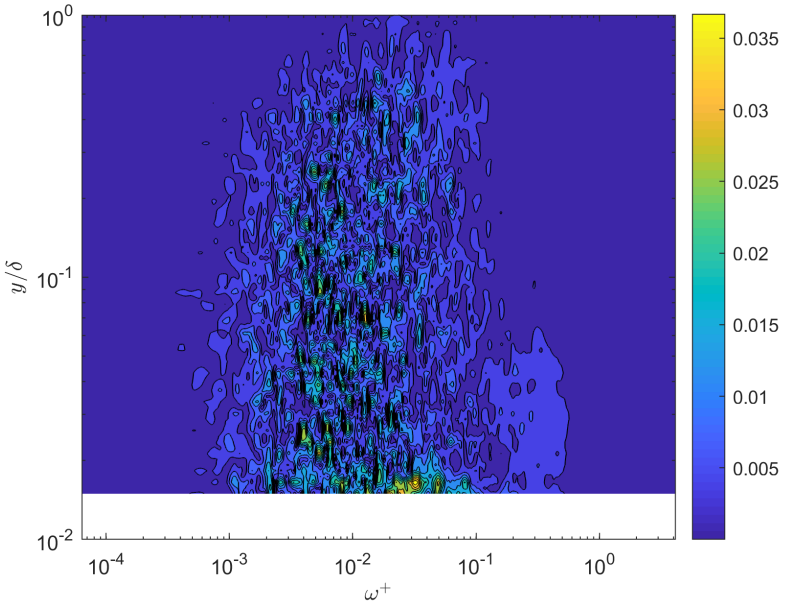

(a)

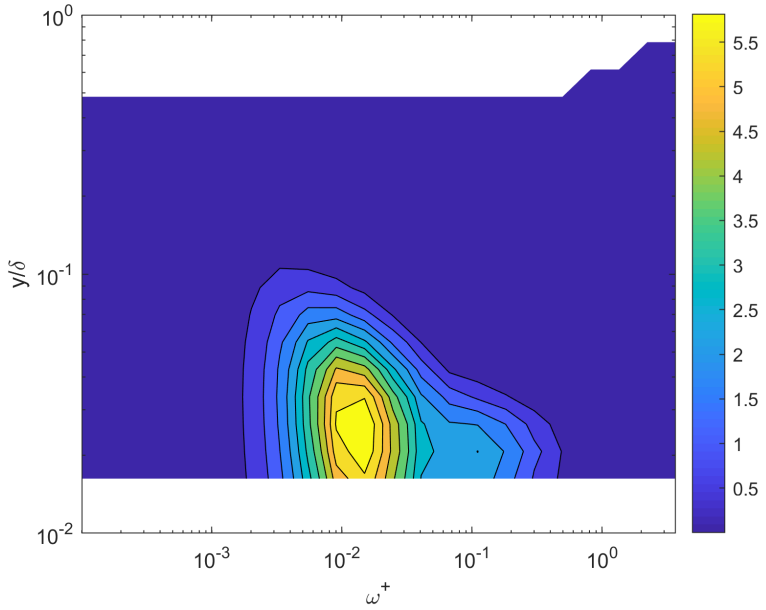

(b)

Figure 5.5: a)Magnitude of the R1M scale modulation $|\widehat{\omega\Phi}^+(y,\omega;2k_r,0)|$ b)Predicted Scale Modulation $\zeta(y,\omega;2k_r,0)$.

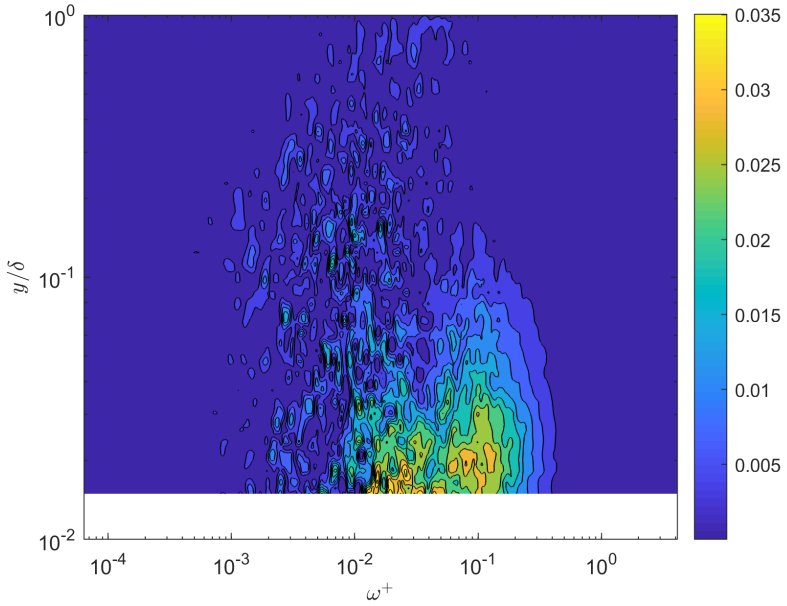

(a)

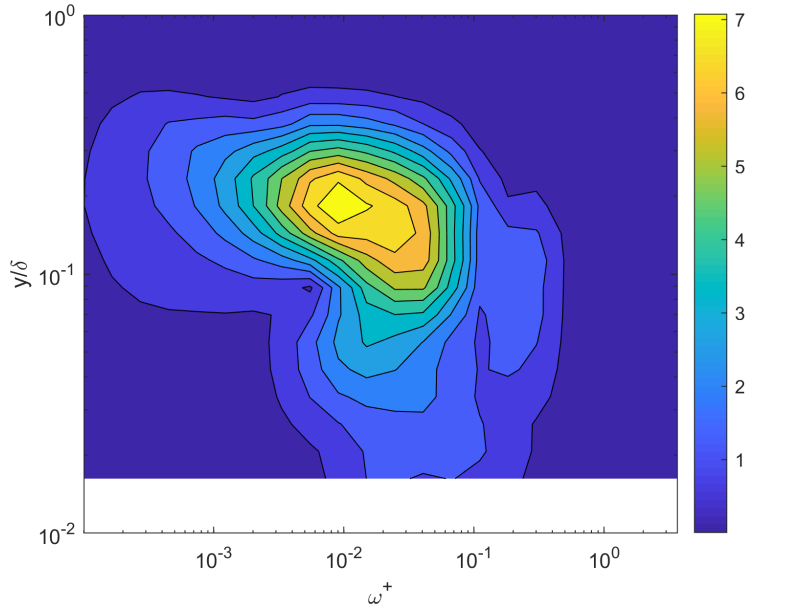

(b)

Figure 5.6: a)Magnitude of the R1M scale modulation $|\widehat{\omega\Phi}^{+}(y,\omega;0,2m_r)|$ b)Predicted Scale Modulation $\zeta(y,\omega;0,2m_r)$.

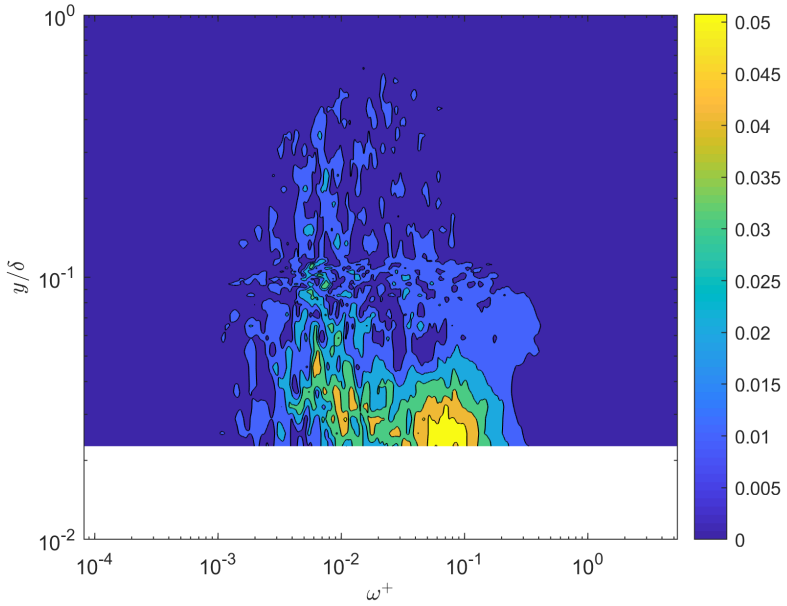

(a)

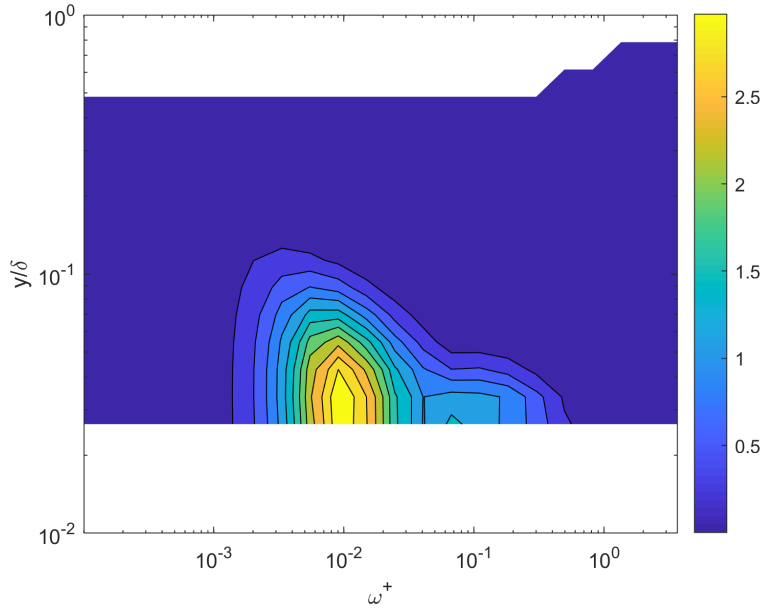

(b)

Figure 5.7: a)Magnitude of the R2M scale modulation $|\widehat{\omega\Phi}^+(y,\omega;k_r,0)|$ b)Predicted Scale Modulation $\zeta(y,\omega;k_r,0)$.

$(k, m) = (k_r, 0)$ case. Consistent with the experimental data, the ζ field predicts a two-lobed structure, with a taller one centered around $\omega^+ = 0.01$ and a shorter one around $\omega^+ = 0.07$. In both plots, the peaks are located at the bottom of the measurement volume, around $y/\delta = 0.015$. The relative magnitude of the two peaks are reversed, however. In addition, the wall-normal extent of the scale modulation is underestimated by ζ, especially at higher frequencies. The observed scale modulation includes a "bulge" extending outward towards higher frequencies at roughly $y/\delta = 0.06$ which is missing in the ζ field. The scale modulation observed here is also consistent with the observed roughness-correlated velocity Fourier mode: it extends well into the boundary layer, but attains a maximum at low y. Despite these small discrepancies, ζ presents a plausible qualitative model for the scale modulation at this wavenumber.

Predicted and actual scale modulation for the R2M roughness, $(k, m) = (0, m_r)$, are plotted in Figure 5.8. Again, ζ predicts a two-lobed structure, with the lobes separated in both y and ω, which is consistent with the experimental measurements, though the relative magnitudes of the peaks are again reversed. The frequencies of the peaks are also consistent, at roughly $\omega^+ = 0.02$ and $\omega^+ = 0.09$. The lower, higher-frequency peak is located by ζ at a different wall-normal location, at around $y/\delta = 0.04$ rather than at the lower end of the measurement volume. Additionally, the wall-normal extent of the high-frequency lobe, which extends to $y/\delta = 0.1$ in the observed scale modulation, is underestimated by ζ, which shows a more compact lobe. The location of the higher lobe in y is consistent with the observed static velocity Fourier mode corresponding to this wavenumber: there is one peak around $y/\delta = 0.2$. Though some discrepancies exist, ζ is qualitatively consistent with the observed scale modulation in several respects at this wavenumber, despite the simplicity of the model.

Finally, the predicted and actual scale modulation for the case of $(k, m) = (k_r, m_r)$ for R2M roughness are plotted in Figure 5.9. There is no qualitative resemblance between the plots. The ζ field shows two separate lobes while the actual scale modulation does not have such a distinct shape. The scale modulation for this mode is not well predicted by ζ.

In summary, the simple model ζ tends to be a reasonable model for the scale modulation $|\omega\hat{\Phi}^+(y, \omega; k, m)|$ under certain circumstances, predicting scale modulation in y, ω which is consistent with experimental data. Certainly, the static resolvent mode must accurately capture the behavior of the stationary velocity Fourier mode,

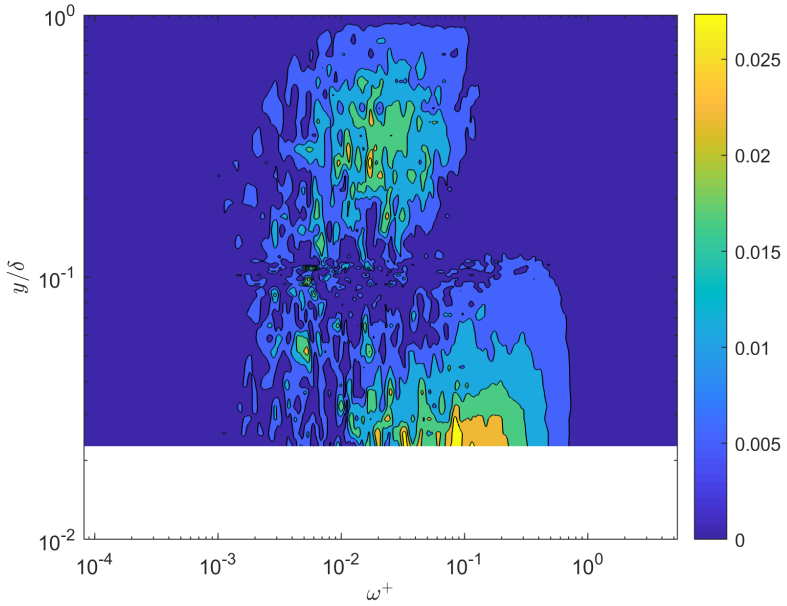

(a)

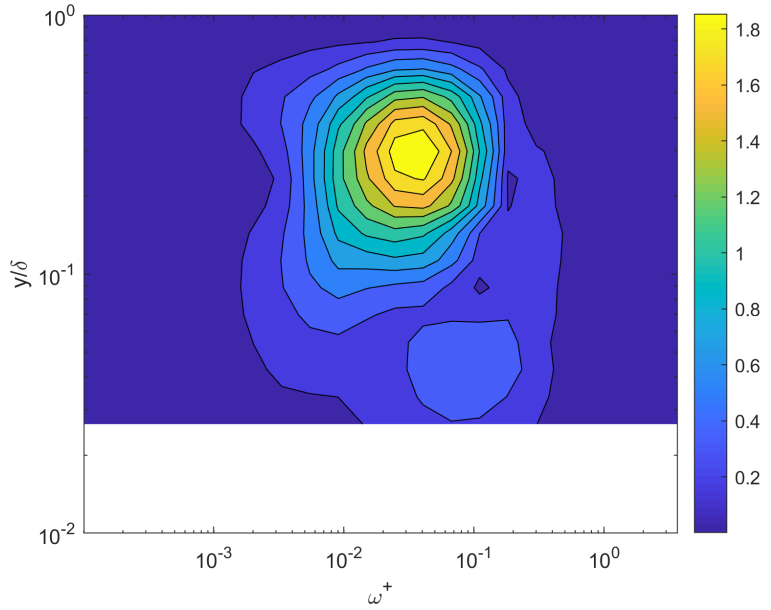

(b)

Figure 5.8: a)Magnitude of the R2M scale modulation $|\widehat{\omega\Phi}^+(y,\omega;0,m_r)|$ b)Predicted Scale Modulation $\zeta(y,\omega;0,m_r)$.

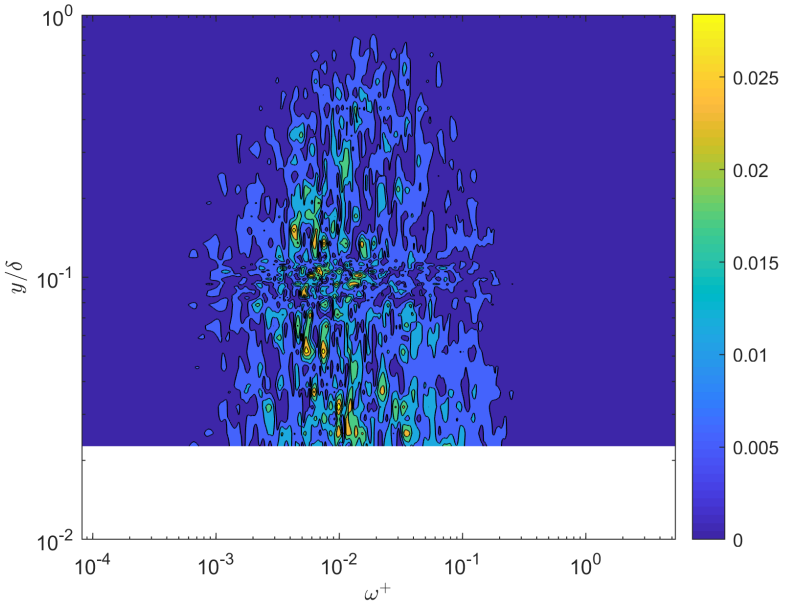

(a)

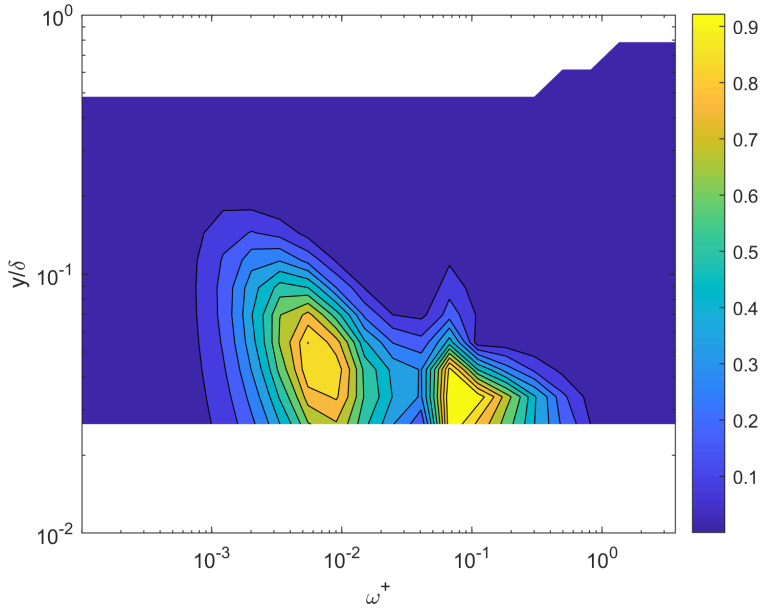

(b)

Figure 5.9: a)Magnitude of the R2M scale modulation $|\widehat{\omega\Phi}^+(y,\omega;k_r,m_r)|$ b)Predicted Scale Modulation $\zeta(y,\omega;k_r,m_r)$.

as that is a key assumption in the model, and the y-location of observed modulation corresponds well to peaks in the observed static velocity Fourier modes. Furthermore, ζ is more predictive for the wavenumber combinations which are directly related to a roughness mode ($(k, m) = (k_r, m_r)$ for R1M and $(k, m) = (k_r, 0), (0, m_r)$ for R2M). This may reflect the fact that the other stationary modes are themselves formed by non-linear interactions. The most accurate modeling occurred for the R2M roughness, possibly because the static modes are two-dimensional. In any case, it is remarkable that such a simple model has any predictive power at all. Its qualitative success may indicate that nonlinear interactions resulting from roughness in a turbulent boundary layer may be "low rank" in the sense that they can be usefully modeled without the expense and computational intractability of direct numerical simulation at high Reynolds number.

Chapter 6

CONCLUSIONS AND FUTURE WORK

Turbulent boundary layers have been the subject of much experimental, numerical, and analytical work for decades. Recent advances in understanding the turbulent structure and cross-scale interactions in canonical flows (Banyopadhay and Hussain [5], Mathis et al.[42]), combined with work on low-order representations of rough walls (MacDonald et al. [41], Mejia-Alvarez and Christensen [44]), present an opportunity to span the gap between these subfields in a way that answers some of the challenges of both. Chapter 3 describes the spatially-varying flow statistics that distinguish a rough-wall boundary layer from a canonical one, and correlates them to the periodic roughness. The long-wavelength roughness was found to produce a non-convecting velocity Fourier mode which persisted throughout the boundary layer. Flows statistics such as power spectra were also found to vary significantly, though in a more limited y-domain. Chapter 4 relates the stationary velocity Fourier modes to resolvent response modes, and further explores the resolvent analysis of static modes by relating resolvent quantities to asymptotic limits of the Navier-Stokes equations. Chapter 5 explains the relation between the roughness geometry and the spatial distribution of power spectra using a low-order model of the additional non-linear forcing introduced by the static velocity Fourier mode. Resolvent analysis allowed for a low-order representation of that mode and two triadically-compatible convecting modes.

From the perspective of the amplitude-modulation literature, this work can be seen as introducing a novel perturbation on top of a canonical flow. The static nature of the perturbation allows a clean separation from the modulated scales and a finely resolved measure of the modulation at each individual scale, which can be related physically to the nonlinear forcing. A simple low-order model provides a tractable but qualitatively accurate prediction of this modulation. Asymptotic analysis of the low-order behavior predicts the characteristics of the perturbation.

From a rough-wall turbulence perspective, this work builds on the low-order roughness literature by creating the simplest possible roughness, with the fewest possible scales. The sinusoidal roughness alters the boundary condition of the flow in a simple way, which creates in a direct, linear way a static inhomogeneous mean ve-

locity field, or secondary flow, with simple spatial spectral composition in the flow. This mean velocity field interacts nonlinearly with the turbulence of the boundary layer at a range of other scales to alter the mean quantities of the flow. Due to the large wall-parallel wavelengths compared to the boundary layer thickness and non-negligible amplitude, the effects of the roughness extend through much of the boundary layer, and hot wire anemometry can be used to measure the spatial variation in mean quantities, statistics, and power spectra required to trace the effects of the roughness. The non-linear forcing field of the rough wall is modeled in the simplest possible way, as a perturbation to the smooth-wall forcing which involves only the roughness wavenumber and two additional convecting wavenumbers.

Real-world roughness is substantially more complicated than the present case of one or two individual sinusoids. It may take as many as 16 modes (Mejia-Alvarez and Christensen [44]) to accurately reproduce mean-flow quantities of interest for rough-wall boundary layers. Due to the nominally-linear nature of the boundary condition, it is proposed that the effects of a number of these simple roughnesses can be linearly superposed to predict the behavior of a real-world roughness in wall-bounded flow. The validity of such linear superposition is consistent with the results of the R2M case, where the individual scale modulation plots of the streamwise-only mode and of the spanwise-only mode were well predicted by their respective ζ calculations. The lack of fidelity between ζ and scale modulation for static wavenumbers which are not directly imposed does point to a gap in the modelling procedure, but this may not be so significant for real world flows, where roughness exhibits a broad range of wavenumbers. In those circumstances, the mechanism for scale modulation modelled here may dominate the mechanisms for scale modulation at harmonic static wavenumbers which are not captured. Roughnesses outside the "wavy-wall" regime have also not been evaluated within this framework. The steeper slopes associated with shorter wavelengths may cause a persistent separation bubble which would introduce more scales into the flow at the wall.

Finally, this work was conceived and funded as part of a long-term scientific campaign to better understand rough-wall flows, with the ultimate goal of understanding and shaping the turbulence within a practical turbulent boundary to reduce drag or enhance other mean-flow characteristics. This work does not directly address drag, which is affected by self-interactions of velocity Fourier modes to produce Reynolds stress. It does, however, illuminate aspects of non-linear forcing within a turbulent boundary layer which could contribute to eventually "closing the loop" in

the analysis and control of practical turbulent shear flows.

BIBLIOGRAPHY

[1] J Allen, M Shockling, G Kunkel, and A Smits. Turbulent flow in smooth and rough pipes. *Phil. Trans. R. Soc. A*, 365(1852):699–714, 2007.

[2] W Anderson. Amplitude modulation of streamwise velocity fluctuations in the roughness sublayer: evidence from large-eddy simulations. *J. Fluid Mech.*, 789:567–588, 2016.

[3] W Anderson, J Barros, K Christensen, and A Awasthi. Numerical and experimental study of mechanisms responsible for turbulent secondary flows in boundary layer flows over spanwise heterogeneous roughness. *J. Fluid Mech.*, 768:316–347, 2015.

[4] A Awasthi and W Anderson. Numerical study of turbulent channel flow perturbed by spanwise topographic heterogeneity: Amplitude and frequency modulation within low-and high-momentum pathways. *Phys. Rev. Fluids*, 3 (4):044602, 2018.

[5] P Bandyopadhyay and A Hussain. The coupling between scales in shear flows. *Phys. Fluids*, 27(9):2221–2228, 1984.

[6] J Barros and K Christensen. Observations of turbulent secondary flows in a rough-wall boundary layer. *J. Fluid Mech.*, 748, 2014.

[7] G Berkooz, P Holmes, and J Lumley. The proper orthogonal decomposition in the analysis of turbulent flows. *Ann. Rev. Fluid Mech.*, 25(1):539–575, 1993.

[8] H Blasius. *Grenzschichten in Flüssigkeiten mit kleiner Reibung*. Druck von BG Teubner, 1907.

[9] J Burgers. *The motion of a fluid in the boundary layer along a plane smooth surface*. Waltman, 1925.

[10] B Cantwell. Organized motion in turbulent flow. *Ann. Rev. Fluid Mech.*, 13 (1):457–515, 1981.

[11] L Chan, M MacDonald, D Chung, N Hutchins, and A Ooi. Secondary motion in turbulent pipe flow with three-dimensional roughness. *J. Fluid Mech.*, 854: 5–33, 2018.

[12] A Chavarin and M Luhar. Resolvent analysis for turbulent channel flow with riblets. *arXiv preprint arXiv:1812.07178*, 2018.

[13] D. Chung and B. McKeon. Large-eddy simulation investigation of large-scale structures in a long channel flow. *J. Fluid Mech.*, 661:341–364, 2010.

[14] C Colebrook. Turbulent flow in pipes, with particular reference to the transition region between the smooth and rough pipe laws. *J. Inst. of Civ. Eng.*, 11 (4):133–156, 1939.

[15] D De Graaff and J Eaton. Reynolds-number scaling of the flat-plate turbulent boundary layer. *J. Fluid Mech.*, 422:319–346, 2000.

[16] T Driscoll, N Hale, and L Trefethen. *Chebfun Guide*. Pafnuty Publications, 2014. URL `http://www.chebfun.org/docs/guide/`.

[17] S Duvvuri. *Non-Linear Scale Interactions in a Forced Turbulent Boundary Layer*. PhD thesis, California Institute of Technology, 2016.

[18] S Duvvuri and B McKeon. Triadic scale interactions in a turbulent boundary layer. *J. Fluid Mech.*, 767:R4, 2015.

[19] M Farge. Wavelet transforms and their applications to turbulence. *Ann. Rev. Fluid Mech.*, 24(1):395–458, 1992.

[20] K Flack and M Schultz. Roughness effects on wall-bounded turbulent flows. *Phys. Fluids (1994-present)*, 26(10):101305, 2014.

[21] O Flores and J Jimenez. Effect of wall-boundary disturbances on turbulent channel flows. *J. Fluid Mech.*, 566:357–376, 2006.

[22] M Gaster, C Grosch, and T Jackson. The velocity field created by a shallow bump in a boundary layer. *Phys. Fluids*, 6(9):3079–3085, 1994.

[23] G Gioia and P Chakraborty. Turbulent friction in rough pipes and the energy spectrum of the phenomenological theory. *Phys. Rev. Lett.*, 96(4):044502, 2006.

[24] F Gómez, H Blackburn, M Rudman, A Sharma, and B McKeon. Streamwise-varying steady transpiration control in turbulent pipe flow. *J. Fluid Mech.*, 796:588–616, 2016.

[25] J Hinze. Secondary currents in wall turbulence. *Phys. Fluids*, 10(9):S122–S125, 1967.

[26] J Hong, J Katz, and M Schultz. Near-wall turbulence statistics and flow structures over three-dimensional roughness in a turbulent channel flow. *J. Fluid Mech.*, 667:1–37, 2011.

[27] A Hussain and W Reynolds. The mechanics of an organized wave in turbulent shear flow. *J. Fluid Mech.*, 41(2):241–258, 1970.

[28] N Hutchins and I Marusic. Evidence of very long meandering features in the logarithmic region of turbulent boundary layers. *J. Fluid Mech.*, 579:1–28, 2007.

[29] N Hutchins and I Marusic. Large-scale influences in near-wall turbulence. *Phil. Trans. R. Soc. A*, 365(1852):647–664, 2007.

[30] I Jacobi and B McKeon. Phase relationships between large and small scales in the turbulent boundary layer. *Exp. Fluids*, 54(3):1481, 2013.

[31] T Jelly and A Busse. Reynolds and dispersive shear stress contributions above highly skewed roughness. *J. Fluid Mech.*, 852:710–724, 2018.

[32] J Jimenez. Turbulent flows over rough walls. *Ann. Rev. Fluid Mech.*, 36: 173–196, 2004.

[33] J Jimenez and A Pinelli. The autonomous cycle of near-wall turbulence. *J. Fluid Mech.*, 389:335–359, 1999.

[34] I Jolliffe. Principal component analysis. In *International encyclopedia of statistical science*, pages 1094–1096. Springer, 2011.

[35] K Kim and R Adrian. Very large-scale motion in the outer layer. *Phys. Fluids*, 11(2):417–422, 1999.

[36] Stephen J Kline, William C Reynolds, F Schraub, and P Runstadler. The structure of turbulent boundary layers. *J. Fluid Mech.*, 30(4):741–773, 1967.

[37] J LeHew. *Spatio-temporal analysis of the turbulent boundary layer and an investigation of the effects of periodic disturbances*. PhD thesis, California Institute of Technology, 2012.

[38] J LeHew, M Guala, and B McKeon. A study of the three-dimensional spectral energy distribution in a zero pressure gradient turbulent boundary layer. *Exp. Fluids*, 51(4):997–1012, 2011.

[39] M Luhar, A Sharma, and B McKeon. Opposition control within the resolvent analysis framework. *J. Fluid Mech.*, 749:597–626, 2014.

[40] M Luhar, A Sharma, and B McKeon. A framework for studying the effect of compliant surfaces on wall turbulence. *J. of Fluid Mech.*, 768:415–441, 2015.

[41] M MacDonald, D Chung, N Hutchins, L Chan, A Ooi, and R García-Mayoral. The minimal channel: a fast and direct method for characterising roughness. In *J. of Phys.: Conf. Series*, volume 708, page 012010. IOP Publishing, 2016.

[42] R Mathis, N Hutchins, and I Marusic. Large-scale amplitude modulation of the small-scale structures in turbulent boundary layers. *J. Fluid Mech.*, 628: 311–337, 2009.

[43] B McKeon and A Sharma. A critical-layer framework for turbulent pipe flow. *J. Fluid Mech.*, 658:336–382, 2010.

[44] R Mejia-Alvarez and K Christensen. Low-order representations of irregular surface roughness and their impact on a turbulent boundary layer. *Phys. Fluids (1994-present)*, 22(1):015106, 2010.

[45] R Mejia-Alvarez and K Christensen. Wall-parallel stereo particle-image velocimetry measurements in the roughness sublayer of turbulent flow overlying highly irregular roughness. *Phys. Fluids (1994-present)*, 25(12):115109, 2013.

[46] R Moarref, A Sharma, J Tropp, and B McKeon. Model-based scaling of the streamwise energy density in high-Reynolds-number turbulent channels. *J. Fluid Mech.*, 734:275–316, 2013.

[47] J Monty, N Hutchins, H Ng, I Marusic, and M Chong. A comparison of turbulent pipe, channel and boundary layer flows. *J. Fluid Mech.*, 632:431–442, 2009.

[48] L Moody. Friction factors for pipe flow. *Trans. ASME*, 66(8):671–684, 1944.

[49] C Morrill-Winter, DT Squire, JC Klewicki, N Hutchins, MP Schultz, and I Marusic. Reynolds number and roughness effects on turbulent stresses in sandpaper roughness boundary layers. *Phys. Rev. Fluids*, 2(5):054608, 2017.

[50] C Navier. Mémoire sur les lois du mouvement des fluides. *Mémoires de l'Académie Royale des Sciences de l'Institut de France*, 6(1823):389–440, 1823.

[51] I Newton. *Philosophiae naturalis principia mathematica*. J. Societatis Regiae ac Typis J. Streater, 1687. URL `https://books.google.com/books?id=-dVKAQAAIAAJ`.

[52] J Nikuradse. Laws of flow in rough pipes. *NACA TM 1292*, 1933.

[53] B Nugroho, N Hutchins, and J Monty. Large-scale spanwise periodicity in a turbulent boundary layer induced by highly ordered and directional surface roughness. *Int. J. Heat and Fluid Flow*, 41:90–102, 2013.

[54] G Pathikonda and K Christensen. Inner–outer interactions in a turbulent boundary layer overlying complex roughness. *Phys. Rev. Fluids*, 2(4):044603, 2017.

[55] M Pedras and M de Lemos. Macroscopic turbulence modeling for incompressible flow through undeformable porous media. *Int. J. Heat and Mass Trans.*, 44(6):1081–1093, 2001.

[56] A Perry and J Li. Experimental support for the attached-eddy hypothesis in zero-pressure-gradient turbulent boundary layers. *J. Fluid Mech.*, 218:405–438, 1990.

[57] D Pokrajac, I McEwan, and V Nikora. Spatially averaged turbulent stress and its partitioning. *Exp. Fluids*, 45(1):73–83, 2008.

[58] L Prandtl. Über flüssigkeitsbewegung bei sehr kleiner reibung, verhandlungen des iii, int. *Math. Kongr*, pages 484–491.

[59] K Rao, R Narasimha, and M Narayanan. The 'bursting' phenomenon in a turbulent boundary layer. *J. Fluid Mech.*, 48(2):339–352, 1971.

[60] M Raupach, R Antonia, and S Rajagopalan. Rough-wall turbulent boundary layers. *App. Mech. Rev.*, 44(1):1–25, 1991.

[61] K Rosenberg and B McKeon. Efficient representation of exact coherent states of the navier-stokes equations using resolvent analysis. *Fluid Dynamics Research*, 2018.

[62] P Schmid. Dynamic mode decomposition of numerical and experimental data. *J. Fluid Mech.*, 656:5–28, 2010.

[63] P Schmid and D Henningson. *Stability and transition in shear flows*, volume 142. Springer Science & Business Media, 2012.

[64] W Schoppa and F Hussain. Coherent structure generation in near-wall turbulence. *J. Fluid Mech.*, 453:57–108, 2002.

[65] M Schultz and K Flack. The rough-wall turbulent boundary layer from the hydraulically smooth to the fully rough regime. *J. Fluid Mech.*, 580:381–405, 2007.

[66] S Symon, N Dovetta, B McKeon, D Sipp, and P Schmid. Data assimilation of mean velocity from 2D PIV measurements of flow over an idealized airfoil. *Exp. Fluids*, 58(5):61, 2017.

[67] S Symon, K Rosenberg, S Dawson, and B McKeon. Non-normality and classification of amplification mechanisms in stability and resolvent analysis. *Phys. Rev. Fluids*, 3(5):053902, 2018.

[68] A Towne, O Schmidt, and T Colonius. Spectral proper orthogonal decomposition and its relationship to dynamic mode decomposition and resolvent analysis. *J. Fluid Mech.*, 847:821–867, 2018.

[69] A Townsend. *The structure of turbulent shear flow*. Cambridge University Press, 1980.

[70] L Trefethen and M Embree. *Spectra and pseudospectra: the behavior of nonnormal matrices and operators*. Princeton University Press, 2005.

[71] C Vanderwel and B Ganapathisubramani. Effects of spanwise spacing on large-scale secondary flows in rough-wall turbulent boundary layers. *J. Fluid Mech.*, 774, 2015.

[72] R Volino, M Schultz, and K Flack. Turbulence structure in boundary layers over periodic two-and three-dimensional roughness. *J. Fluid Mech.*, 676:172–190, 2011.

[73] J Weideman and S Reddy. A matlab differentiation matrix suite. *ACM Transactions on Mathematical Software (TOMS)*, 26(4):465–519, 2000.

[74] D Willingham, W Anderson, K Christensen, and J Barros. Turbulent boundary layer flow over transverse aerodynamic roughness transitions: induced mixing and flow characterization. *Phys. Fluids*, 26(2):025111, 2014.